U.S.NRC
United States Nuclear Regulatory Commission
Protecting People and the Environment

NUREG/CR-7186

Experimental Measurement of Suppression Pool Void Distribution During Blowdown in Support of Generic Issue 193

Office of Nuclear Regulatory Research

AVAILABILITY OF REFERENCE MATERIALS IN NRC PUBLICATIONS

NRC Reference Material

As of November 1999, you may electronically access NUREG-series publications and other NRC records at NRC's Public Electronic Reading Room at http://www.nrc.gov/reading-rm.html. Publicly released records include, to name a few, NUREG-series publications; *Federal Register* notices; applicant, licensee, and vendor documents and correspondence; NRC correspondence and internal memoranda; bulletins and information notices; inspection and investigative reports; licensee event reports; and Commission papers and their attachments.

NRC publications in the NUREG series, NRC regulations, and Title 10, "Energy," in the *Code of Federal Regulations* may also be purchased from one of these two sources.

1. The Superintendent of Documents
   U.S. Government Printing Office
   Mail Stop SSOP
   Washington, DC 20402–0001
   Internet: bookstore.gpo.gov
   Telephone: 202-512-1800
   Fax: 202-512-2250
2. The National Technical Information Service
   Springfield, VA 22161–0002
   www.ntis.gov
   1–800–553–6847 or, locally, 703–605–6000

A single copy of each NRC draft report for comment is available free, to the extent of supply, upon written request as follows:

Address: U.S. Nuclear Regulatory Commission
Office of Administration
Publications Branch
Washington, DC 20555-0001
E-mail: DISTRIBUTION.RESOURCE@NRC.GOV
Facsimile: 301–415–2289

Some publications in the NUREG series that are posted at NRC's Web site address http://www.nrc.gov/reading-rm/doc-collections/nuregs are updated periodically and may differ from the last printed version. Although references to material found on a Web site bear the date the material was accessed, the material available on the date cited may subsequently be removed from the site.

Non-NRC Reference Material

Documents available from public and special technical libraries include all open literature items, such as books, journal articles, transactions, *Federal Register* notices, Federal and State legislation, and congressional reports. Such documents as theses, dissertations, foreign reports and translations, and non-NRC conference proceedings may be purchased from their sponsoring organization.

Copies of industry codes and standards used in a substantive manner in the NRC regulatory process are maintained at—

The NRC Technical Library
Two White Flint North
11545 Rockville Pike
Rockville, MD 20852–2738

These standards are available in the library for reference use by the public. Codes and standards are usually copyrighted and may be purchased from the originating organization or, if they are American National Standards, from—

American National Standards Institute
11 West 42nd Street
New York, NY 10036–8002
www.ansi.org
212–642–4900

Legally binding regulatory requirements are stated only in laws; NRC regulations; licenses, including technical specifications; or orders, not in NUREG-series publications. The views expressed in contractor-prepared publications in this series are not necessarily those of the NRC.

The NUREG series comprises (1) technical and administrative reports and books prepared by the staff (NUREG–XXXX) or agency contractors (NUREG/CR–XXXX), (2) proceedings of conferences (NUREG/CP–XXXX), (3) reports resulting from international agreements (NUREG/IA–XXXX), (4) brochures (NUREG/BR–XXXX), and (5) compilations of legal decisions and orders of the Commission and Atomic and Safety Licensing Boards and of Directors' decisions under Section 2.206 of NRC's regulations (NUREG–0750).

U.S.NRC
United States Nuclear Regulatory Commission
Protecting People and the Environment

NUREG/CR-7186

Experimental Measurement of Suppression Pool Void Distribution During Blowdown in Support of Generic Issue 193

Manuscript Completed: March 2011
Date Published: September 2014

Prepared by:
M. Ishii, T. Hibiki, S. Rassame,
M. Griffiths, D. Y. Lee, P. Ju, J. Yang,
S. L. Sharma, and S. W. Choi

Purdue University
School of Nuclear Engineering
West Lafayette, IN 47907

A. Ireland, NRC Project Manager
A. Velazquez-Lozada, NRC Technical Monitor

Office of Nuclear Regulatory Research

ABSTRACT

The possible failure of an Emergency Core Cooling System (ECCS) train due to a large amount of entrained gas in the ECCS pump suction piping during a loss of coolant accident (LOCA) is one of the potential engineering problems faced in a Boiling Water Reactor (BWR) power plant. The void fraction distribution and void penetration in the Suppression Pool (SP) during blowdown from a LOCA are key parameters necessary to analyze potential gas intrusion into the ECCS pump suction piping. To study void fraction distribution and void penetration in the Suppression Pool (SP) during blowdown, two sets of experiments, namely steady state tests and transient tests, were conducted using the Purdue University Multi-Dimensional Integral Test Assembly for ESBWR applications (PUMA-E) facility. The design of the test apparatus used is based on a scaling analysis from a prototypical BWR containment (Mark I) with consideration of downcomer size, SP water level and downcomer water submergence depth. Several instruments were installed to obtain the required experimental data such as the gas volumetric flow, void fraction, pressure, and temperature.

For the steady state tests, the air was injected through a downcomer pipe in the SP. Sixteen tests with various air volumetric flow rates, downcomer void conditions, and air velocity ramp rates were performed. Two periods of the experiment, namely, the initial air injection period and the quasi-steady period are observed. The initial air injection period gives the maximum void penetration depth. The quasi-steady period provides less void penetration, but with oscillation in the void penetration. It was found that the air volumetric flow rate has a minor effect on the void fraction distribution and void penetration during the initial air injection period in the range of high air volumetric flow rate conditions while it strongly impacts the void fraction distribution and void penetration during the quasi-steady state for the entire range of air flow rate conditions. The initial downcomer void conditions were found to strongly affect the void fraction distribution and void penetration during the initial period. The air velocity ramp rates were found to have a minor impact on the void distribution and penetration in both periods.

For the transient tests, sequential flows of air, steam-air mixtures, and pure steam with the various flow rate conditions were injected from the Drywell (DW) through a downcomer pipe in the SP. Eight tests were conducted at various gas volumetric fluxes at the downcomer, two different downcomer sizes, and two different initial air concentration conditions in the DW. Three periods of the experiment, namely, initial period, quasi-steady period, and chugging period are observed. The void penetration depth was maximum in the initial period and reduced in the quasi-steady period. The penetration of noncondensable gases during the chugging period, which occurs at the end of the transient, reached depths similar to those observed during the initial period. It was determined that the void distribution and area of void penetration in the SP is governed by the gas volumetric flux at the downcomer and by air concentration in the downcomer. It is noted that the transient conditions were well scaled for the initial period but not necessarily well scaled to simulate the chugging phenomena. Chugging is a complex phenomenon that depends primarily on periodic sudden condensation of steam into colder water, but also depends on gas volumetric flux, noncondensable gas concentration, frequency of the phenomenon, heat transfer, and subcooling, as well as the downcomer and suppression pool geometry. The rudimentary scaling methods used here are not suitable for use with such complex phenomenon. Instead, more specific and advanced scaling techniques would be needed.

FOREWORD

The potential safety issue of boiling water reactors (BWR) Emergency Core Cooling System (ECCS) suction concern was originally identified by staff in Region III. This issue pertains to the possible failure of the low pressure ECCS pumps due to unanticipated large quantities of gas entering into the suction pipe. The issue was identified initially as applicable to Mark I and Mark II containments during large or medium-break loss of coolant accidents (LOCA). Gas entering into the ECCS system might impact the operation of the ECCS pumps and challenge the long term cooling capability of the ECCS, which is required by Title 10, Section 50.46(b)(5), of the Code of Federal Regulations (10 CFR 50.46).

After revising the first communication of this issue, the Office of Nuclear Regulatory Research (RES) concluded that enough information was provided to perform an initial screening and that the issue does not pose any immediate safety concern and a review was requested as the potential Generic Issue (GI) 193: “BWR ECCS suction concerns”.

On the initial screening of this issue, one of the areas identified by RES to be investigated was the gas-liquid injection into the suppression pool and how deep the jet will penetrate into the pool.

A task action plan was developed to investigate the areas identified in the initial screening and an experimental program was defined and implemented as part of the technical assessment to characterize the gas-liquid jet penetration into the suppression pool.

This experimental program was conducted at Purdue University Multi-Dimensional Integral Test Assembly facility (PUMA). The objective of the experimental program was to better understand the liquid-gas jet injected into the suppression pool through the downcomers (vents) and establish the technical basis of a potential exclusion zone in the vicinity of the downcomers. The results of the experimental program to characterize the liquid-jet are documented in this report.

The experimental program described in this report is by no means a comprehensive study of the liquid-gas jet injection phenomena, nor is it a complete investigation of the ECCS suction concern. The data obtained in this program may ultimately be useful to the resolution of the generic issue, but must be considered within the context of a larger body of research. Care should be taken when extending the experimental results contained in this report to the scale and configuration of prototypic BWR Mark I and Mark II containments. The magnitude and duration of the phenomena predicted in the experimental test facility may exhibit unintended biases that were not included in the rudimentary scaling analysis performed. Extending the result to a prototypic geometry without considering all of the significant parameters may result in unrealistic extrapolations.

TABLE OF CONTENTS

Section Page

LIST OF FIGURES

LIST OF TABLES

ABBREVIATIONS AND ACRONYMS

ADS	Automatic Depressurization System
BWR	Boiling Water Reactor
DAS	Digital Acquisition System
DBA	Design Basis Accident
DC	Downcomer
DP	Differential Pressure
DPV	Depressurization Valve
DW	Drywell
ECCS	Emergency Core Cooling System
ESBWR	Economic Simplified Boiling Water Reactor
GDCS	Gravity Driven Cooling System
GSI	Generic Safety Issue
ICS	Isolation Condenser System
LOCA	Loss of Coolant Accident
Mark I	Prototypic BWR containment type
MSL	Main Steam Line
NRC	U.S. Nuclear Regulatory Commission
PC	Personal Computer (part of the digital acquisition system)
PCCS	Passive Containment Cooling System
PUMA-E	Purdue University Multi-dimensional integral test Assembly for ESBWR applications facility
RELAP5	Reactor Excursion and Leak Analysis Program (1-D thermal-hydraulic computer code)
RHR	Residual Heat Removal system
RPV	Reactor Pressure Vessel
SBWR	Simplified Boiling Water Reactor
Sch.	Schedule. A standard designation of pipe wall thickness
SP	Suppression Pool
SRV	Safety Relief Valve
WW	Wetwell

1. INTRODUCTION

1.1. Research Background

The possible failure of the Emergency Core Cooling System (ECCS) due to a large amount of entrained gas in the ECCS suction piping of a Boiling Water Reactor (BWR) is addressed in the Generic Safety Issue (GSI) 193, BWR ECCS suction concerns. Air ingestion to the Residual Heat Removal (RHR) and core spray pumps can degrade the pump performance. Therefore, it is important to understand the dynamics of the Drywell (DW) to Suppression Pool (SP) venting phenomena during blowdown and the resulting void distribution in the SP in proximity to the ECCS pump suction strainers. The void distribution, bubble velocity and size, and rate of bubble plume spread are the key parameters in this analysis of the physical phenomena.

The void distribution in the SP during the blowdown period of a design basis accident is affected by several important local phenomena. In the initial blowdown, the steam and superheated water are released into the DW. As a result, pressure in the DW and downcomers to the SP increases rapidly. During the early period of the blowdown, mostly noncondensable gas is forced through the downcomers into the SP (Ref. 1). This is followed by the steam-air mixture injection. In the later period, the vented gas is mostly steam. In the first stage, water initially standing in the downcomers is accelerated into the SP and the downcomers become voided. A large bubble of mostly air is then formed at the exit of the downcomer. The air injection from the DW results in the expansion of this bubble at the tip of the downcomer. After that, this large bubble may deform and smaller disintegrated bubbles may spread and rise to the water surface. Figure 1-1 shows local phenomena in the SP during the blowdown period of air injection. During this initial period, some disintegrated bubbles may be entrained into the bottom of the pool due to the circulating liquid flow. When the steam-air mixtures enter the downcomers, condensation occurs at the exit of the downcomers. Rapid condensation will eventually induce condensation oscillation or chugging at the exit of the downcomers. Condensation oscillation and chugging are separate phenomena and do not occur simultaneously. Whether condensation oscillation or chugging occurs and the duration of the phenomena are dependent on a number of factors including steam mass flux and pool temperature. The conditions for these phenomena can be determined from a graph developed by Moody from GE Mark I full scale test results (Ref. 2). Figure 1-2 shows the local phenomena in the SP during the period of steam-air mixture injection.

In order to study the local phenomena in the SP, both steady state and transient tests using the PUMA-E facility were proposed. In the steady state tests, different air volumetric flow rates were injected into the downcomer installed in the PUMA-E SP. For the transient tests, the actual blowdown period in the DW and subsequent injection of sequential flows of air, steam-air mixture, and pure steam with various flow rate conditions was simulated using the Reactor Pressure Vessel (RPV), DW, and SP of the PUMA-E facility.

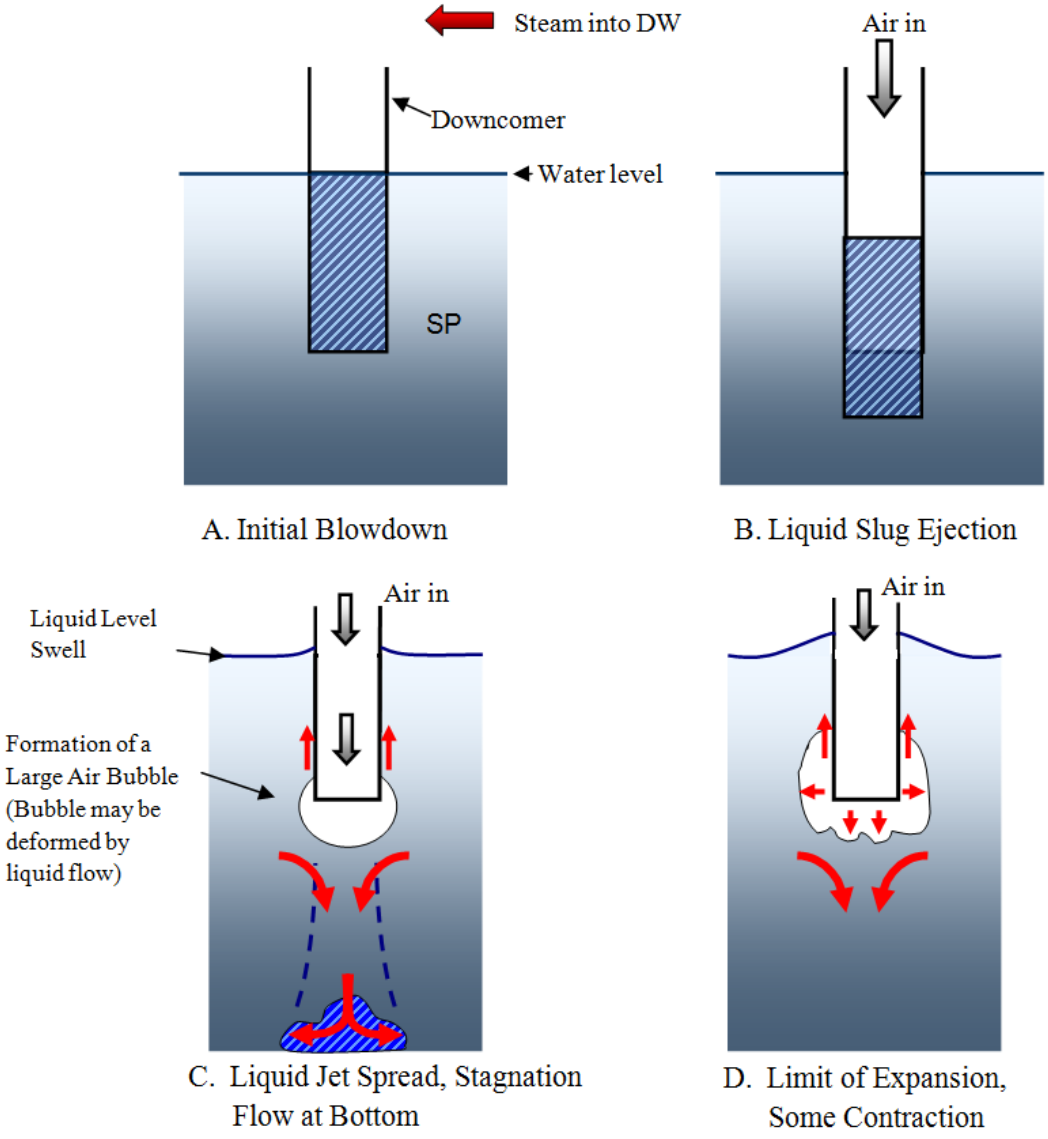

Figure 1-1 Local Phenomena in SP During Blowdown Period of Air Injection

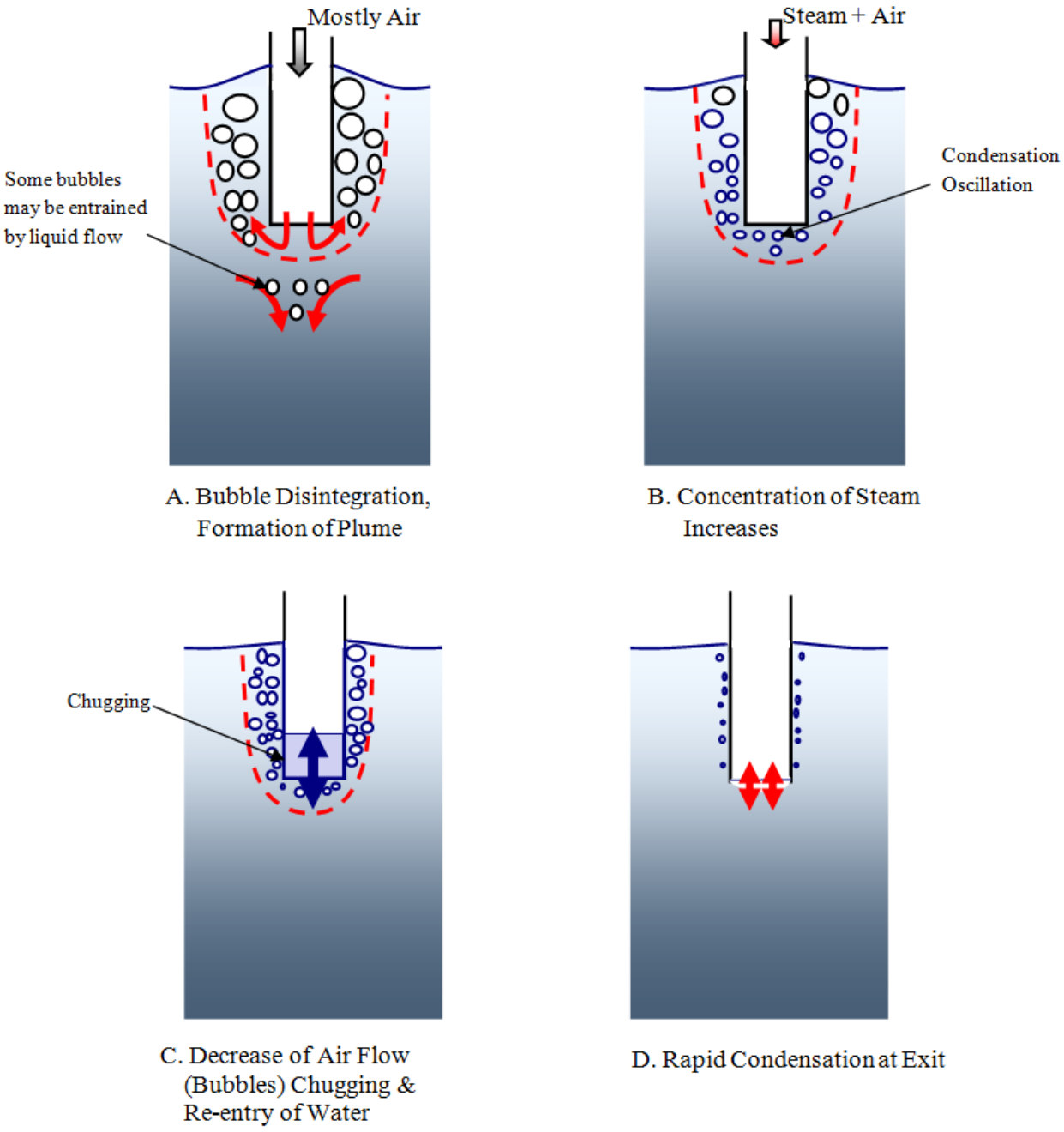

Figure 1-2 Local Phenomena in SP During Blowdown Period of Steam-air Mixtures Injection

1.2. Research Objectives

The primary objective of this study is to develop a physical understanding and to obtain experimental data for the void distribution and fluid dynamics of a BWR Mark I Type SP during the blowdown period of LOCAs. Measurements of local void fraction and high-speed movie recordings were used to determine the break-up length of a downward jet containing steam and noncondensable gas. Measurements of the local void fraction give the rate at which the bubble plume spreads, such that it is possible to estimate the void fraction and bubble velocity near the entrance of a strainer. The impact of the noncondensable gas fraction on the void distribution was also investigated.

Specific objectives are:

- To simulate the blowdown period of LOCAs using the modified PUMA-E facility so that void distribution tests in the SP can be conducted.
- To obtain a series of test data that covers a range of injection flow rates and noncondensable gas fraction for blowdown conditions to determine local void fraction, bubble size, and bubble velocity with a special focus on the locations where strainers for the ECCS pump suction are generally positioned.

2. EXPERIMENTAL FACILITY AND INSTRUMENTATION

In order to use the PUMA-E facility to investigate the void distribution and fluid dynamics of the BWR SP during blowdown, facility modifications and installation of instrumentation were necessary for both the steady state and transient tests.

2.1. PUMA-E Facility

The PUMA facility was originally built to simulate the SBWR (Simplified Boiling Water Reactor) in terms of integral test performance and control. The project was sponsored by the U.S. Nuclear Regulatory Commission (NRC). The PUMA facility is an integral test facility including major components similar to the SBWR power plant such as the Reactor Pressure Vessel (RPV), DW, Wetwell (WW), Gravity Driven Cooling System (GDCS), Passive Containment Cooling System (PCCS), Isolation Condenser System (ICS), and Automatic Depressurization System (ADS). The schematic of the PUMA facility is shown in Figure 2-1.

The PUMA-E facility was modified from the PUMA facility to adopt the design changes from the SBWR to the Economic Simplified Boiling Water Reactor (ESBWR). The heater rods, ADS, GDCS, PCCS, and ICS have been modified based on the scaling and scientific design study for the ESBWR relative to the PUMA facility (Ref. 3). The RPV, DW, and WW geometries are identical to the PUMA facility. The details of the PUMA RPV, DW, and WW can be found in the scientific design report for the PUMA facility (Ref. 3). Table 2-1 lists the important facility parameters.

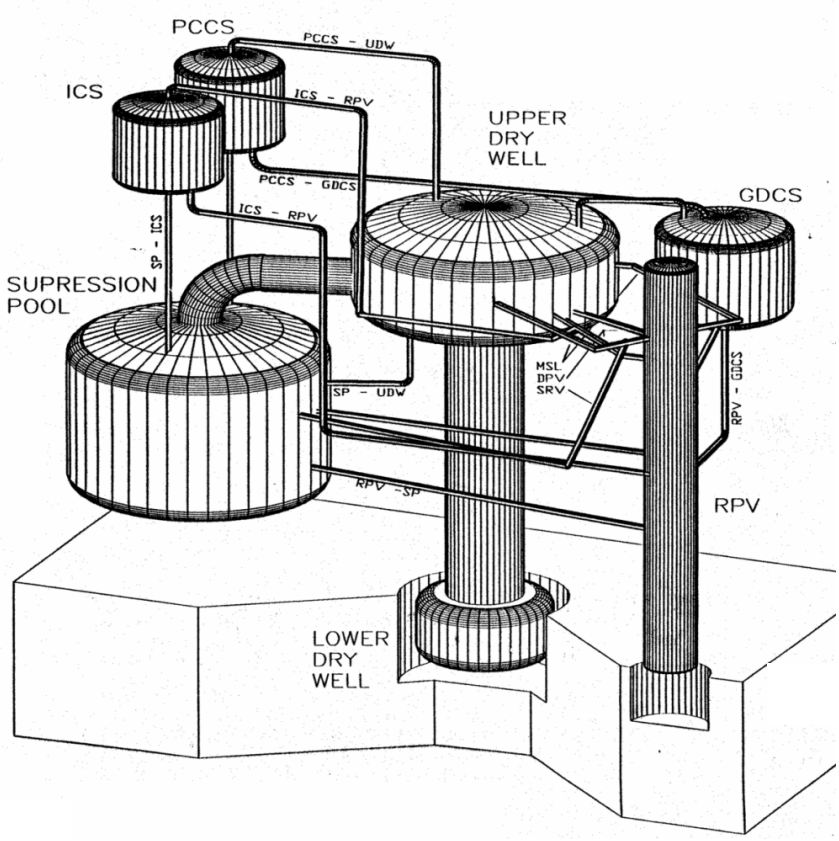

Figure 2-1 Schematic of PUMA facility

Table 2-1 PUMA-E Facility Key Parameters.

Parameters	Value
Maximum Power	630 kW (2.15×10^6 btu/h)
RPV Height / Diameter	6.13/0.600 m (20/2 ft)
RPV Free Volume	1.65 m^3 (58.3 ft^3)
DW Free Volume	12.9 m^3 (456 ft^3)
WW Water Volume	8.05 m^3 (284 ft^3)
WW Gas Volume	9.63 m^3 (340 ft^3)

2.2. Test Facility for Steady State Tests

To provide the required air flow rate for the steady state experiments, a new air supply line was connected to the 0.051 m (2 in.) existing compressed air line in the PUMA-E facility. This new compressed air line has a length of around 60 meters (197 ft) and extends to the compressed air tank, which has a volume of 14.4 m^3 (509 ft^3).

The 0.102 m (4 in.) downcomer pipe was installed in the SP of the PUMA-E facility to simulate the downcomer in the suppression chamber of the Mark I containment. The dimensions of the

downcomer pipe size and submerged depth of pipe in the SP water are determined by a scaling analysis. (The scaling analysis for these parameters is based on proprietary design information and will not be included here.)

2.2.1. Air Supply Line for Steady State Tests

Figure 2-2 shows the schematics of the test facility used for the steady state tests. In the PUMA-E facility, the Safety Relief Valve (SRV) line is branched from the Main Steam Line (MSL) and is connected the SP. To supply air flow to the downcomer pipe section in the SP, pipe lines with manual valves and pneumatic actuator valves were installed and merged into the exiting SRV line outside the SP. The valve positioned in the SRV-A line (V-AL-06) was fully closed in order to isolate the SP from the PUMA-E RPV.

The required flow rates are set by adjusting the position of valve V-AL-01, which needs to be calibrated before performing the tests.

The pneumatic actuator valves (VM-AL-01 and VM-AL-02) are used to start the experiment by sequentially opening both valves. VM-AL-02 is initially opened and closed within a short period to release air flow to the atmosphere while VM-AL-01 is opened to provide the flow to the main air supply line during the closure of VM-AL-02. Air flow can be increased smoothly without any perturbations. The ramp rate of air flow can be controlled by adjusting the opening time of VM-AL-01.

The 0.006 m (¼ in.) bypass line, including valve V-AL-02, is incorporated to adjust the initial water level in the downcomer pipe inside the SP by releasing a volumetric air flow to the air supply line.

Next to the 0.025 m (1 in.) pipeline, there are two branches of 0.051 m (2 in.) and 0.019 m (¾ in.) with manual valves. The 0.051 m (2 in.) pipeline is used for experiments with high flow rate, while the 0.019 m (¾ in.) pipeline is utilized for experiments with relatively low flow rate. This is done to ensure accurate measurements of the gas flow rate, as the larger 0.051 m (2 in.) vortex flow meter is not able to accurately measure the smaller gas flow rates present in the steady state tests.

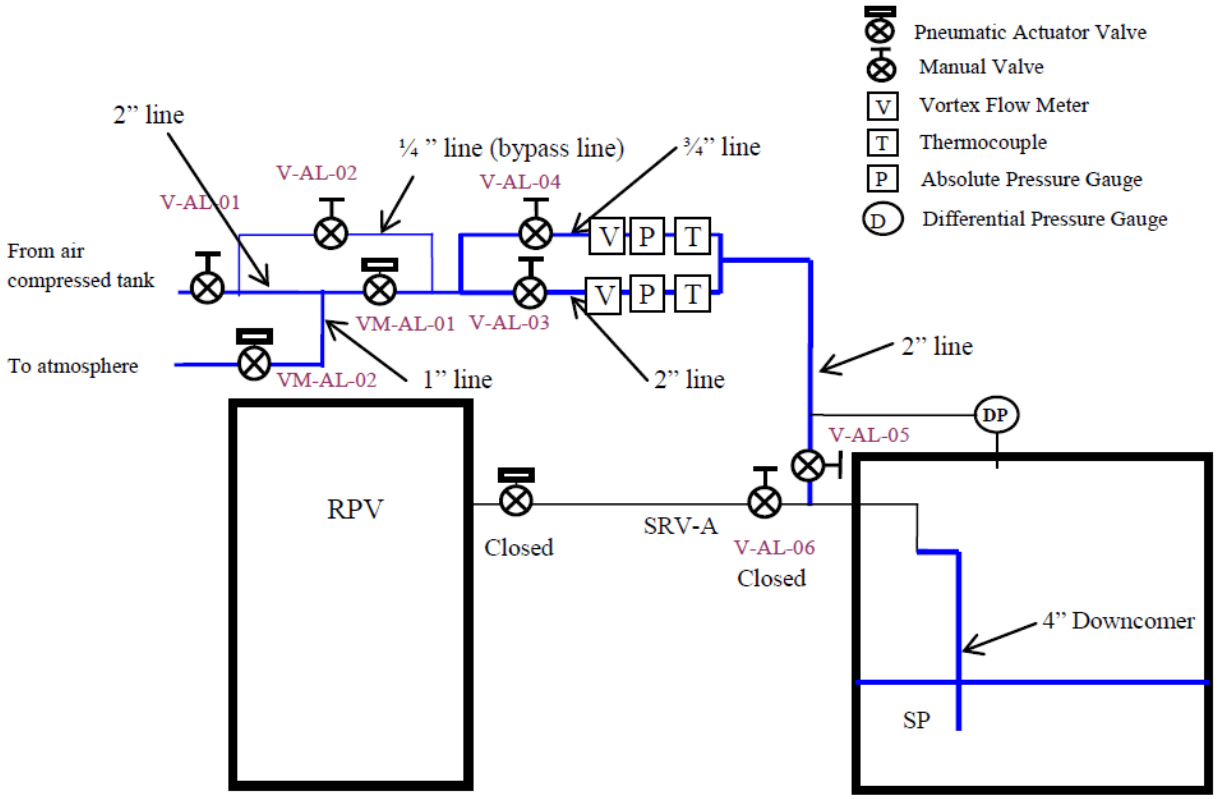

Figure 2-2 Schematics of Test Facility for Steady State Tests

2.2.2. Downcomer Section for Steady State Tests

Figures 2-3 and 2-4 show the side and top view, respectively, of the SP with the modification to the SRV line. The downcomer pipe is installed by modifying the SRV line inside the SP of PUMA-E. The existing 0.051 m (2 in.) SRV line is replaced with the 0.102 m (4 in.) pipe for the test.

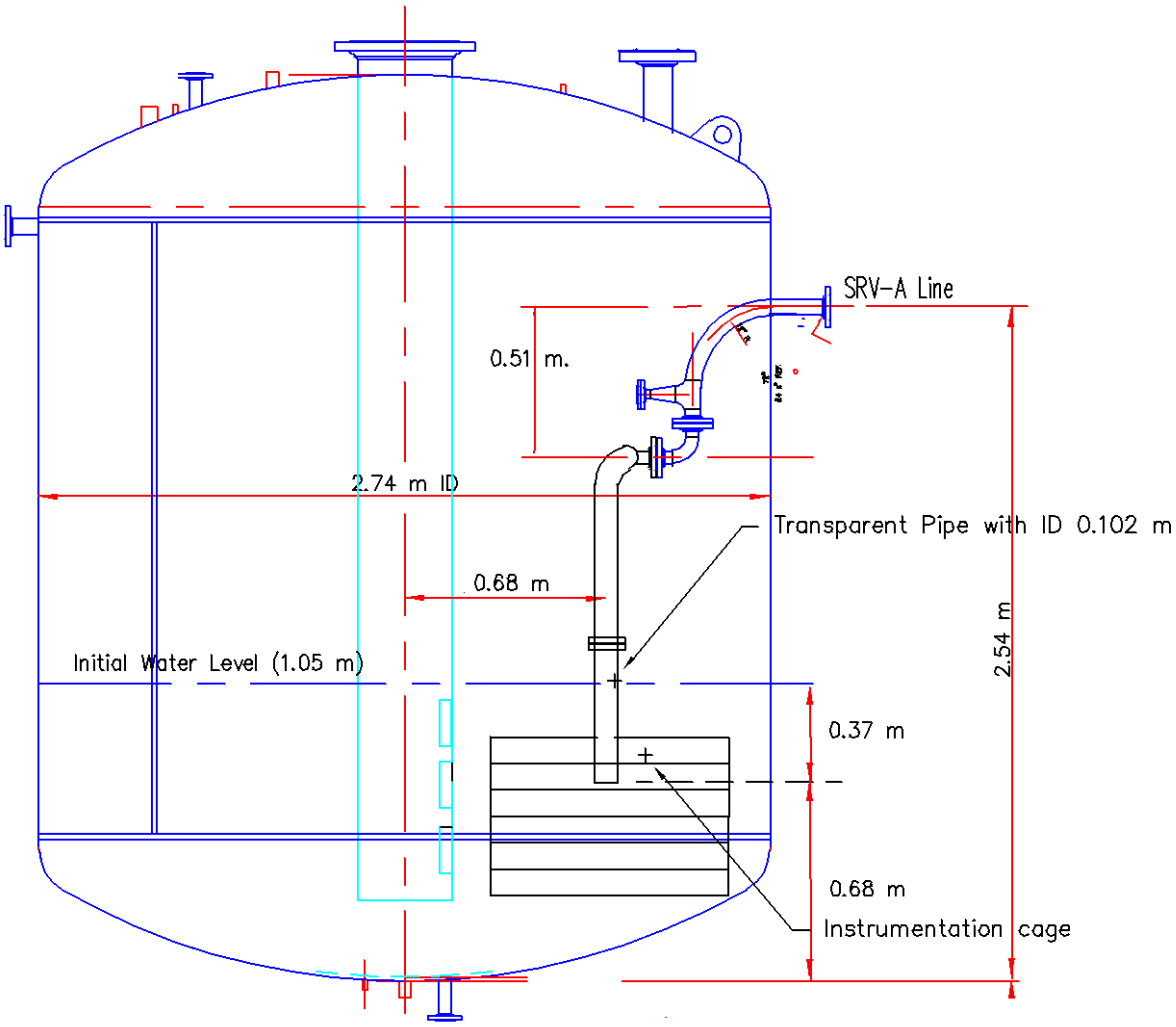

Figure 2-3 Side View of SP with Modification for Steady State Tests

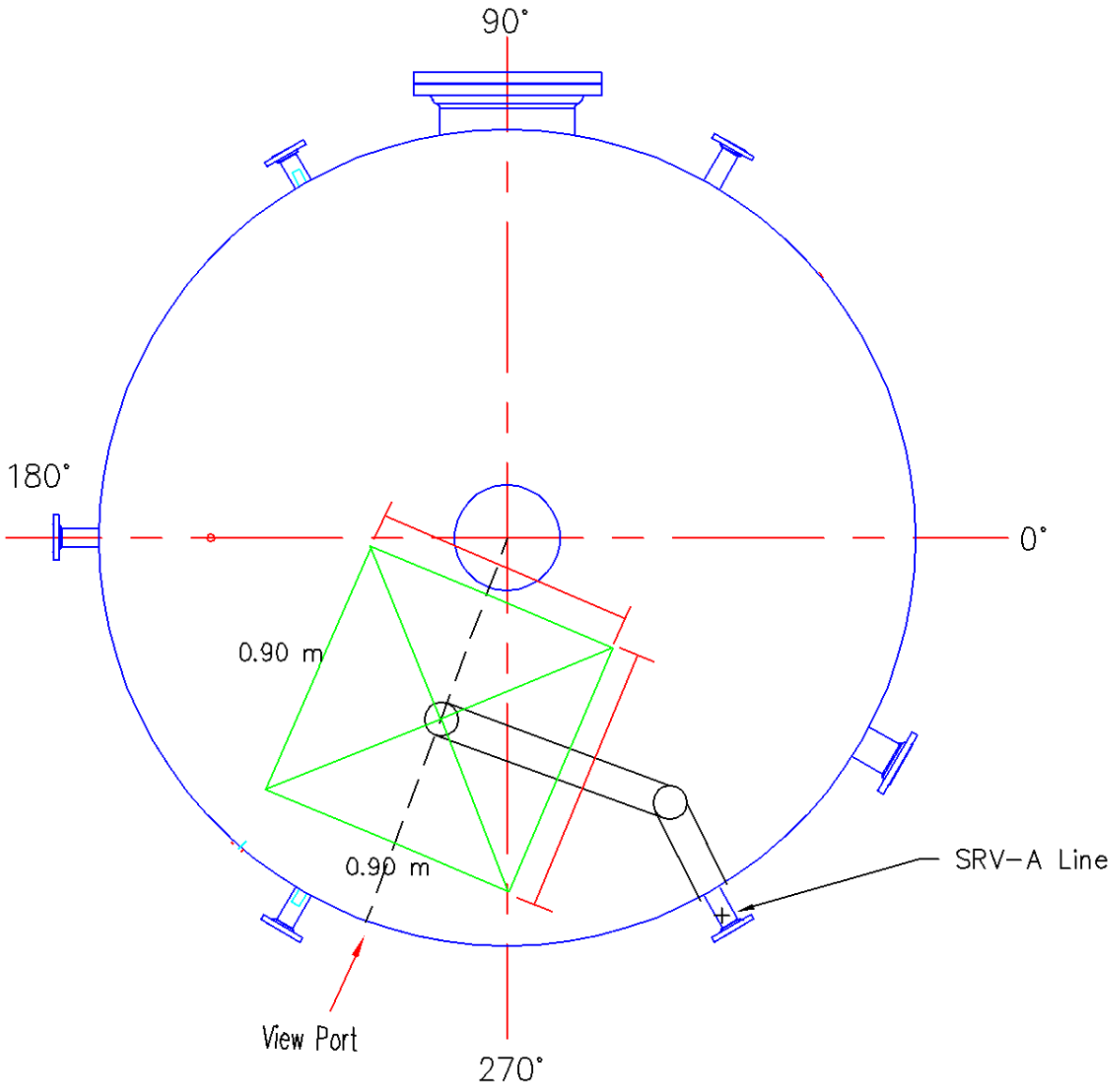

Figure 2-4 Top View of SP with Modification for Steady State Tests

The pipelines are composed of two different materials: stainless steel pipe and transparent lexan pipe. Two pipe clamps connect the vertical vent and stainless steel pipe in order to prevent shaking or vibration during the tests. The transparent lexan pipe section is extended from the stainless steel pipe at around 0.20 m (0.66 ft) above the SP water level and submerged into water with a depth of 0.37 m (1.2 ft). The transparent lexan pipe section is used to estimate the water column velocity in the downcomer by visualizing the water column-air interface using a high-speed video camera. As a second measurement for the water column level, five single-sensor conductivity probes are evenly mounted on the transparent pipe wall to measure the level of water column. To measure the void distribution near the exit of the downcomer pipe, conductivity probes are mounted on a supporting cage.

2.3. Test Facility for Transient Tests

To study the dynamics of DW to SP venting phenomena, specifically the distribution of voids in the SP during a LOCA blowdown, existing components such as the RPV, DW, Automatic Depressurization System (ADS) lines, Main Steam Lines (MSL), vertical vent, and SP in the PUMA-E facility were utilized to perform transient tests. Figure 2-5 represents the modified test facility used for the transient tests. The details of the PUMA-E RPV, DW, and SP can be found in the scientific design report for the PUMA facility (Ref. 3).

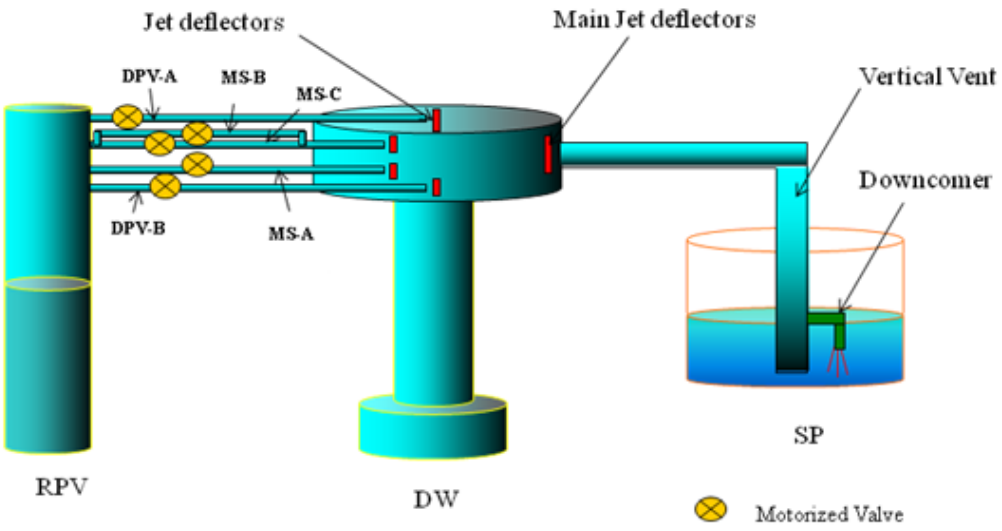

Figure 2-5 Experimental Facility for Transient Tests

2.3.1. RPV, ADS line and DW

The RPV is used to produce saturated steam that is discharged into the DW through the ADS and MSL lines. The electrical heater rods of the RPV are operated at a power of 300 kW ($1x10^6$ btu/h) during the experiment.

The PUMA-E ADS and MSL are illustrated in Figure 2-6. They were originally designed based on the scaling analysis (Ref. 3) from the ESBWR ADS system which has eight DPV lines and ten SRV lines. The PUMA DPV-A line, B line, and MS-A line each represent 2 DPV lines in the ESBWR and the PUMA MS-B and MS-C line each represent 1 DPV line in the ESBWR according to the scaling considerations. The combined set of DPV and MSL valves that are opened, namely the number of DPV lines opened, determines the steam mass flow rate discharged to the DW to achieve the scaled gas volumetric flux at the downcomer pipe.

The free volume of the DW in the PUMA-E facility is larger than the free volume that would result from scaling analyses. Modification of the DW was not considered when conducting this research, as this distortion was not expected to have an effect on the major results of the study. Jet deflectors are installed in the DW at the discharge location of each DPV line and at the

entrance of the vertical vent to prevent the discharge of steam from the RPV directly to the SP as well as to simulate the jet deflectors installed in the Mark I containment.

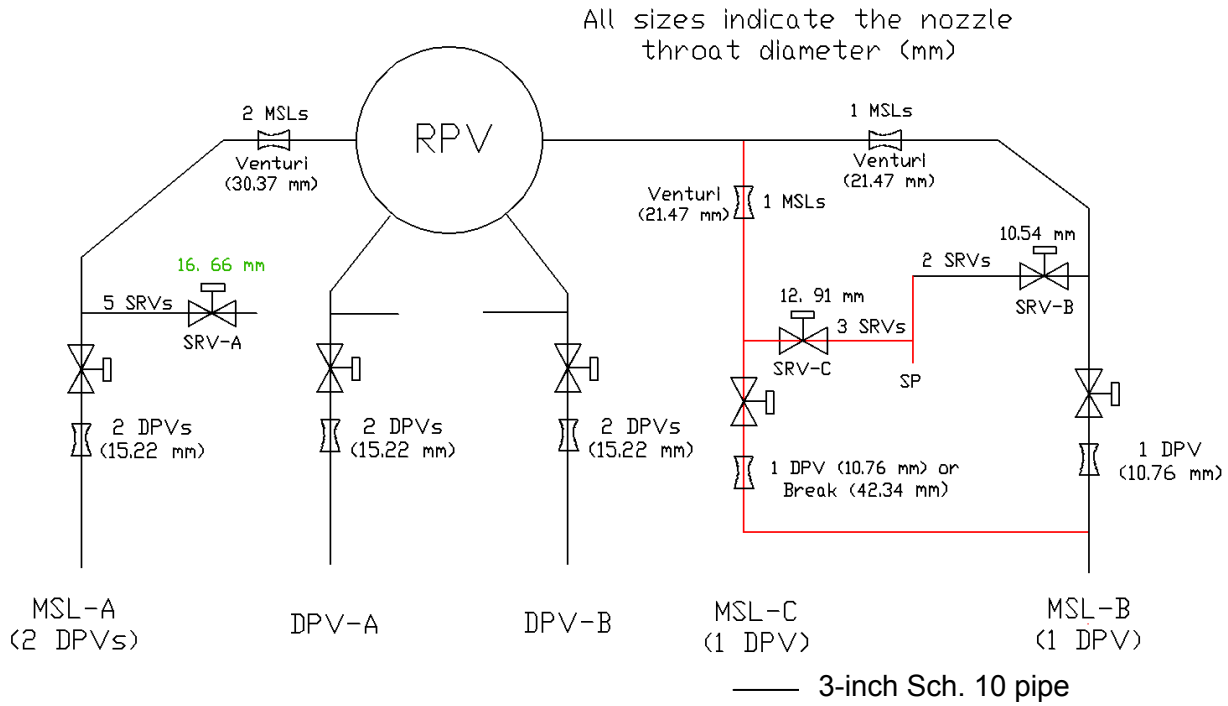

Figure 2-6 PUMA-E ADS and Main Steam Line Configuration

2.3.2. Downcomer Section for Transient Tests

A new vent line is installed on the existing vertical vent line as shown in Figure 2-7. This piping is the downcomer section for the transient tests. A Schedule 10 (Sch. 10) stainless steel pipe with 0.102 m or 0.076 m (4 in. or 3 in.) diameter is mounted on a window in the vertical vent. The other seven windows are completely closed except for a 0.025 m (1 in.) pipe installed in one window connecting the vertical vent to the SP for water level equalization. The bottom of the vertical vent is closed. To measure the water column level in the downcomer, five single-sensor conductivity probes are mounted on the pipe wall at evenly spaced intervals. A supporting cage for conductivity probes is installed near the exit of the downcomer.

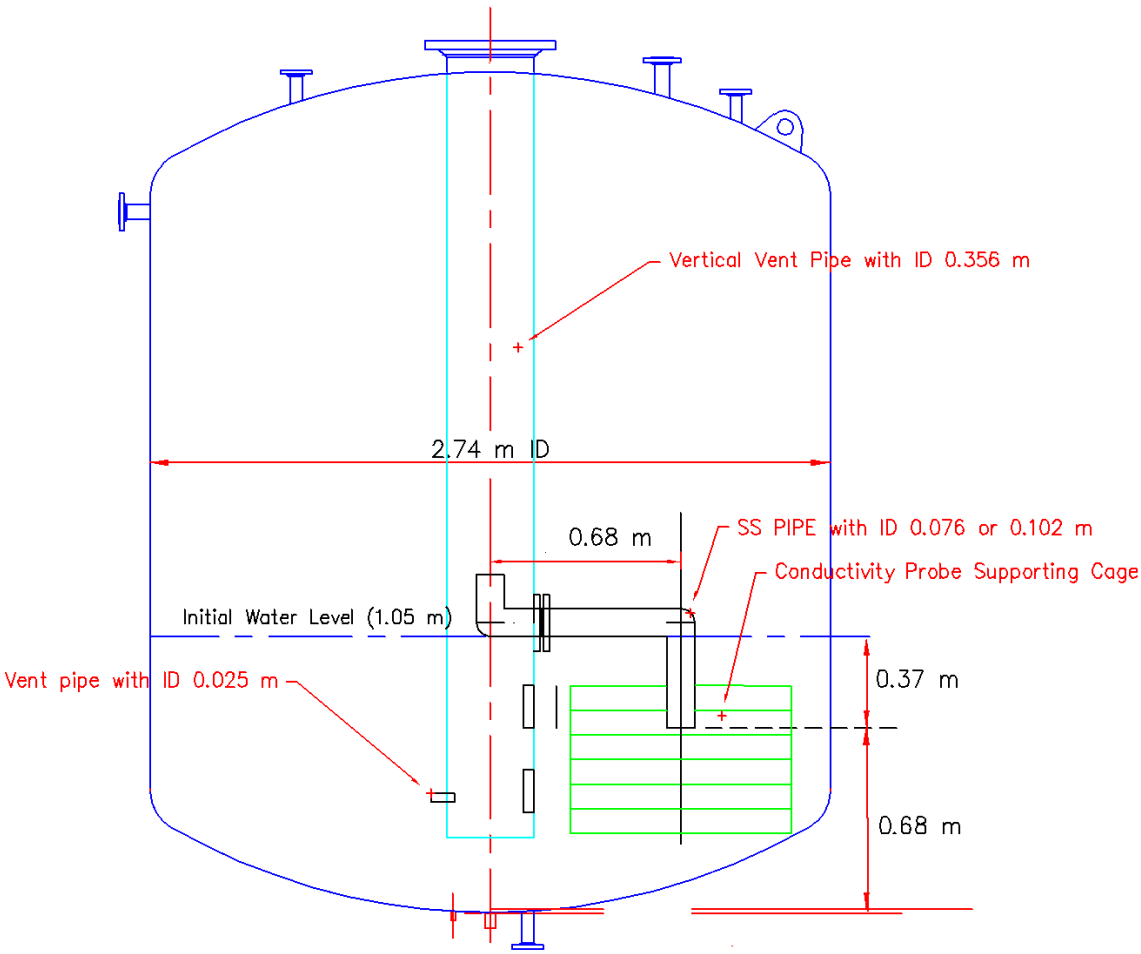

Figure 2-7 SP with Modification for Transient Tests

3. TEST DESCRIPTION

This chapter explains details of the tests performed including the test matrix, test initial conditions, test procedures, and test initial time for both the steady state tests and transient tests. Additionally, the estimation of the gas volumetric flux at the downcomer in the transient tests using RELAP5 is described.

3.1. Test Description for the Steady State Tests

The basic scaling analysis and the technical information for the prototypic plant provided by the NRC (Ref. 4) were used to develop the test matrix. The final sixteen steady state test conditions were determined by the NRC based on discussion with Purdue as shown in Table 3-1.

Table 3-1 Test Matrix for Steady State Tests.

Test No.	DC Diameter	Velocity Ramp Rate (s)	DC Condition	Flow Type	Air Mass Flow Rate (kg/s [ft/s])	Air Volumetric Flow Rate (m^3/s [ft^3/s])	Air Volumetric Flux (m/s [ft/s])
A1	0.102 m (4 in.)	1.0	Completely Filled with Water	Category 4b	0.184 [0.406]	0.153 [5.403]	18.9 [62.0]
A2				DBA	0.138 [0.304]	0.115 [4.061]	14.2 [46.6]
A3				Category 4a	0.077 [0.170]	0.064 [2.260]	7.9 [25.9]
A4				Category 2	0.005 [0.011]	0.004 [0.141]	0.5 [1.6]
A5			Partially Voided	Category 4b	0.184 [0.406]	0.153 [5.403]	18.9 [62.0]
A6				DBA	0.138 [0.304]	0.115 [4.061]	14.2 [46.6]
A7				Category 4a	0.077 [0.170]	0.064 [2.260]	7.9 [25.9]
A8				Category 2	0.005 [0.011]	0.004 [0.141]	0.5 [1.6]
A9		2.0	Completely Filled with Water	Category 4b	0.184 [0.406]	0.153 [5.403]	18.9 [62.0]
A10				DBA	0.138 [0.304]	0.115 [4.061]	14.2 [46.6]
A11				Category 4a	0.077 [0.170]	0.064 [2.260]	7.9 [25.9]
A12				Category 2	0.005 [0.011]	0.004 [0.141]	0.5 [1.6]
A13			Partially Voided	Category 4b	0.184 [0.406]	0.153 [5.403]	18.9 [62.0]
A14				DBA	0.138 [0.304]	0.115 [4.061]	14.2 [46.6]
A15				Category 4a	0.077 [0.170]	0.064 [2.260]	7.9 [25.9]
A16				Category 2	0.005 [0.011]	0.004 [0.141]	0.5 [1.6]

The downcomer condition is determined based on the voided level in the downcomer section. For partially voided conditions, the downcomer water level is reduced to 39% of the submergence depth of the downcomer. This voided condition represents the DW to SP differential pressure of 7.584 kPa (1.1 psi) in some BWR power plants.

The definition of flow types in category 4a, DBA, and category 2 are classified by the NRC based on various volumetric flow rates for different pipe break sizes in LOCAs (Ref. 4).

Category 4b is based on the maximum capability of the air supply flow in the PUMA-E test facility. The velocity ramp rate is the required time to reach the steady state air flow rate.

For the case of the 0.102 m (4 in.) downcomer size, the volumetric flow rates and fluxes are computed from the air mass flow rates when the air density is about 1.2 kg/m^3 (0.075 lbm/ft^3). In the steady state tests, the air (15 °C to 20 °C [59 °F to 68 °F]) is injected into the SP (25 °C [77 °F]), while for the prototypic plant case, the DW air (52°C to 65°C [126 °F to 149 °F]) would be injected into the SP (27°C to 37°C [80.6 °F to 98.6 °F]). Due to these temperature differences, there may be as much as an 11.8% change in PUMA gas volumetric flow rate in the upper section of the pool relative to the prototype if we translate the conditions using a scaling method. However, these steady state tests are also separate effect tests with the air flow rate treated as a parameter. Therefore the whole set of data can be used to understand the effect of air volumetric flow rate on important parameters such as void fraction distribution, bubble velocity, and bubble chord length.

3.2. Test Description for Transient Tests

3.2.1. Test Matrix

Table 3-2 shows the test matrix for the transient tests. There are two series of tests. Each series is performed with a different downcomer pipe size. Each test, regardless of series, is performed with different initial air concentrations in the DW and mixed steam and air volumetric flux at the downcomer. Performing tests for 0.076 m and 0.102 m (3 in. and 4 in.) downcomer pipes aims to confirm the scaling from the prototypic plant to the scaled down test facility. Furthermore, the 0.076 m (3 in.) downcomer can provide a higher mixture volumetric flux than the 0.102 m (4 in.) downcomer pipe at the same break flow rate. The mixture volumetric flux at the downcomer pipe in the initial blowdown period covers the possible range of volumetric flux at the downcomer in the prototypic plant, scaled down to test facility conditions.

Table 3-2 Test Matrix for Transient Test.

Test No.	Downcomer size	Initial air concentration in DW (%)	No. of DPVs opening	Steam Mass flow Rate Blowdown* from RPV to DW (kg/s [lbm/s])	Mixture Volumetric Flux at Downcomer** (m/s [ft/s])
T1	0.076 m (3 in.)	100	5 DPVs	0.65 [1.43]	75 [246]
T2	0.076 m (3 in.)	100	3 DPVs	0.31 [0.68]	41 [135]
T3	0.076 m (3 in.)	100	2 DPVs	0.21 [0.46]	28 [92]
T4	0.076 m (3 in.)	80	5 DPVs	0.65 [1.43]	84 [276]
T5	0.102 m (4 in.)	100	5 DPVs	0.65 [1.43]	45 [148]
T6	0.102 m (4 in.)	100	3 DPVs	0.31 [0.68]	27 [89]
T7	0.102 m (4 in.)	100	2 DPVs	0.21 [0.46]	17 [56]
T8	0.102 m (4 in.)	80	5 DPVs	0.65 [1.43]	50 [164]

* Steam mass flow rate from RPV during the initial blowdown measured by nozzle.

** Estimated values based on the RELAP5 calculation during the initial blowdown.

3.2.2. Test Initial Condition

The initial conditions in the RPV, DW, and SP are shown in the Table 3-3. The pressure and temperature in the SP and DW of the PUMA facility are identical to the Mark I containment operational conditions (Ref. 4). The water level in the SP is set at 1.05 m (3.44 ft). The submergence length for the downcomer in the SP is 0.37 m (1.2 ft), filling the downcomer with water to the base of the elbow joining the vertical outlet and the horizontal inlet.

Table 3-3 Initial Conditions for Transient Test.

Component	Parameter	PUMA-E
RPV	RPV power	300 kW (1.02×10^6 btu/h)
	Steam Dome Pressure	1034 kPa (135.3 psig)
	Steam Dome Temperature	197.6 °C (387.7 °F)
	Collapsed Water Level	2.81 m (9.22 ft)
DW	Pressure	113.4 kPa (1.747 psig)
	Water Level	0 m (0 ft)
	Steam/NC Temperature at Upper DW	65.5 °C (149.9 °F)
SP	Pressure	113.4 kPa (1.747 psig)
	Water Temperature (bulk)	37 °C (98.6 °F)
	Water Level	1.05 m (3.44 ft)

3.2.3. Estimation of Gas Volumetric Flux at Downcomer of PUMA-E Facility Using RELAP5 for Transient Tests

To estimate gas volumetric flux at the downcomer of the PUMA-E facility, the transient tests were simulated using the RELAP5/mod 3.3 code. The DW, SP, Vertical Vent, valves, and downcomer section of the PUMA-E facility were modeled using several components of RELAP5 such as the PIPE, BRANCH, TMDPJUN, SINGJUN, VALVE, etc. The time-dependent inlet flow condition was input as TMDPJUN using the experimental data from the steam mass flow rate measured by nozzle measurements. Figures 3-1 and 3-2 show the RELAP5 nodalization for the DW, and vertical vent, and downcomer section, respectively. The simulation was performed for 600 seconds to align with the actual transient test time. The calculated results of the gas volumetric flux at the downcomer were obtained.

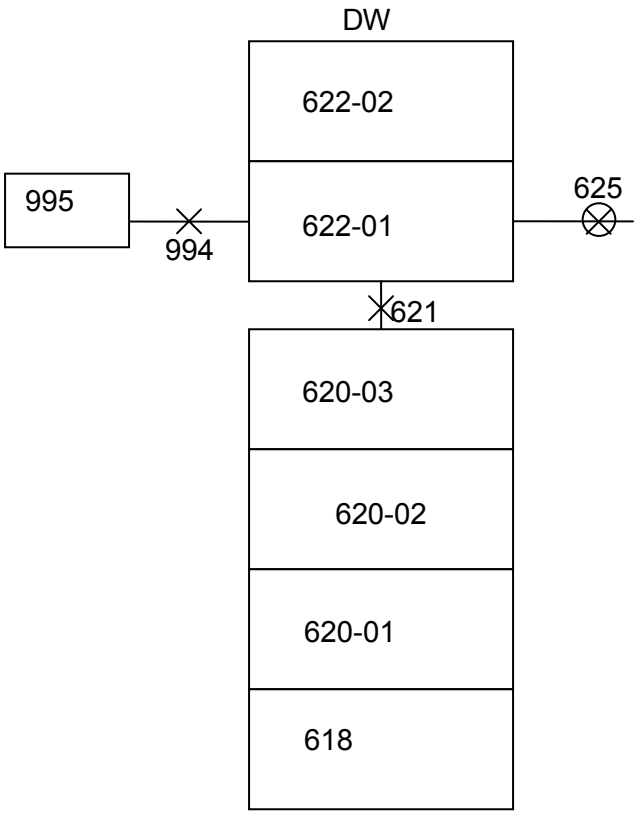

Figure 3-1 RELAP5 Nodalization for the DW Section

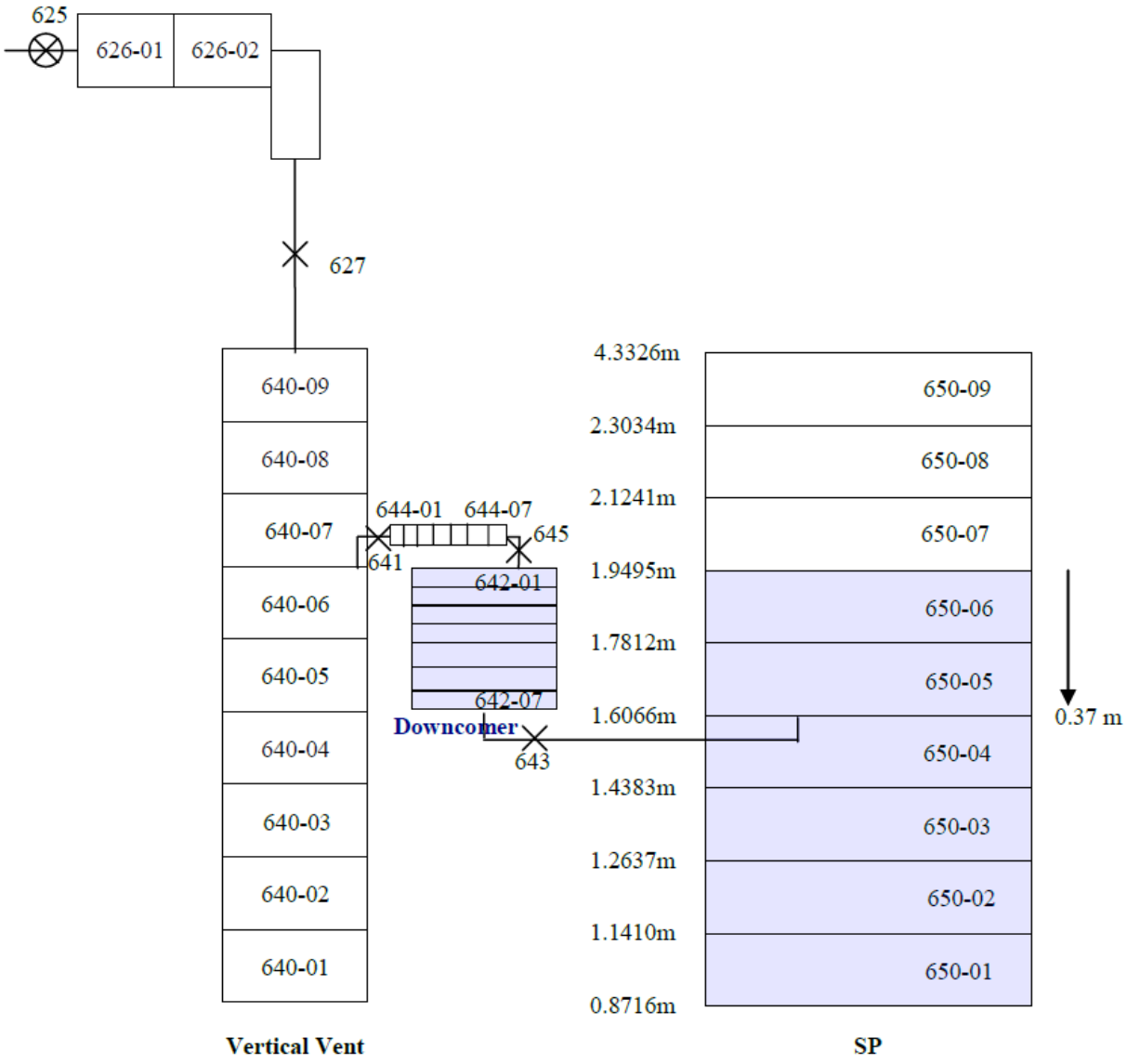

Figure 3-2 RELAP5 Nodalization for the Vertical Vent, Downcomer, and SP

4. TEST RESULTS AND DISCUSSION

Sixteen conditions for the steady state tests and eight conditions for the transient tests were performed using the PUMA-E facility. Information about void fraction distribution, axial and radial void penetration, bubble velocity, and bubble chord length for each test condition were obtained for both type of tests. To better understand the local physical phenomena in the SP during blowdown, this chapter discusses, in detail, the experimental results for both the steady state and transient tests. For both test types, the test conditions were varied by adjusting several parameters. Table 4-1 lists the varied test conditions for the steady state and transients tests.

Table 4-1 List of Varied Test Conditions for the Steady State and Transient Tests.

Type of Test	Varied Test Conditions
Steady State Tests	- Air volumetric flow rate/flux - Initial downcomer void condition - Air velocity ramp rate
Transient Tests	- Downcomer diameter size - Gas (steam/air) volumetric flux - Initial air concentration in the DW

For the steady state tests, the air volumetric flow rate/flux, initial downcomer void condition, and the air velocity ramp rate were varied for the performance of each test. The impact of these parameters on the void fraction and penetration depth were studied and the results are provided and discussed in Section 4.1.

For the transient tests, the downcomer diameter, gas (steam/air) volumetric flux, and the initial air concentration in the DW were varied for the performance of each test. The impact of these parameters on the void fraction and penetration depth were studied and the results are provided and discussed in Section 4.2.

4.1. Steady State Tests

During the initial blowdown period of a LOCA in a prototypic Mark I type containment, the noncondensable gas in the DW is forced through the downcomers into the SP. To simulate the initial blowdown of noncondensable gas, the steady state tests were performed using air injection through a downcomer with different air volumetric flow rates, initial downcomer void conditions, and air velocity ramp rates. The experimental results from different test conditions were used to understand the local phenomena in the SP during the blowdown phase of a LOCA. Investigation of the impact of the air volumetric flow rates, initial downcomer void condition, and the air velocity ramp rate on the void fraction distribution and void penetration depth were performed for the steady state tests using a parametric study. The results of selected test conditions are compared in the following sections to illustrate the impact of each parameter on the void fraction distribution and void penetration depth in the SP.

4.1.1. Flow Visualization for Steady State Tests.

In order to understand the global phenomena in the SP during the steady state tests, the bubble behavior at the downcomer exit was recorded by a high-speed camera. Figures 4-1 and 4-2 highlight the development of the bubble plume around the downcomer exit in the SP for test No. A1. This test condition was chosen as an example because the results are typical in terms of bubble plume formation. Figure 4-1 shows the development of the bubble plume during the initial period. The air was injected downward through the downcomer pipe and a spherical bubble plume was formed at the exit of the downcomer. The initial injection resulted in the maximum void penetration depth since the bubble was entrained into the bottom of the pool due to the circulating liquid flow induced by the liquid slug injection into the SP. The plume then rose to the water surface due to the buoyancy force. Some remnants of the broken-up plume were present as bubbles at the bottom of the SP during this process.

During the quasi-steady period, the bubble plume oscillated. A small plume would form at the exit of the downcomer (Figure 4-2) and rise, followed a short time later by the formation of another plume, resulting in the oscillation of the axial and radial void penetration. However, the axial penetration depth of the oscillating bubble plume was less than half that of the initial bubble plume. This is because the oscillating bubble plume does not include the liquid slug, and the liquid circulation effects are greatly reduced. This quasi-steady process continued cyclically during the remainder of the experiment.

These are the only two periods, namely, initial air injection and quasi-steady, observed during the steady state tests.

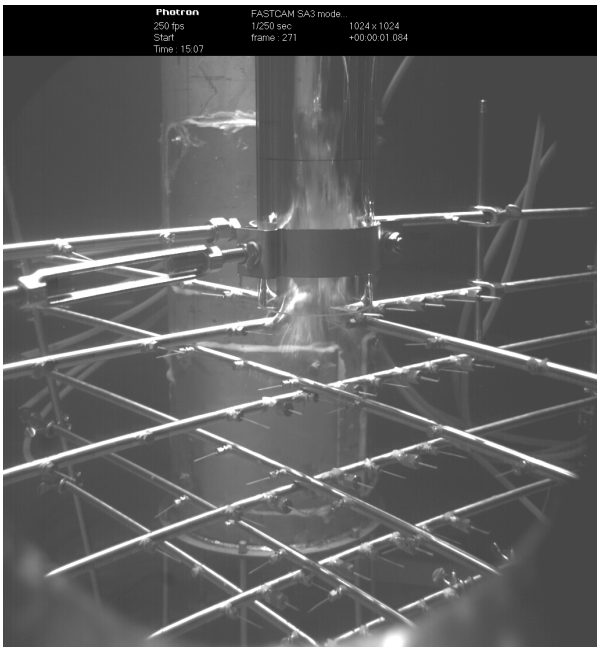

Time = 1.084 seconds

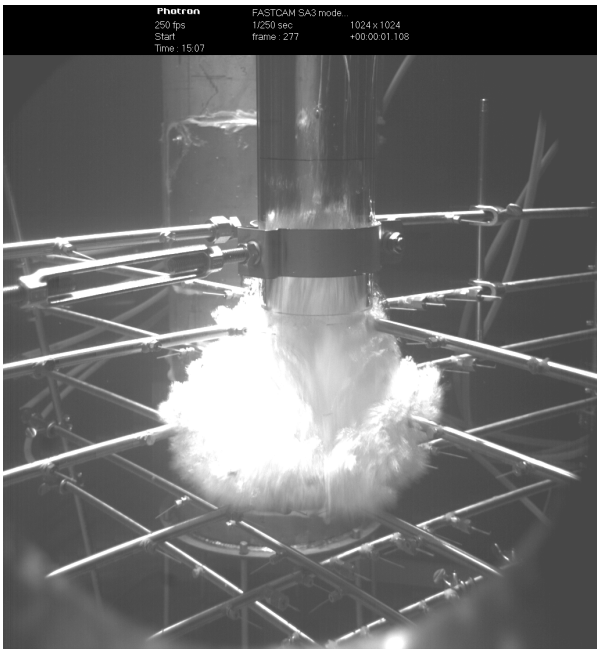

Time = 1.108 seconds

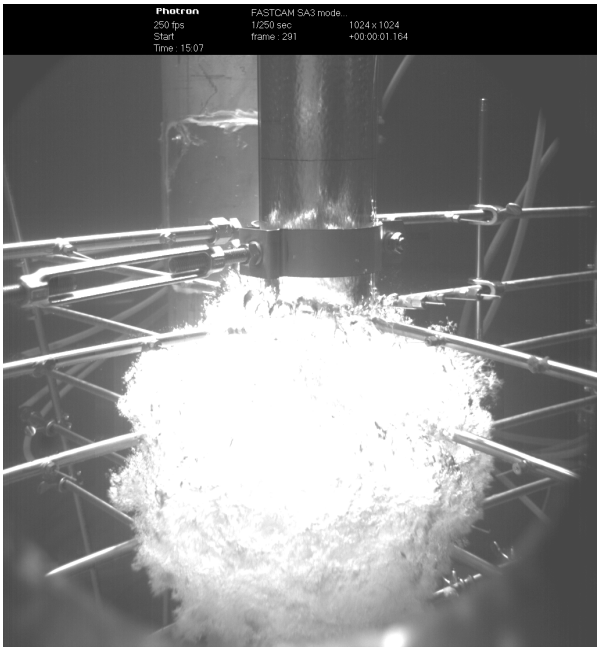

Time = 1.164 seconds

Time = 1.420 seconds

Figure 4-1 Bubble Plume Around the Downcomer Exit During t=1.084-1.420 Seconds (the Initial Period) for Test No. A1

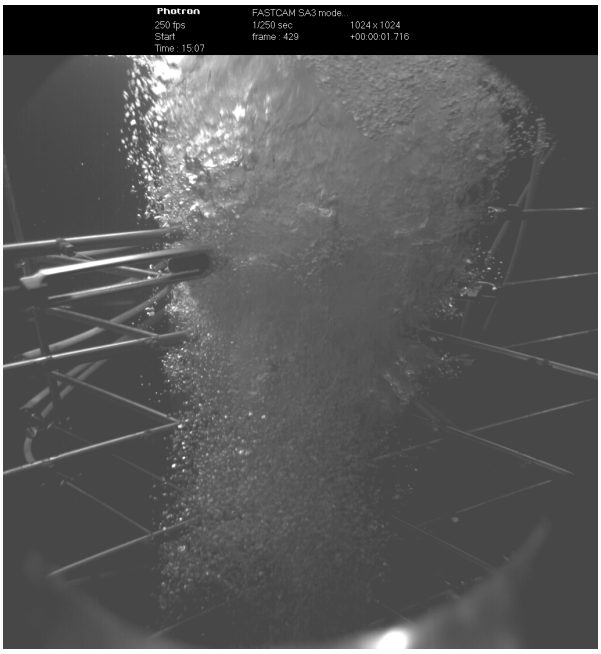

Time = 1.716 second

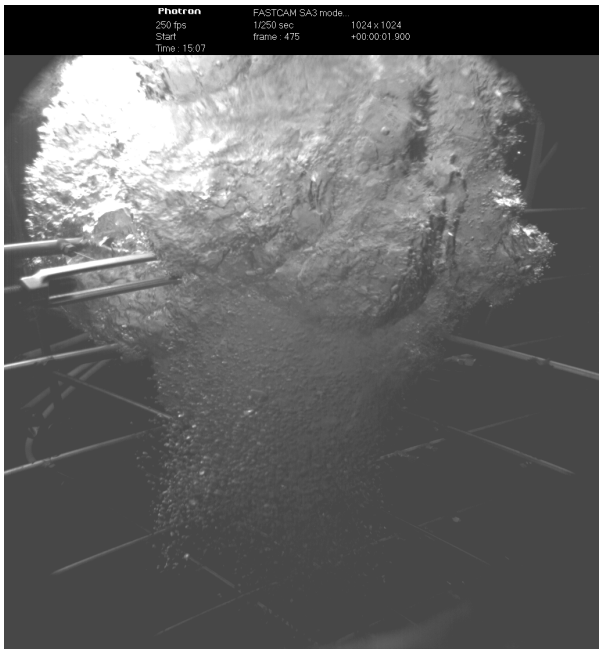

Time = 1.900 second

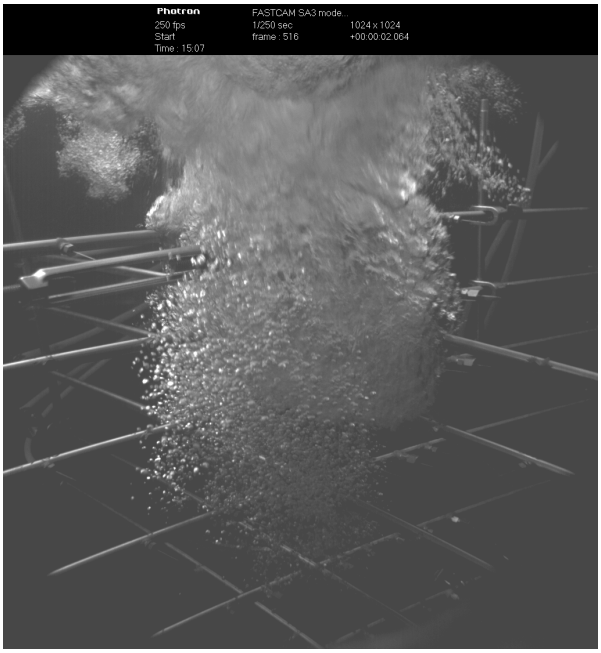

Time = 2.064 second

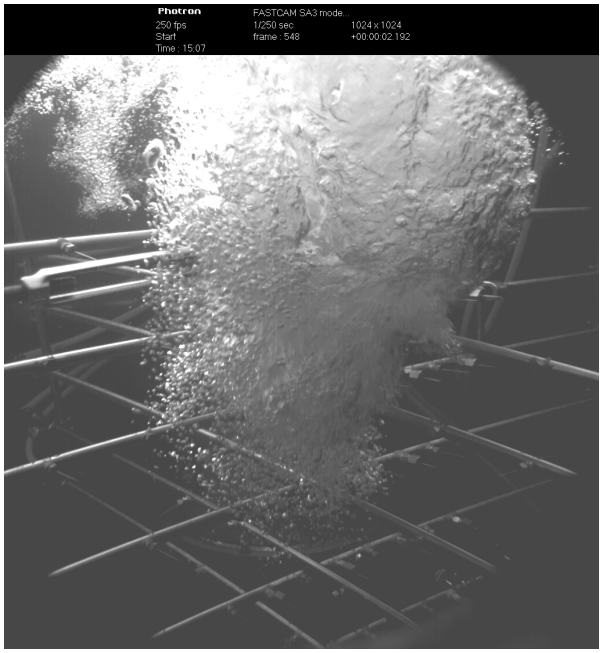

Time = 2.192 second

Figure 4-2 Bubble Plume Around the Downcomer Exit During t=1.716-2.192 Seconds (the Quasi-steady Period) for Test No. A1

4.1.2. Air Volumetric Flow Rate

The results of test Nos. A1, A2, A3, and A4 (test conditions shown in Table 4-2) are compared in this section to illustrate the impact of the air volumetric flow rate on the void fraction distribution and void penetration. Table 4-3 provides a description of each figure used to determine the effect of the air volumetric flow rate on SP void penetration and distribution.

Table 4-2 Test Conditions for Comparison of the Air Volumetric Flow Rate Effect on Void Distribution and Void Penetration in the SP.

Test No.	DC Diameter	Air Velocity Ramp Rate (s)	DC Condition	Prototypic Plant Flow Type	Air Mass Flow Rate (kg/s [lbm/s])	Air Volumetric Flow Rate (m^3/s [ft^3/s])	Air Volumetric Flux (m/s [ft/s])
A1	0.102 m (4 in.)	1.0	Completely Filled with Water	Category 4b	0.184 [0.406]	0.153 [5.403]	18.9 [62.0]
A2				DBA	0.138 [0.304]	0.115 [4.061]	14.2 [46.6]
A3				Category 4a	0.077 [0.170]	0.064 [2.260]	7.9 [25.9]
A4				Category 2	0.005 [0.011]	0.004 [0.141]	0.5 [1.6]

Table 4-3 Description of Figures for Determining the Effect of Air Volumetric Flow Rate on Void Penetration and Distribution in the SP.

Figure No.	Figure Descriptions	Experimental Period	Measurement Device
4-3	Measured Air Volumetric Flow Rate	Initial and Quasi-steady	Vortex Flow Meter
4-4	Void Fraction Distribution	Initial Period	Conductivity Probes
4-5	Void Fraction Distribution	Quasi-steady	Conductivity Probes
4-6	Axial Void Penetration	Initial and Quasi-steady	Conductivity Probes
4-7	Radial Void Penetration	Initial and Quasi-steady	Conductivity Probes
4-8	Axial Void Penetration	Initial and Quasi-steady	High-speed Camera
4-9	Radial Void Penetration	Initial and Quasi-steady	High-speed Camera

The void fractions, as shown in Figures 4-4 and 4-5, were averaged over a time period of 1 second. For instance, the void fraction at 2 seconds in Figure 4-4 was obtained by averaging the experimentally measured void fraction during the 1.5 to 2.5 second time frame. The void fraction at a given location at a given time is represented in the figures by a highlighted red or blue circle. The shade of the red circles represents low void fractions ranging from 0.025% to 2% and the shade of the blue circles represents high void fractions ranging from 2% to 100%. Two percent void fraction is the current acceptance criteria for BWR ECCS pump void fraction disposure (Ref. 5). These figures can provide beneficial information in terms of the void fraction distribution and void penetration at a given time.

Figure 4-6 shows the axial void penetration measured from the center of the downcomer exit using the conductivity probes. Figure 4-7 shows the radial void penetration measured at the conductivity probe level immediately below the downcomer exit (level 0.02 m [0.79 in.]). The figures are estimated based on the information from the raw data signals obtained from the conductivity probes. The data is discrete since the conductivity probes are located at fixed points in the SP. The smooth curves are plotted to present the void penetration trends. Figure 4-8 shows the axial void penetration estimated from the high-speed camera images measured from the center of the downcomer. Figure 4-9 shows the radial void penetration estimated from the high-speed camera images at level 0.02 m (0.79 in.) below the downcomer. Data points in Figures 4-8 and 4-9 are roughly estimated using information from images recorded by the high-speed camera. Each void penetration data point was obtained by measuring the bubble plume penetration from the images recorded by the high-speed camera. Hence, each data point represents the boundary of the bubble plume at a certain time. The smooth curves are plotted to present the void penetration trends. It is noted that the time scales for each test in Figures 4-6, 4-7, 4-8, and 4-9 are synchronized in order to be able to make a good comparison between each test.

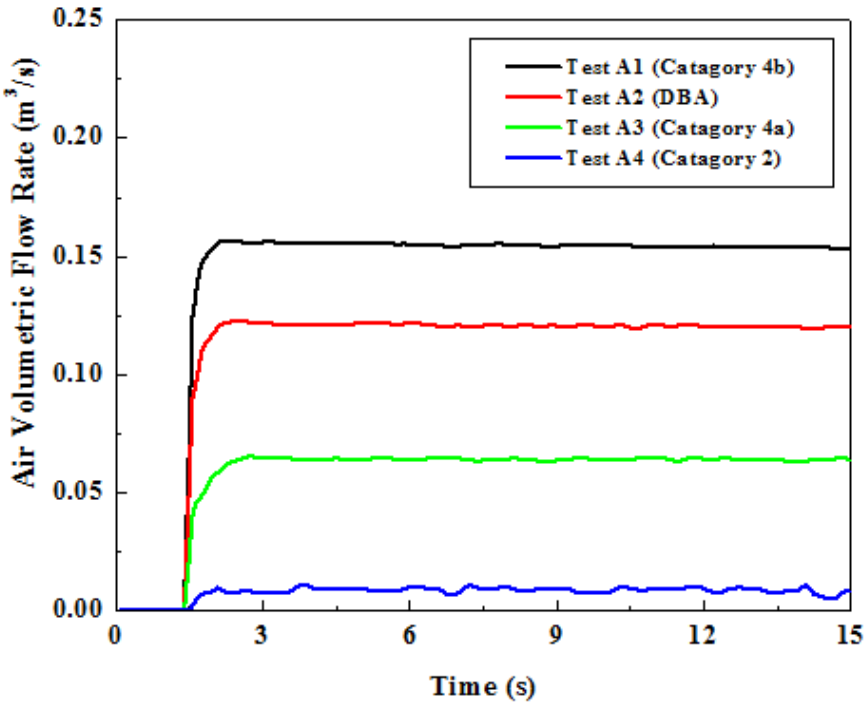

Figure 4-3 Measured Air Volumetric Flow Rate for Test Nos. A1, A2, A3, and A4

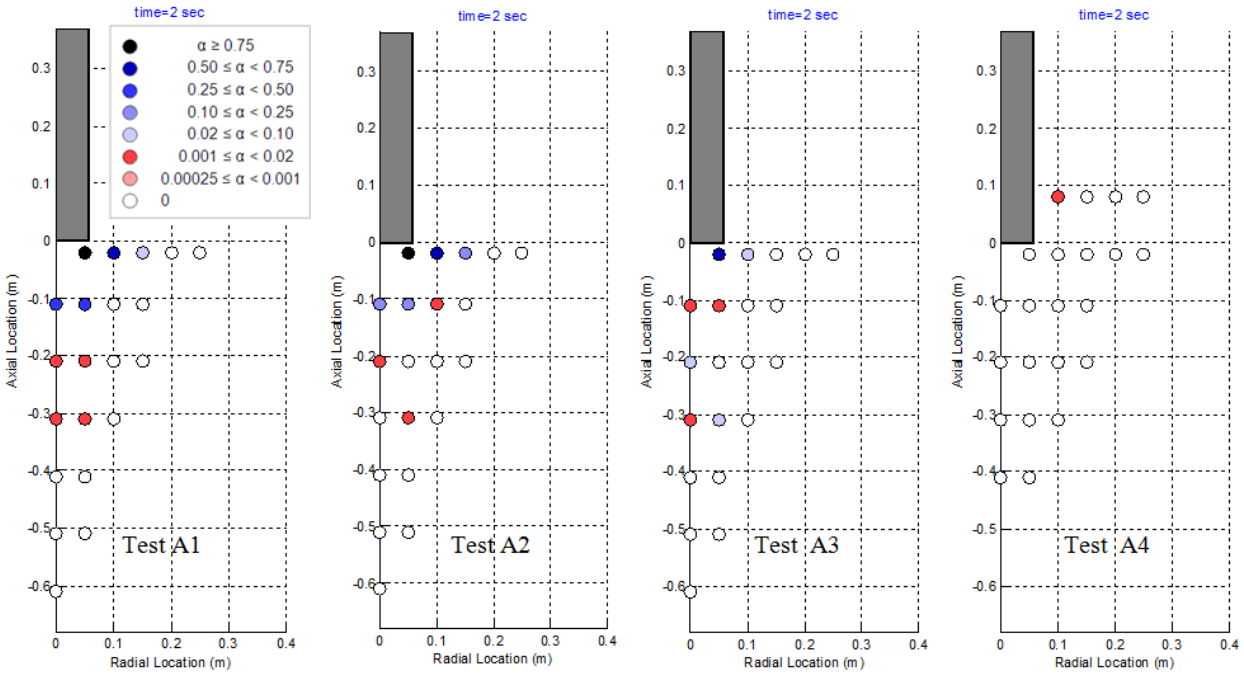

Figure 4-4 Void Fraction Distribution During the Initial Period (t=2 sec) for Test Nos. A1, A2, A3, and A4

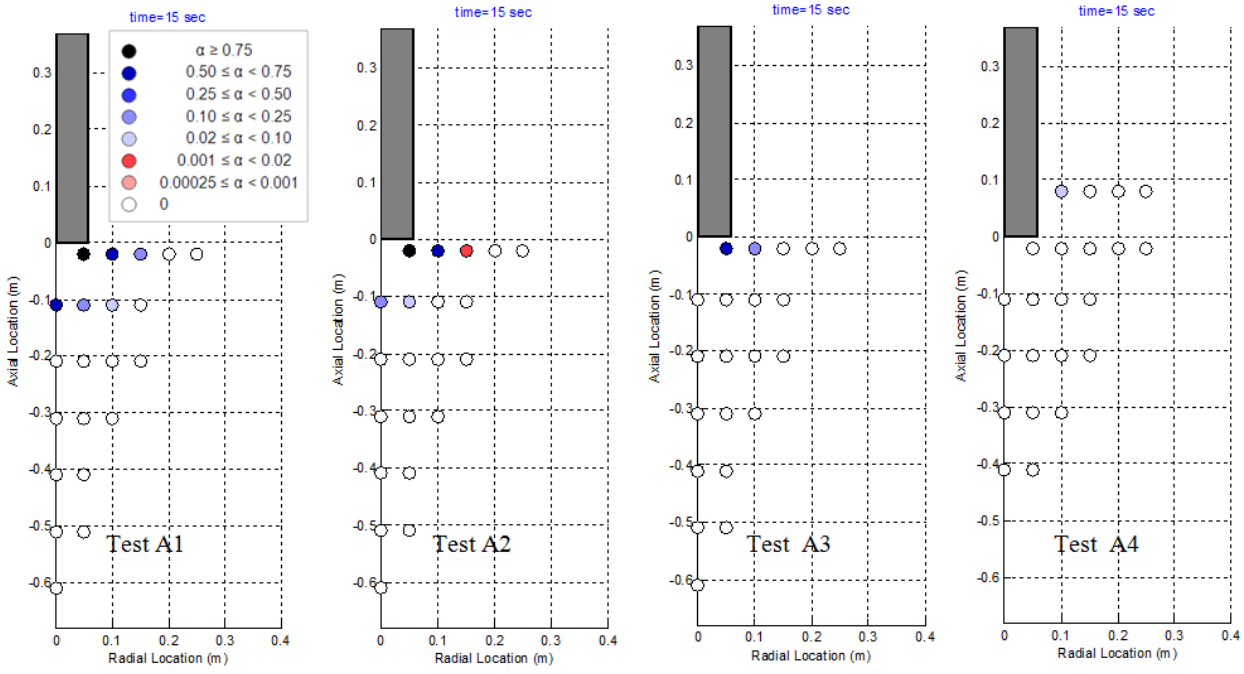

Figure 4-5 Void Fraction Distribution During the Quasi-steady Period (t=15 sec) for Test Nos. A1, A2, A3, and A4

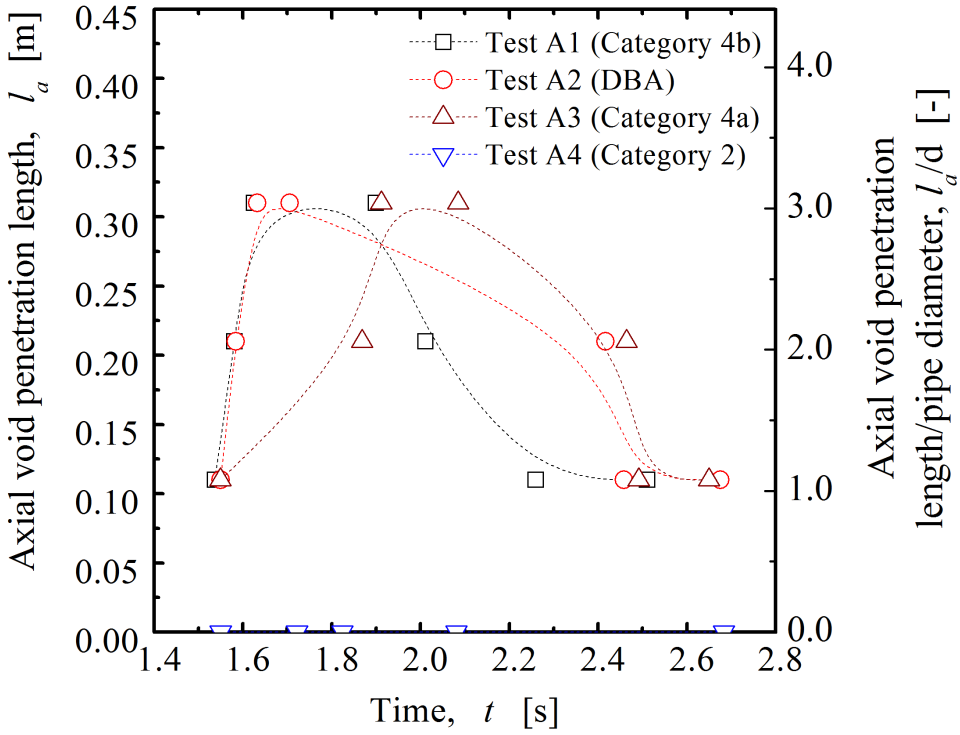

Figure 4-6 Axial Void Penetration During the Initial and Quasi-steady Periods for Test Nos. A1, A2, A3, and A4 Measured Using the Conductivity Probes

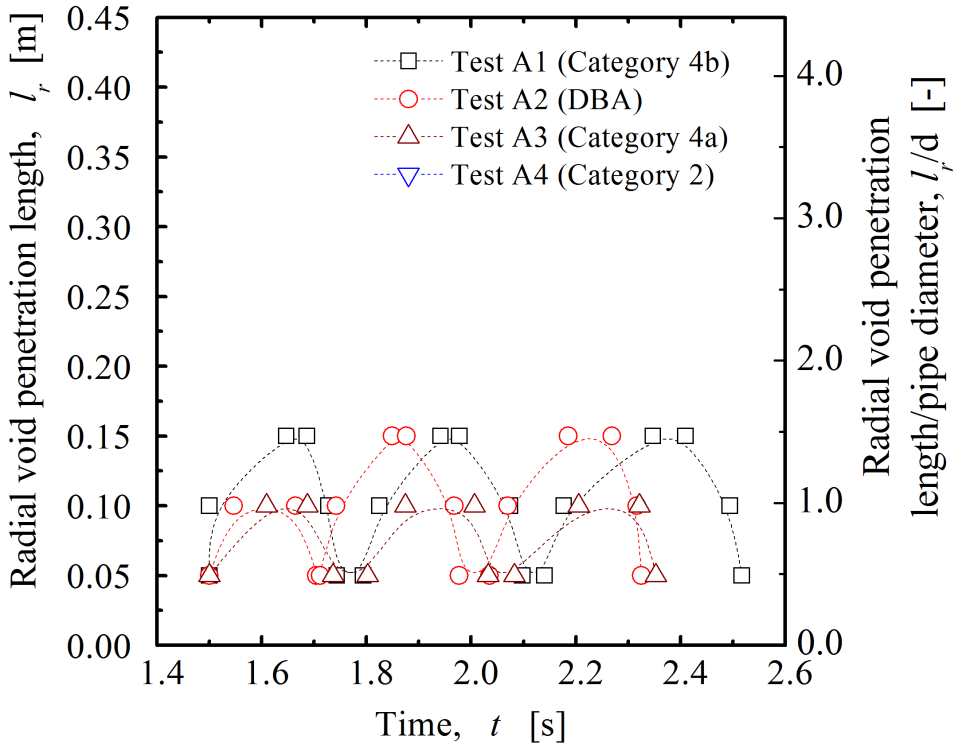

Figure 4-7 Radial Void Penetration During the Initial and Quasi-steady Periods for Test Nos. A1, A2, and A3 Measured Using the Conductivity Probes

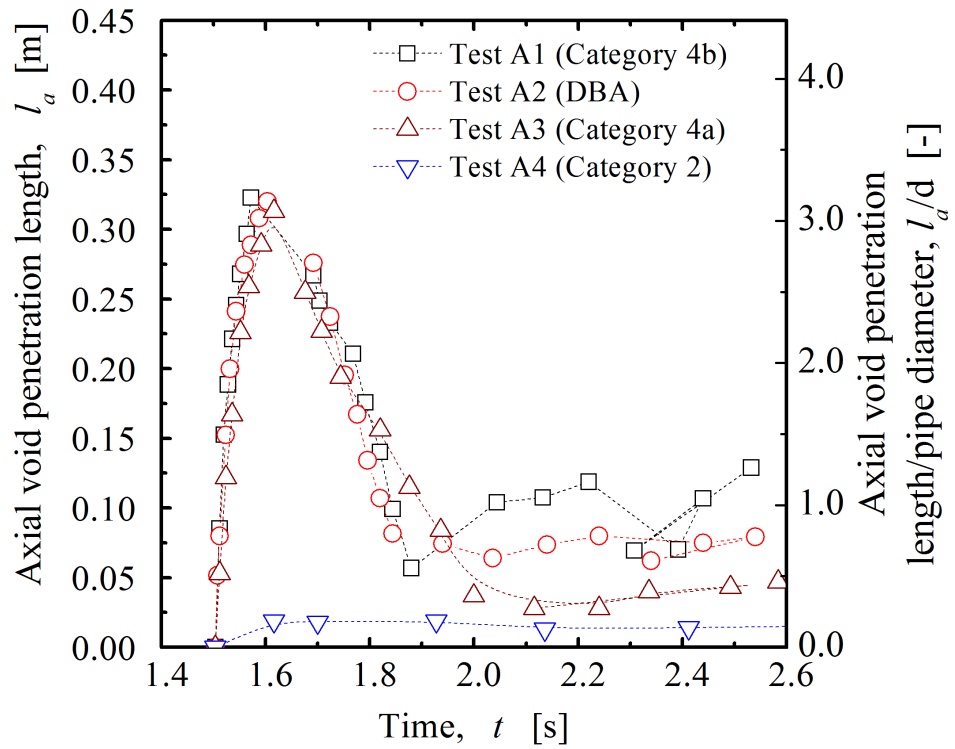

Figure 4-8 Axial Void Penetration During the Initial and Quasi-steady Periods for Test Nos. A1, A2, A3, and A4 Estimated From the High-speed Camera Images

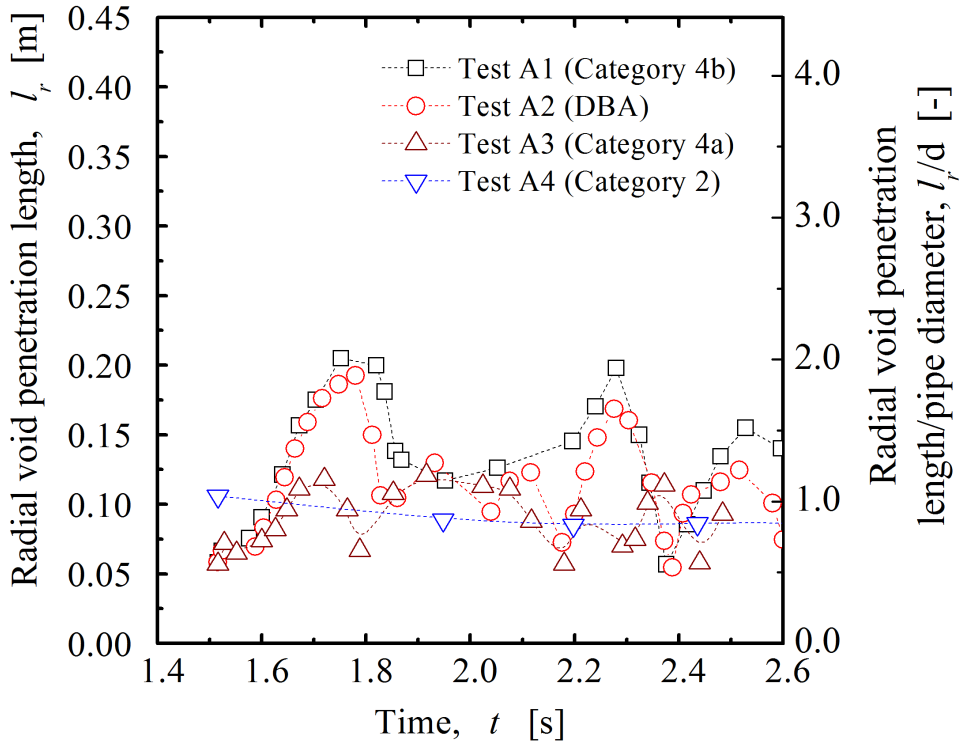

Figure 4-9 Radial Void Penetration During the Initial and Quasi-steady Periods for Test Nos. A1, A2, A3, and A4 Estimated From the High-speed Camera Images

As seen in Figure 4-3, the different volumetric flow rates with air velocity ramp rate times of 1 second were obtained from the different test conditions. As seen in Figure 4-4, the void fraction distribution during the initial period for tests with high air volumetric flow rates (tests Nos. A1, A2, and A3) showed little difference in terms of the void penetration and void distribution. However, from Figure 4-5, it is clear that the void distribution during the quasi-steady period is determined by the air volumetric flow rate through the downcomer section.

From a comparison of Figures 4-6 and 4-8 and Figures 4-7 and 4-9 it is evident that there is some small difference between the void penetration trend obtained using the conductivity probes and estimated from the high-speed camera images. This difference is caused by the method used to determine the void penetration. The void penetration obtained using the conductivity probes represents the bubble plume making direct contact with a probe. The estimated value from the high-speed camera images represents the estimated boundary of the bubble plume observed. There is agreement, however, in the general trend of axial and radial void penetration between the values determined by both methods. During the initial air injection period, the axial void penetration (as measured by the conductivity probes) would increase to the maximum point at a certain time and decreased to a lesser point at a later time. The void penetration then oscillated axially and radially. The size of oscillations varied as a function of the test conditions during the quasi-steady period. These trends correspond to the observations made from the high-speed camera images. In the low volumetric flow condition (test No. A4), only small bubbles, and not a bubble plume, emerged intermittently from the exit of the downcomer.

Consequently, it can be concluded that the air volumetric flow rate has a minor effect on void fraction distribution and axial void penetration in the SP during the initial period for high air volumetric flow rate conditions. The air volumetric flow rate has a greater impact on void fraction distribution and axial void penetration in the SP during the quasi-steady period for the entire range of air volumetric flow rate conditions. The air volumetric flow rate has a significant effect on the radial void penetration for both periods.

4.1.3. Initial Downcomer Void Condition

The results of test Nos. A1 and A5 (test conditions shown in Table 4-4) are compared to illustrate the impact of the initial downcomer void condition on the void penetration and void distribution in the SP. Table 4-5 provides a description of each figure used to determine the effect of initial downcomer void condition on void penetration and distribution in the SP. Interpretation of the data in the figures is similar to that explained in Section 4.1.2.

Table 4-4 Test Conditions for Comparison of the Initial Downcomer Void Condition Effect on Void Distribution and Void Penetration in the SP.

Test No.	DC Diameter	Air Velocity Ramp Rate (s)	DC Condition	Prototypic Plant Flow Type	Air Mass Flow Rate (kg/s [lbm/s])	Air Volumetric Flow Rate (m^3/s [ft^3/s])	Air Volumetric Flux (m/s [ft/s])
A1	0.102 m (4 in.)	1.0	Fully Water	Category 4b	0.184 [0.406]	0.153 [5.403]	18.9 [62.0]
A5			Partially Void				

Table 4-5 Description of Figures for Determining the Effect of Downcomer Initial Void Condition on Void Penetration and Distribution in the SP.

Figure No.	Figure Descriptions	Experimental Period	Measurement Device
4-10	Local Void Distribution	Initial	Conductivity Probes
4-11	Local Void Distribution	Quasi-steady	Conductivity Probes
4-12	Axial Void Penetration	Initial and Quasi-steady	Conductivity Probes
4-13	Radial Void Penetration	Initial and Quasi-steady	Conductivity Probes
4-14	Axial Void Penetration	Initial and Quasi-steady	High-speed Camera
4-15	Radial Void Penetration	Initial and Quasi-steady	High-speed Camera

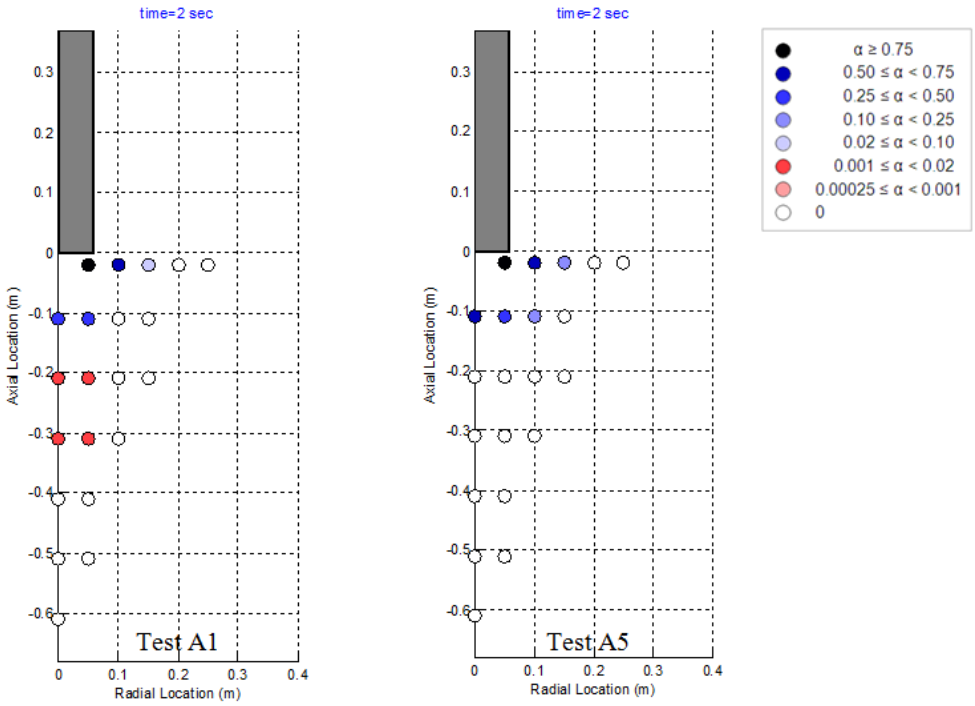

Figure 4-10 Void Fraction Distribution During the Initial Period (t=2 sec) for Test Nos. A1 and A5

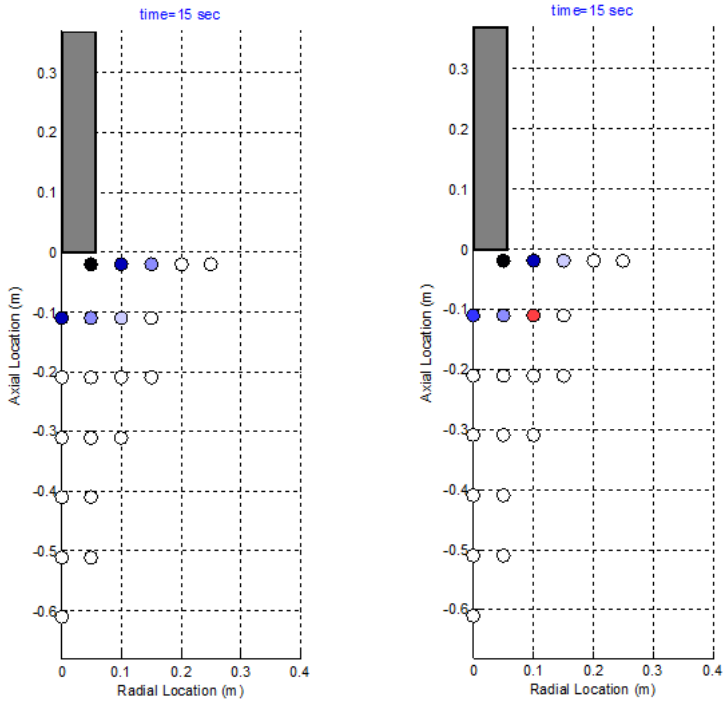

Figure 4-11 Void Fraction Distribution During the Quasi-steady Period (t=15 sec) for Test Nos. A1 and A5

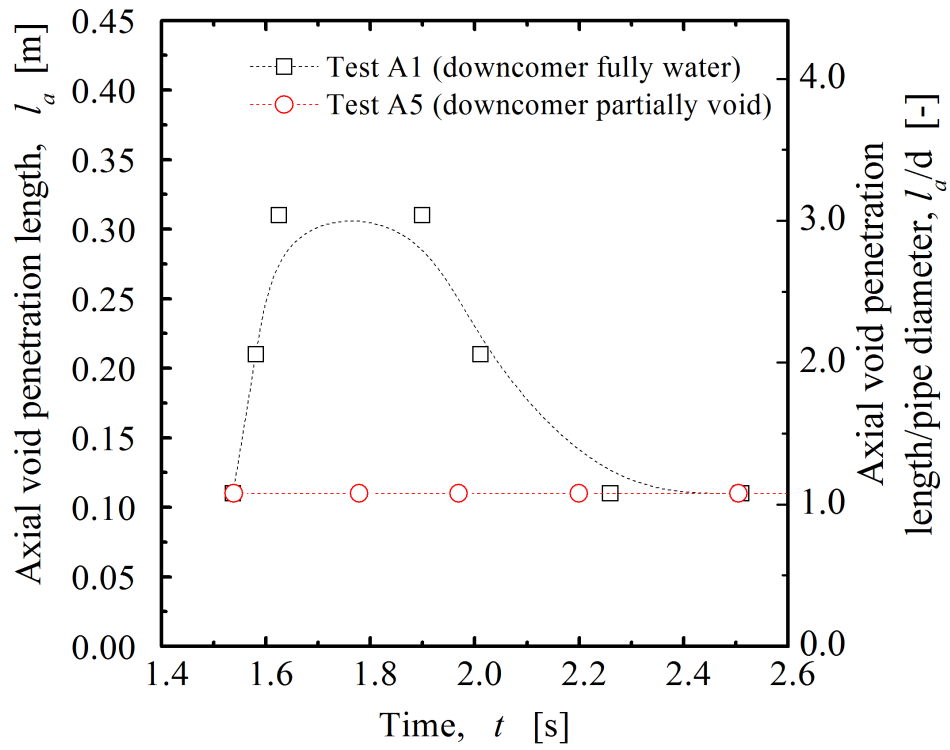

Figure 4-12 Axial Void Penetration During the Initial and Quasi-steady Periods for Test Nos. A1 and A5 Measured Using the Conductivity Probes

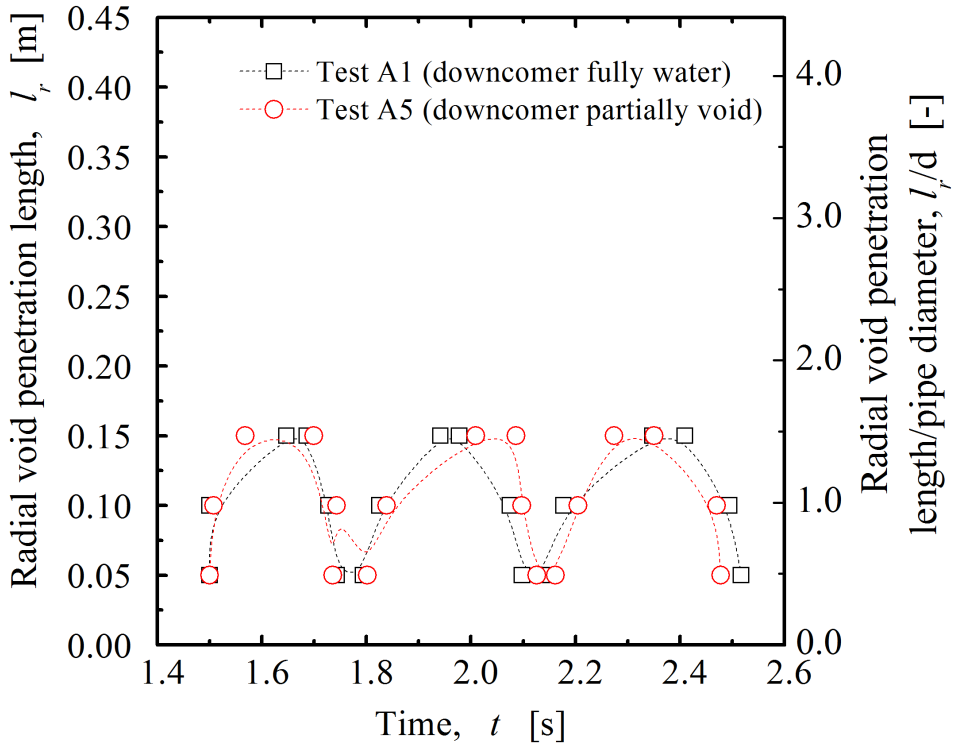

Figure 4-13 Radial Void Penetration During the Initial and Quasi-steady Periods for Test Nos. A1 and A5 Measured Using the Conductivity Probes

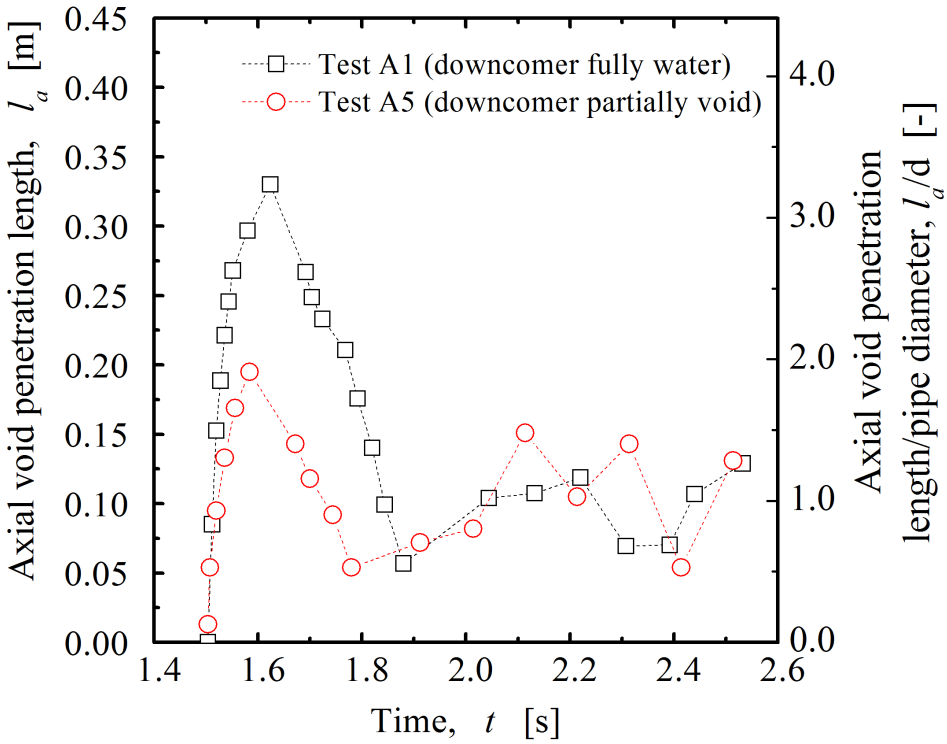

Figure 4-14 Axial Void Penetration During the Initial and Quasi-steady Periods for Test Nos. A1 and A5 Estimated From the High-speed Camera Images

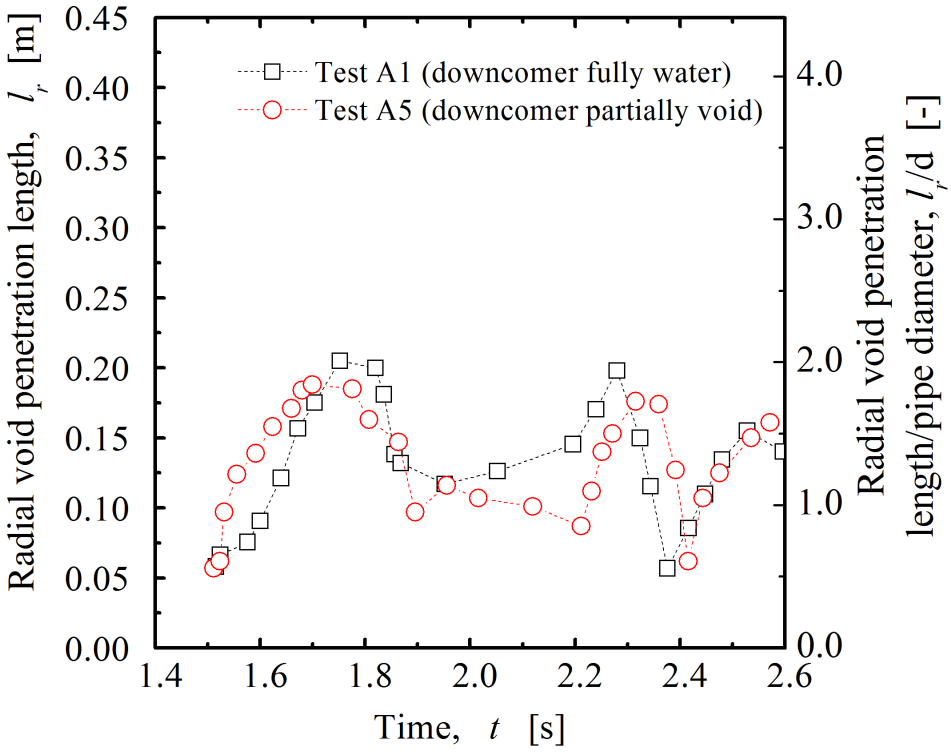

Figure 4-15 Radial Void Penetration During the Initial and Quasi-steady Periods for Test Nos. A1 and A5 Estimated From the High-speed Camera Images

From Figures 4-10 and 4-11, it can be seen that the downcomer void condition has a significant impact on the void distribution and penetration during the initial air injection period and has almost no impact in the quasi-steady period. As shown in Figures 4-12 and 4-14, the maximum axial void penetration depth observed from the high-speed camera images and measured by the conductivity probes show that the maximum axial void penetration for test No. A1 is higher than for test No. A5. It is clear that the initial height of liquid slug in the downcomer affects the maximum axial void penetration depth. A higher initial water column in the downcomer results in a larger initial liquid slug and induces more liquid recirculation, resulting in increased entrainment of bubbles into the liquid flow. For the radial void penetration, both profiles are quite similar as displayed in Figures 4-13 and 4-15. Therefore, the initial downcomer water column height has almost no impact on the radial void penetration. In the prototypic plant, there is a differential pressure between the DW and SP. This creates a partial void condition in the downcomers. This partial void may be significant in terms of reducing the risk of air bubble entrainment into the ECCS pump suction piping when it is installed in close proximity to the downcomer exit.

4.1.4. Air Velocity Ramp Rate

The results of test Nos. A1 and A9 (test conditions shown in Table 4-6) are compared to illustrate the effect of the air velocity ramp rate on void fraction distribution and void penetration. Table 4-7 provides a description of each figure used to determine the effect of air velocity ramp rate void penetration and distribution in the SP. Interpretation of the data in the figures is similar to that explained in Section 4.1.2.

Table 4-6 Test Conditions for Comparison of the Air Velocity Ramp Rate Effect on Void Distribution and Void Penetration in the SP.

Test No.	DC Diameter	Air Velocity Ramp Rate (s)	DC Condition	Prototypic Plant Flow Type	Air Mass Flow Rate (kg/s [lbm/s])	Air Volumetric Flow Rate (m^3/s [ft^3/s])	Air Volumetric Flux (m/s [ft/s])
A1	0.102 m (4 in.)	1.0	Fully Water	Category 4b	0.184 [0.406]	0.153 [5.403]	18.9 [62.0]
A9		2.0					

Table 4-7 Description of Figures for Determining the Effect of the Air Velocity Ramp Rate on Void Penetration and Distribution in the SP.

Figure No.	Figure Descriptions	Experimental Period	Measurement Device
4-16	Measured Air Volumetric Flow Rate	Initial to Quasi-steady	Vortex Flow Meter
4-17	Local Void Distribution	Initial	Conductivity Probes
4-18	Local Void Distribution	Quasi-steady	Conductivity Probes
4-19	Axial Void Penetration	Initial and Quasi-steady	Conductivity Probes
4-20	Radial Void Penetration	Initial and Quasi-steady	Conductivity Probes
4-21	Axial Void Penetration	Initial and Quasi-steady	High-speed Camera
4-22	Radial Void Penetration	Initial and Quasi-steady	High-speed Camera

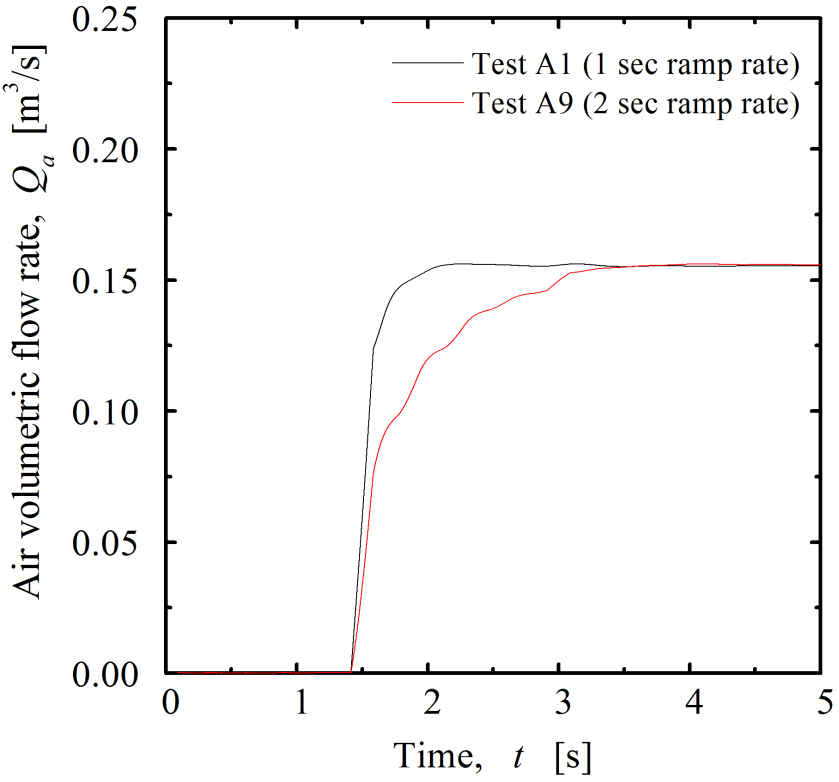

Figure 4-16 Measured Air Volumetric Flow Rate for Test Nos. A1 and A9

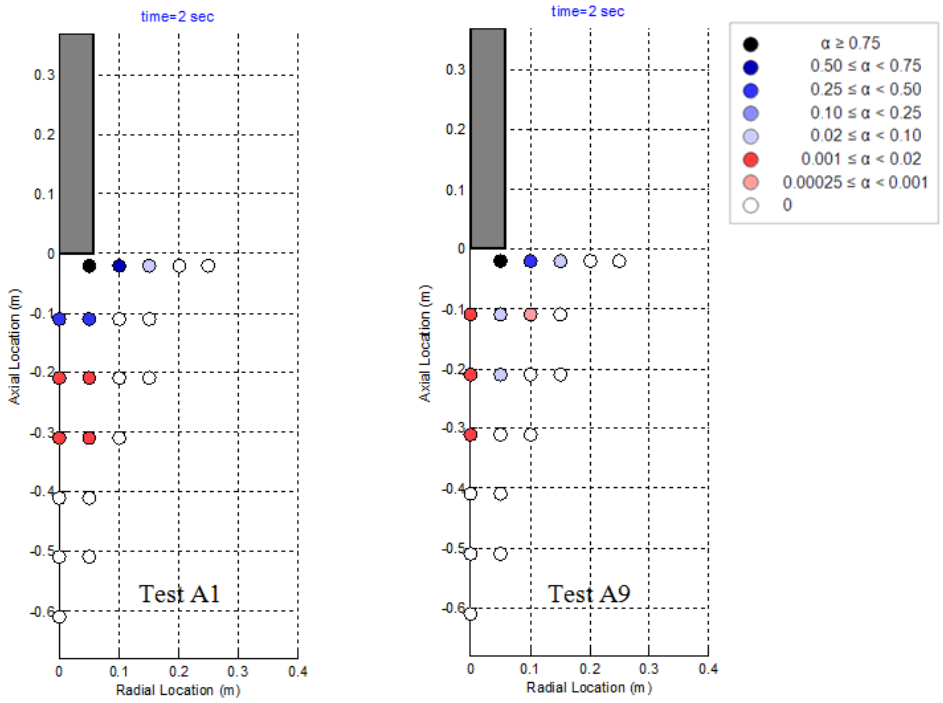

Figure 4-17 Void Fraction Distribution During the Initial Period (t=2 sec) for Test Nos. A1 and A9

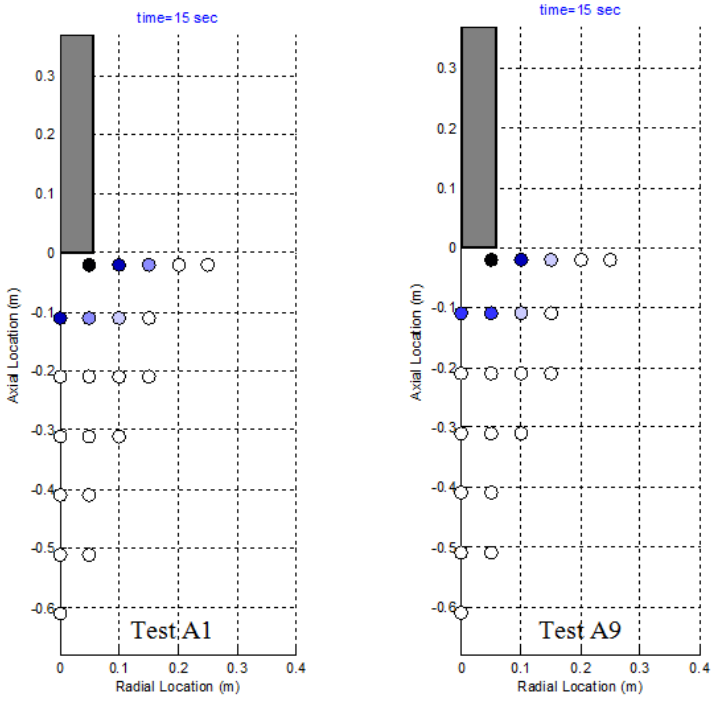

Figure 4-18 Void Fraction Distribution During the Quasi-steady Period (t=15 sec) for Test Nos. A1 and A9

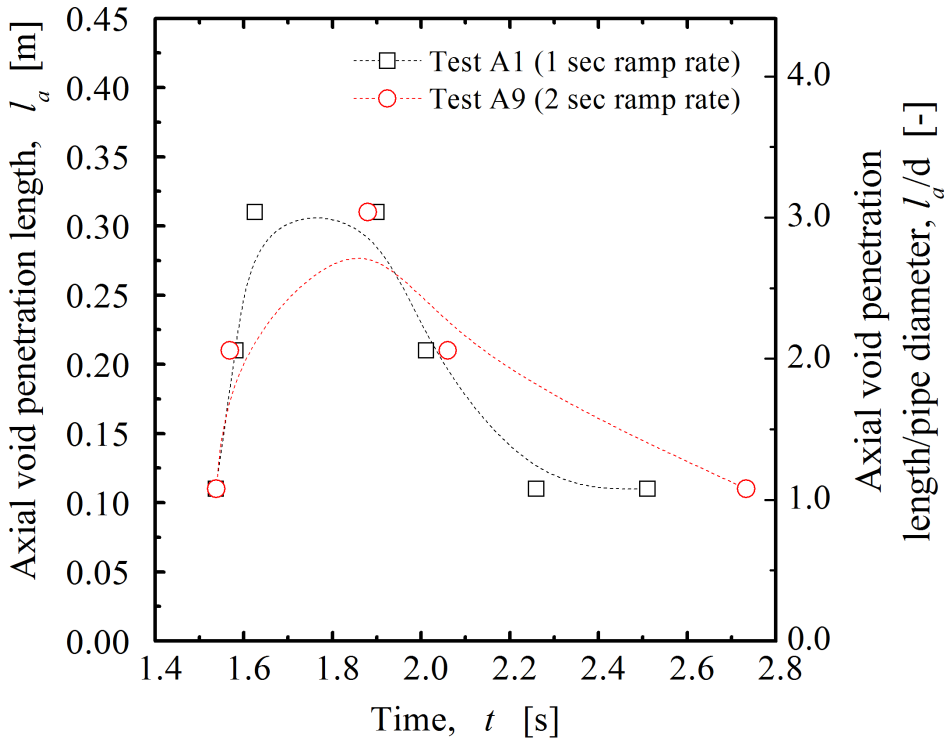

Figure 4-19 Axial Void Penetration During the Initial and Quasi-steady Periods for Test Nos. A1 and A9 Measured Using the Conductivity Probes

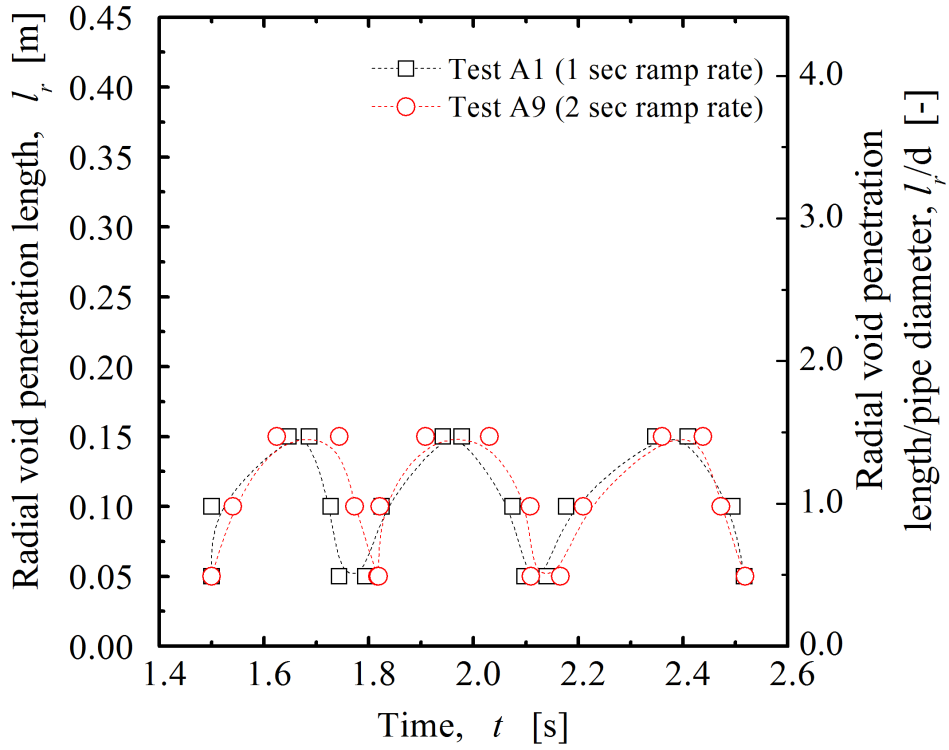

Figure 4-20 Radial Void Penetration During the Initial and Quasi-steady Periods for Test Nos. A1 and A9 Measured Using the Conductivity Probes

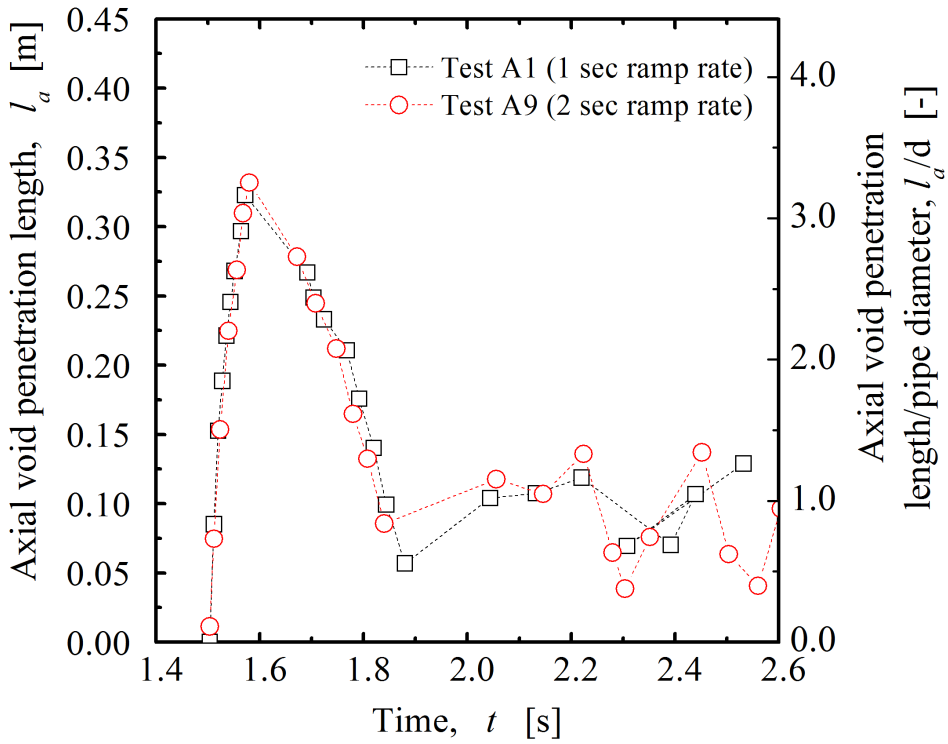

Figure 4-21 Axial Void Penetration During the Initial and Quasi-steady Periods for Test Nos. A1 and A9 Estimated From the High-speed Camera Images

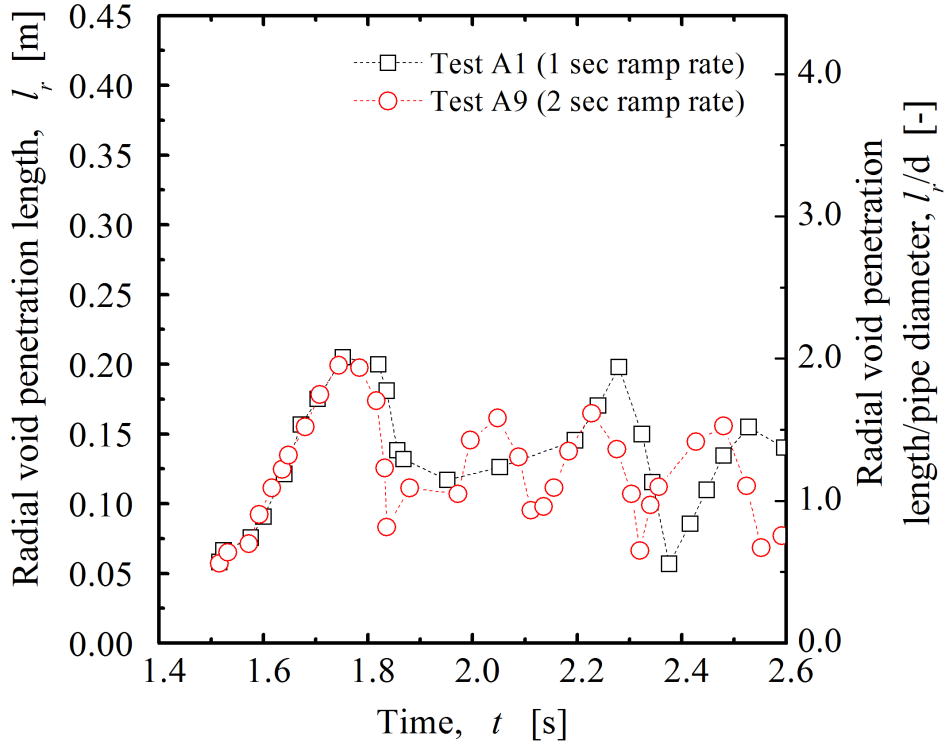

Figure 4-22 Radial Void Penetration During the Initial and Quasi-steady Periods for Test Nos. A1 and A9 Estimated From High-speed Camera Images

As seen in Figures 4-17 and 4-18, the air velocity ramp rate has a minor impact on the void distribution during the initial air injection period and the quasi-steady period. The axial void penetration trends are similar for both cases as shown in Figures 4-19 and 4-21. The radial void penetrations for both cases also have similar trends as displayed in Figures 4-20 and 4-22. There is no significant difference in void fraction distribution or void penetration for test conditions with an air velocity ramp rate of 1 and 2 seconds. The averaged liquid slug ejection (from the downcomer) velocity estimated from the high-speed camera images was 2.31 and 2.15 m/s (7.58 and 7.05 ft/s) for the case of the air velocity ramp rate of 1 (Test A1) and 2 (Test A5) seconds, respectively. The void distribution and penetration during the initial air injection period is impacted by this liquid slug velocity. There is no significant difference in terms of void faction and penetration between tests A1 and A5 since the liquid slug velocity is similar for both cases. In order to determine the impact of the air velocity ramp rate on the void fraction distribution, a range of tests with air velocity ramp rates that significantly differ may be required.

4.1.5. Averaged Bubble Velocity and Bubble Chord Length.

Table 4-8 shows the averaged axial bubble velocity and chord length measured using the double-sensor conductivity probes for each steady state test condition. It is noted that only some air bubbles were detected and measured by the conductivity probes. For general results, it can be seen that averaged bubble velocities ranged between 0.24 and 1.83 m/s (0.79 and 6.0 ft/s) for the upward velocity and between 0.43 and 0.64 m/s (1.4 and 2.1 ft/s) for the downward velocity. The measured upward air bubble velocity was higher for the conditions with the higher air volumetric flow rates. The averaged bubble chord length ranged between 0.010 to 0.363 m (0.39 to 14.3 in.). It is noted that the averaged downward bubble velocity could not be estimated in low air volumetric flow rate conditions (indicated by “-” in Table 4-8) since the bubble plume size in the quasi-steady period is limited. The bubbles in these low air volumetric flow rate conditions did not contact the probes located below C level. The probes below C level were used for measuring the downward bubble velocity as explained in Section A.1.2.1.

Table 4-8 Averaged Axial Bubble Velocity and Chord Length for the Steady State Tests.

Test No.	Averaged Upward Bubble Velocity (m/s [ft/s])	Averaged Downward Bubble Velocity (m/s [ft/s])	Averaged Bubble Chord Length (m [in])
A1	1.31 [4.30]	0.59 [1.94]	0.155 [6.1]
A2	1.83 [6.00]	0.49 [1.61]	0.216 [8.5]
A3	1.06 [3.48]	-	0.102 [4.02]
A4	0.33 [1.08]	-	0.01 [0.39]
A5	1.7 [5.58]	0.55 [1.80]	0.203 [7.99]
A6	1.58 [5.18]	0.5 [1.64]	0.214 [8.43]
A7	0.97 [3.18]	-	0.11 [4.33]
A8	0.3 [0.98]	-	0.011 [0.43]
A9	1.79 [5.87]	0.57 [1.87]	0.207 [8.15]
A10	1.74 [5.71]	0.43 [1.41]	0.363 [14.29]
A11	0.86 [2.82]	-	0.075 [2.95]
A12	0.47 [1.54]	-	0.025 [0.98]
A13	1.73 [5.68]	0.64 [2.10]	0.185 [7.28]
A14	1.61 [5.28]	0.43 [1.41]	0.221 [8.7]
A15	0.97 [3.18]	-	0.155 [6.1]
A16	0.24 [0.79]	-	0.01 [0.39]

4.2. Transient Tests

During a LOCA blowdown, the noncondensable gas concentration in the Mark I containment will decrease as air is replaced by steam from the break. The rate of this replacement is governed by the break size. While the steady state tests were performed using air to parametrically study the local physical phenomena in the SP during the blowdown phase of a LOCA, the transient tests used a steam-air mixture. The purpose of the transient tests was to simulate the effects of noncondensable gas concentration and gas volumetric flux on void penetration and distribution in the SP. In addition, two downcomers of different diameter were used for examining the effect downcomer diameter has on void penetration and distribution in the SP.

4.2.1. Important Differences Between the Steady State and Transient Tests

The most obvious difference between the steady state and transient tests is the test gas used. In the steady state tests, the gas used was air for the duration of each test. In the transient test, the gas used was a steam-air mixture of which the steam-to-air ratio increased as each transient test progressed. The difference in test gases leads to further differences in the steady state and transient tests. These additional differences are discussed in detail below.

Three distinct periods of blowdown were observed during each transient test: the initial period, the quasi-steady period, and the chugging period. The details of each transient test period are described in Section 4.2.3.

During the steady state tests, two distinct periods of blowdown were observed: the initial period and the quasi-steady period. The details of each steady state period are described in Section 4.1.1. The chugging period was not observed during the steady state tests because it is caused by a steam-air mixture with low noncondensable gas concentration, which was only present during the later time of the transient tests.

The other important difference between the steady state and transient tests is role of the DW. In the transient tests the DW was utilized as a steam supply, whereas in the steady state tests the downcomer pipe was connected directly to the compressed air line. Therefore, in the transient tests, the DW volume needed to be pressurized by steam from the RPV before the liquid slug in the downcomer was ejected from the downcomer. During the steady state tests, once the test was initiated by opening the valves, the downcomer was immediately pressurized. The result was that the liquid slug in the downcomer was ejected with a higher velocity during the steady state test than for a comparable transient test. For example, for the steady state test with an air velocity of 14.2 m/s (46.6 ft/s) (Test No. A1), the liquid slug was ejected at an averaged velocity of 2.31 m/s (7.58 ft/s) (estimated from images taken with the high-speed camera). For the transient test with an initial gas velocity of 17 m/s (56 ft/s) (0.102 m [4 in.] downcomer, 2 DPV break size with a 100% initial air concentration in the DW), the liquid slug was ejected at an averaged velocity 0.38 m/s (1.25 ft/s) according to the data obtained using conductivity probes in the downcomer. Consequently, the maximum axial void penetration depth realized during the initial period of the transient tests and the steady state tests cannot be compared directly without consideration of the difference in liquid slug ejection velocity from the downcomer.

The focus of the current transient tests was the initial period of a LOCA blowdown. Thus the test conditions were well scaled for the initial period but not necessarily well scaled to simulate the chugging phenomena. Chugging is dependent on the gas volumetric flux, noncondensable gas concentration, and subcooling. It is necessary to parametrically study the chugging phenomena to better develop a model and investigate its importance to gas intrusion in ECCS suction piping.

4.2.2. Flow Visualization for the Transient Tests

Figures 4-23 and 4-24 highlight the development of the bubble plume around the downcomer exit in the SP. The images were recorded by the high-speed camera during the initial period of blowdown during transient test No. T5, so that the development of the bubble plume during the initial gas injection period could be observed and described. First, the gaseous mixture (almost 100% air) was injected into the SP through the downcomer after pressurizing the DW. The initial injected gas was then pulled toward the bottom of the SP by the wake of the liquid slug ejected from the downcomer. A spherically shaped bubble plume was formed at the exit of the downcomer, eventually rising to the surface of the water due to the buoyancy force.

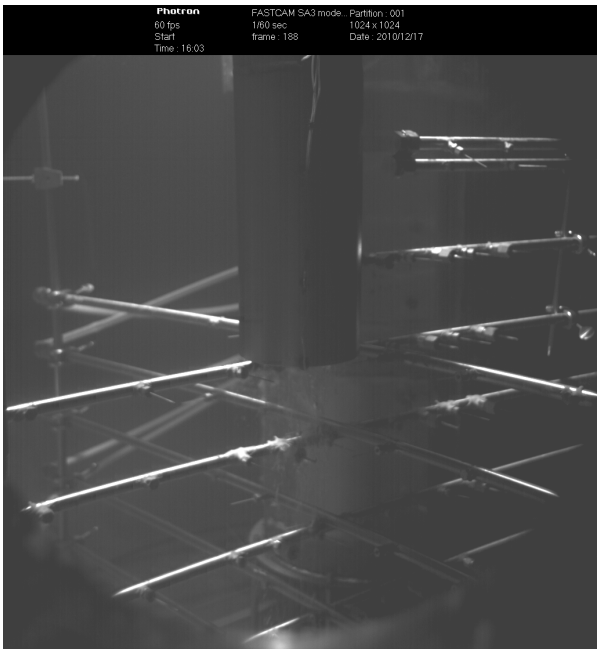

Time = 3.13 seconds

Time = 3.40 seconds

Time = 3.80 seconds

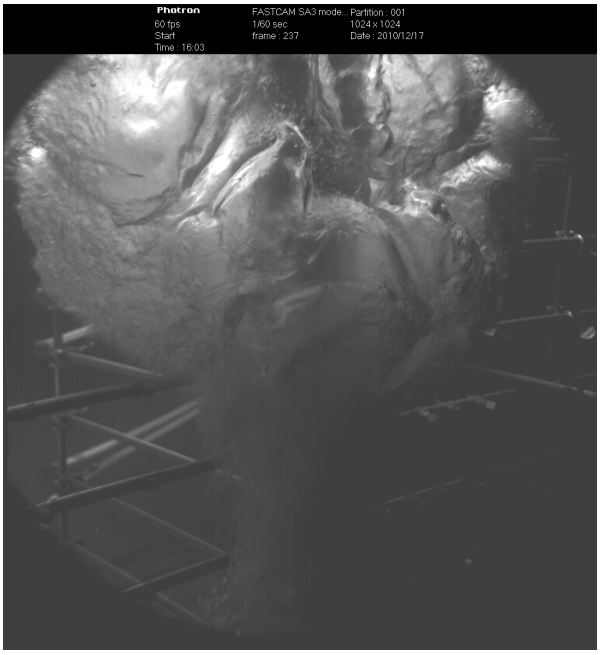

Time = 3.93 seconds

Figure 4-23 Bubble Plume Around the Downcomer Exit During t=3.13-3.93 Seconds for Test No. T5 (Based on the High-speed Camera Time)

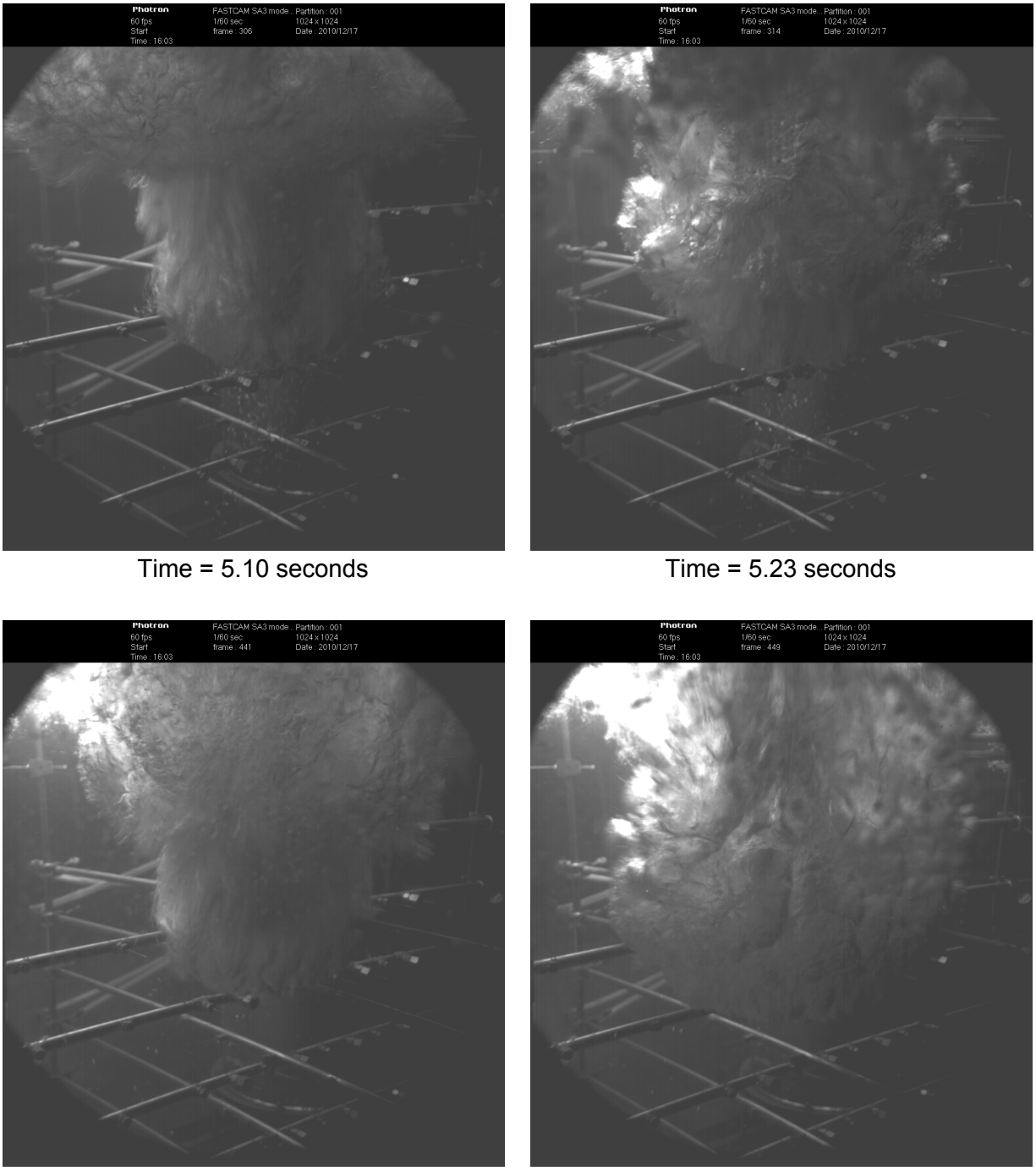

Figure 4-24 Bubble Plume Around the Downcomer Exit During t=5.10-7.48 Seconds for Test No. T5 (Based on the High-speed Camera Time)

Figure 4-25 highlights the development of the bubble plume around the downcomer exit in the SP recorded by the high-speed camera during the quasi-steady period of blowdown during transient test No. T5. The bubble plume oscillated throughout this period with little change to axial or radial penetration depth. However, the penetration depth of this bubble plume was much

less compared to the initial period penetration since there were no liquid slug inertial forces to pull the bubble downward.

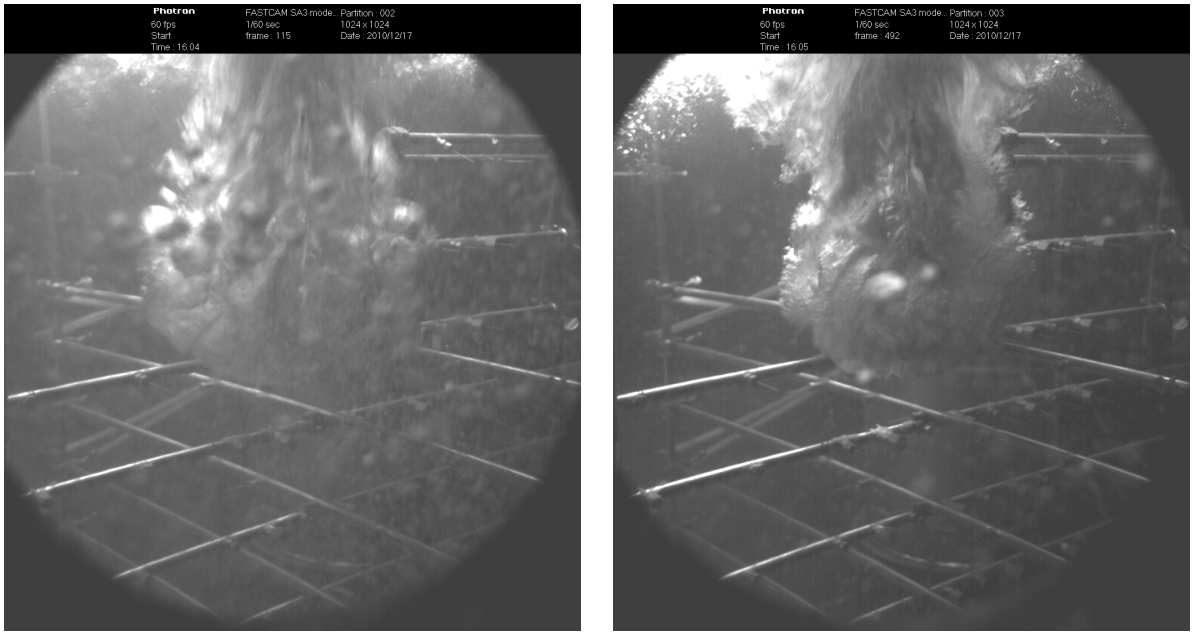

Time = 31.93 seconds Time = 68.20 seconds

Figure 4-25 Bubble Plume Around the Downcomer Exit During t=31.93 and 68.20 Seconds for Test No. T5 (Based on the High-speed Camera Time)

Figure 4-26 highlights the development of the bubble plume around the downcomer exit in the SP recorded by the high-speed camera during the chugging period of blowdown during transient test No. T5. While there was no distinct bubble plume during this period, small bubbles were randomly ejected from the downcomer. The penetration depth of these small bubbles was greater than the penetration depth of the plume in the quasi-steady period but less than the penetration depth of the initial plume since there were no liquid slug inertial forces to pull the bubble downward.

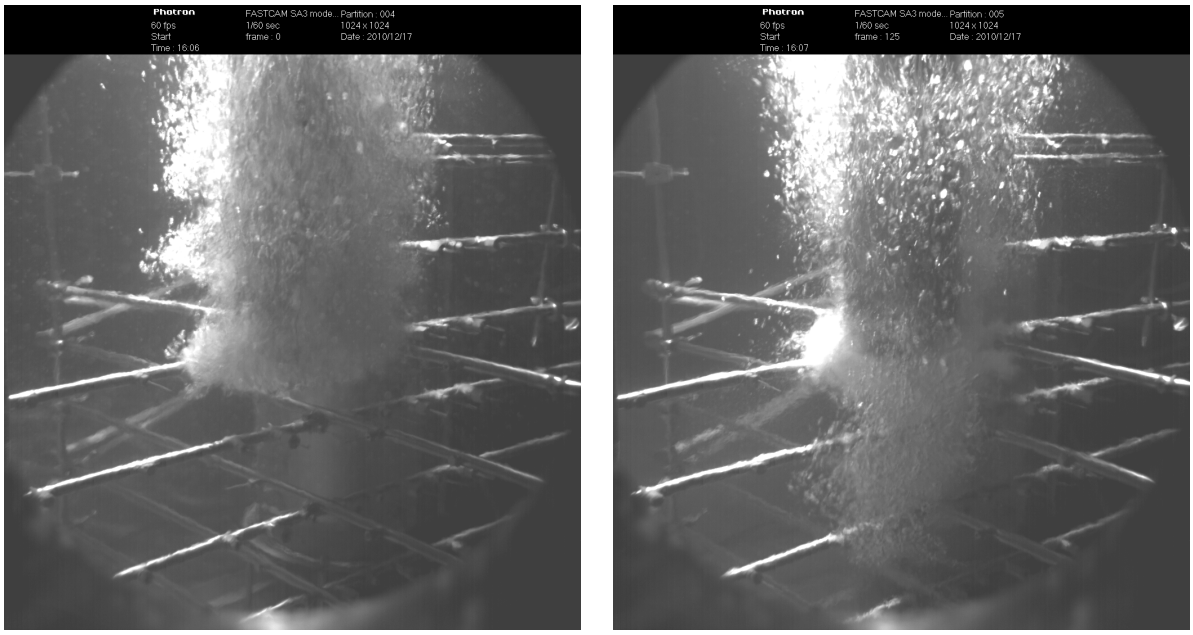

Time = 300.00 seconds Time = 542.08 seconds

Figure 4-26 Bubble Plume Around the Downcomer Exit During t=300 and 542.08 Seconds for Test No. T5 (Based on the High-speed Camera Time)

4.2.3. Transient Test Blowdown Periods

Three periods of blowdown (initial, quasi-steady, chugging) were observed during each transient test experiment. The initial period was caused by the ejection of the liquid slug from the downcomer into the SP. The quasi-steady period consisted of oscillations in the bubble plume caused by condensation and pressure oscillations at the exit of the downcomer. The chugging period was caused by the eventual reduction in noncondensable gas concentration in the DW to some threshold value. The axial depth and radial size of the void penetration were observed to be maximum during the initial period and reduced in the quasi-steady period. The time at which the chugging period was observed varied by test flow condition. The axial depth and radial size of the void penetration during the chugging period were larger than those observed during the quasi-steady period, although a bubble plume did not exist during the chugging period. Instead, small bubbles were observed to be ejected from the exit of the downcomer at random intervals.

The onset time for chugging is earlier during transient tests with the highest volumetric flow rates (5 DPVs) than the tests with lower volumetric flow rates (3 DPVs and 2 DPVs). Also, the data suggests that the initial noncondensable gas concentration in the DW affected the onset time of chugging. For comparable break flows, the average time of chugging onset was slightly lower for the transient tests with 80% initial noncondensable gas concentration compared to the tests with 100% initial noncondensable gas concentration. However, any definitive conclusions regarding the effect of noncondensable gas concentration on the time of chugging onset requires additional data. Chugging onset time ranges for each transient test are provided in Table 4-9.

Table 4-9 Chugging Onset Time Range for Each Transient Test.

Test No.	Break Flow (DPVs)	Initial DW Noncondensable Gas Concentration (%)	Chugging Onset Time Range (s)
T1	5	100	210-270
T2	3	100	180-240
T3	2	100	310-370
T4	5	80	220-280
T5	5	100	160-220
T6	3	100	445-505
T7	2	100	330-390
T8	5	80	120-180

Figures 4-27 and 4-28 show the axial void penetration and the radial void penetration, respectively, as a function of time for each period of transient test Nos.: T1, T2, T3, and T4 (0.076 m [3 in.] downcomer tests). Figures 4-29 and 4-30 show the axial void penetration and the radial void penetration, respectively, as a function of time for each period of transient test Nos.: T5, T6, T7, and T8 (0.102 m [4 in.] downcomer tests). Each of these Figures, 4-27 through 4-30, show estimated values based on images taken with the high-speed camera. The high-speed camera was used because it provided a very clear portrait of the three periods for each transient test condition. Note that for the initial period, all high-speed camera times were shifted to a common start time in order to be able to make a good comparison between the different tests.

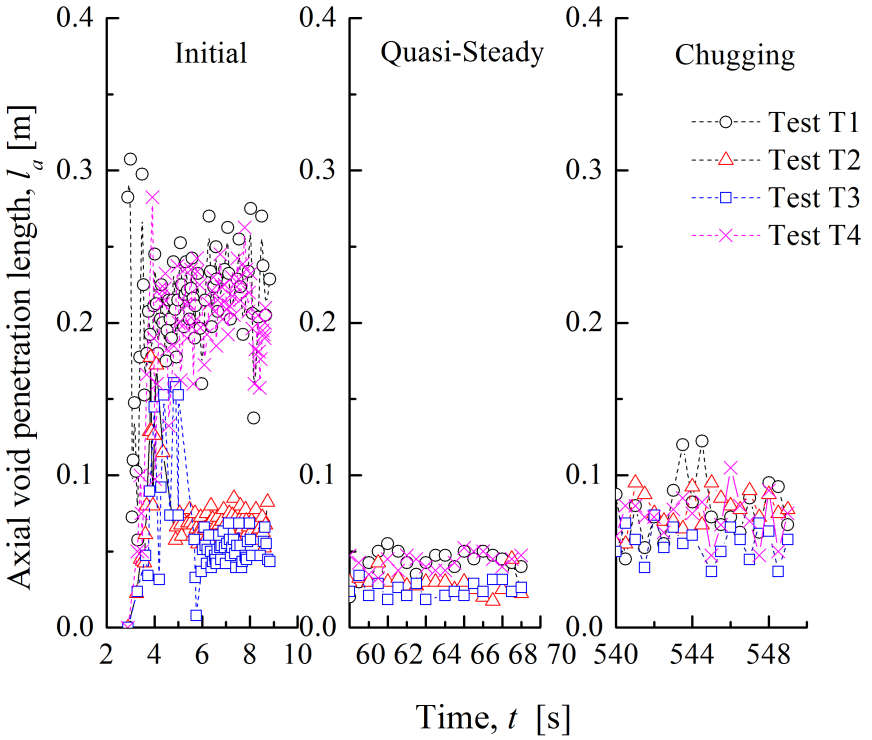

Figure 4-27 Axial Void Penetration as a Function of Time for Each Period of Transient Test Nos. T1, T2, T3, and T4

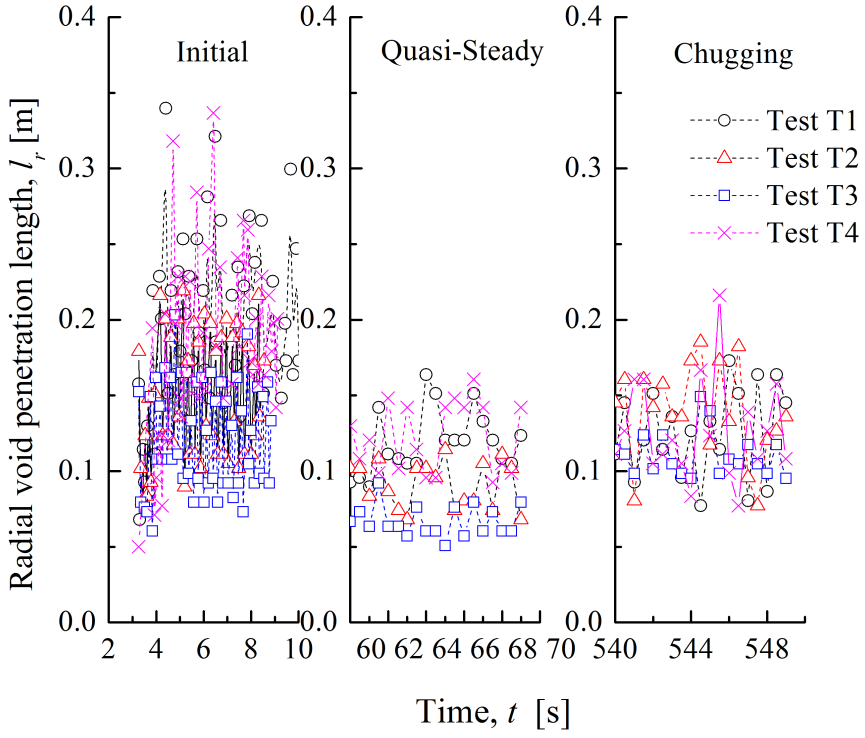

Figure 4-28 Radial Void Penetration as a Function of Time for Each Period of Transient Test Nos. T1, T2, T3, and T4

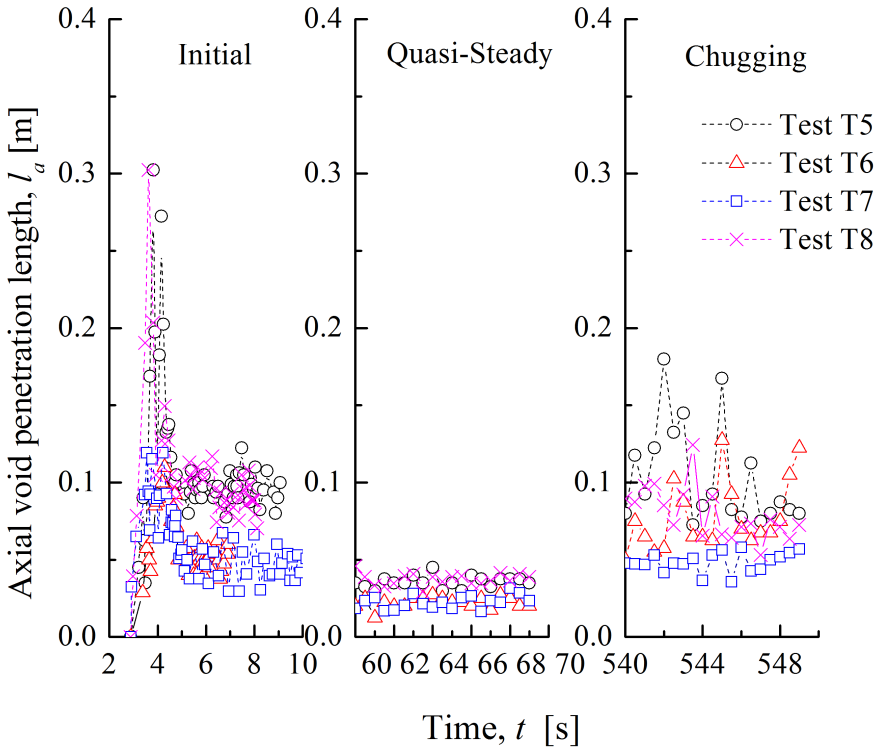

Figure 4-29 Axial Void Penetration as a Function of Time for Each Period of Transient Test Nos. T5, T6, T7, and T8

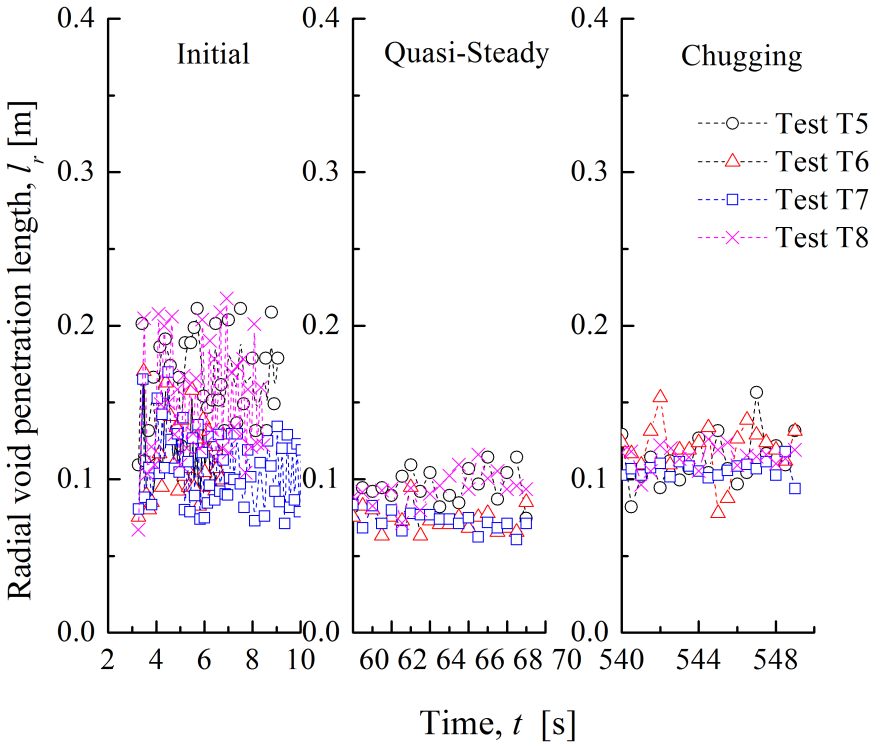

Figure 4-30 Radial Void Penetration as a Function of Time for Each Period of Transient Test Nos. T5, T6, T7, and T8

The maximum void penetration occurred during the initial period for all transient tests due to the inertia of the liquid slug ejected from the downcomer into the SP at the onset of the initial period. Higher break flow conditions, for example transient test Nos. T5 and T8, experienced the maximum void penetration both axially and radially as compared to the lower break flow test conditions.

The axial and radial void penetration during the quasi-steady period oscillated with time. In all transient tests, both the axial and radial penetration during the quasi-steady period were within close proximity to the downcomer and considerably less than the axial and radial penetration experienced during the initial period.

The chugging period, which occurred after the quasi-steady period for each transient test, demonstrated renewed deep axial and radial void penetration, more comparable to the penetration experienced in the initial period. While the renewed deep axial and radial void penetration experienced was more comparable to the initial period of each experiment (especially in the 0.102 m [4 in.] downcomer tests), the frequency of void ejection from the downcomer section was much more random than during the initial period and the quasi-steady period. The voids seen in the chugging period consisted of small, individual bubbles as opposed to the larger somewhat continuous plume experienced during the initial period and quasi-steady period.

While the void penetration during the initial period was greatest for each transient test, in an actual plant during a LOCA, ECCS pump start times are generally later than the duration of the initial period. For example, the initial period only lasts for approximately 9-15 seconds, but ECCS pump start times are typically around 20 seconds after the onset of a LOCA. Therefore, the initial, maximum void penetration may not be a concern at some plants with larger time differences between the onset of a LOCA and the start of their ECCS pumps. Due to the oscillating nature and relatively small void penetration experienced during the quasi-steady period, this period may not be safety significant. Renewed deep penetration was experienced during the chugging period, which began anywhere from 120 to more than 400 seconds into a transient test (the range of the onset of chugging depended on the initial test conditions). The chugging period would be experienced in the prototypic plant while the ECCS pumps are operating and therefore gas intrusion into the ECCS pump suction piping may be much more likely during the chugging period. However, the gas composition during the condensation oscillation/chugging period is primarily steam. Steam can condense before reaching a pump and therefore poses less of a problem for affecting pump operation than does noncondensable gas.

The focus of the current transient tests was the initial period of a LOCA blowdown. Thus the test conditions were well scaled for the initial period but not necessarily well scaled to simulate the chugging phenomena. Chugging is dependent on the gas volumetric flux, noncondensable gas concentration, and subcooling. It is necessary to parametrically study the chugging phenomena to better develop a model and investigate its importance to gas intrusion in ECCS suction piping.

4.2.4. Effect of Noncondensable Gas Concentration and Gas Volumetric Flux on SP Void Penetration and Distribution

The initial air concentration in the DW for six of the eight tests (three tests per downcomer size) was 100% while the initial air concentration of the other two tests (one test per downcomer size) was approximately 80%. Table 3-3 in Section 3.2.1 provides the detailed parameters for each test.

Each of the four transient tests performed for a particular downcomer size varied the gas volumetric flux at the downcomer by changing the break size initiating the test. The break steam mass flow rate, measured by flow nozzles in each appropriate break line for a particular transient test, was used as the inlet boundary condition in preparing a RELAP5 simulation. The gas volumetric flux at the downcomer exit for each test condition was then estimated using the RELAP5 simulation. This gas volumetric flux, estimated for each test condition, spans the entire range of the scaled-down gas volumetric flux expected in the downcomers during a LOCA in the prototypic plant. A comparison of the measured break flow rate and the estimated gas volumetric flux for each transient test is provided in Table 3-3 in Section 3.2.

Table 4-10 provides a description of each figure used to determine the effect of noncondensable gas concentration and gas volumetric flux on SP void penetration and distribution.

Table 4-10 List of Figures for Use in Determining of Effect of Noncondensable Gas Concentration and Volumetric Flux on SP Void Penetration and Distribution.

Figure	Transient Tests	Downcomer Section Size	Period	Figure Description	Measurement Device
4-31	T1 - T4	0.076 m (3 in.)	N/A[1]	Noncondensable gas concentration and the gas volumetric flux as a function of time	Downcomer oxygen analyzer[2]
4-32	T5 - T8	0.102m (4 in.)	N/A[1]	Noncondensable gas concentration and the gas volumetric flux as a function of time	Downcomer oxygen analyzer[2]
4-33	T1 - T4	0.076 m (3 in.)	Initial	Typical void fraction distribution	Conductivity probes
4-34	T1 - T4	0.076 m (3 in.)	Quasi-steady	Typical void fraction distribution	Conductivity probes
4-35	T1 - T4	0.076 m (3 in.)	Chugging	Typical void fraction distribution	Conductivity probes
4-36	T5 - T8	0.102 m (4 in.)	Initial	Typical void fraction distribution	Conductivity probes
4-37	T5 - T8	0.102 m [4 in.]	Quasi-steady	Typical void fraction distribution	Conductivity probes
4-38	T5 - T8	0.102 m [4 in.]	Chugging	Typical void fraction distribution	Conductivity probes

[1] The data provided in Figures 4-31 and 4-32 spans the duration of each transient test, therefore the figures include all three periods observed during a transient test and do not focus on a single period.

[2] The gas volumetric flux was estimated using RELAP5 based on the steam mass flow rate measured at the break locations. The upper plot in Figures 4-31 and 4-32 was produced using data measured by the downcomer oxygen analyzer. The lower plot in Figures 4-31 and 4-32 was produced using RELAP5.

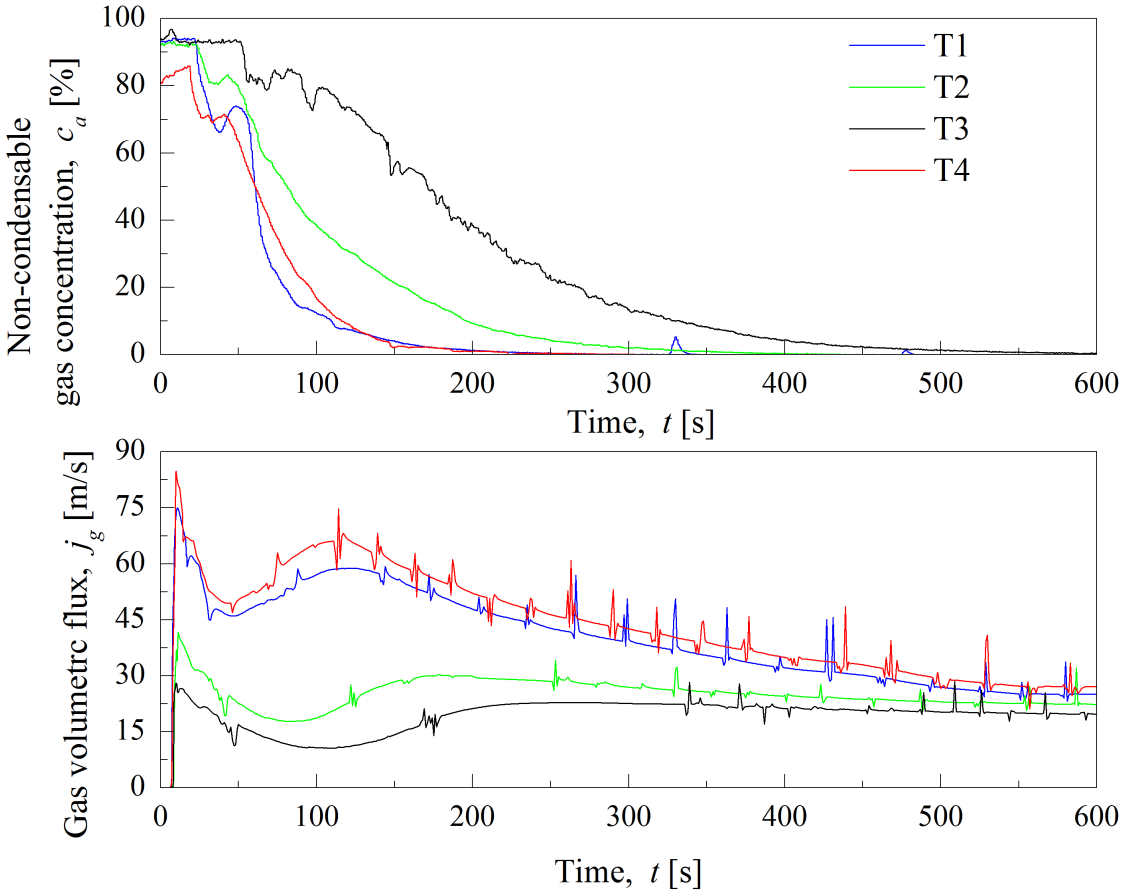

Figure 4-31 Noncondensable Gas Concentration and Gas Volumetric Flux as a Function of Time for Transient Test Nos. T1, T2, T3, and T4

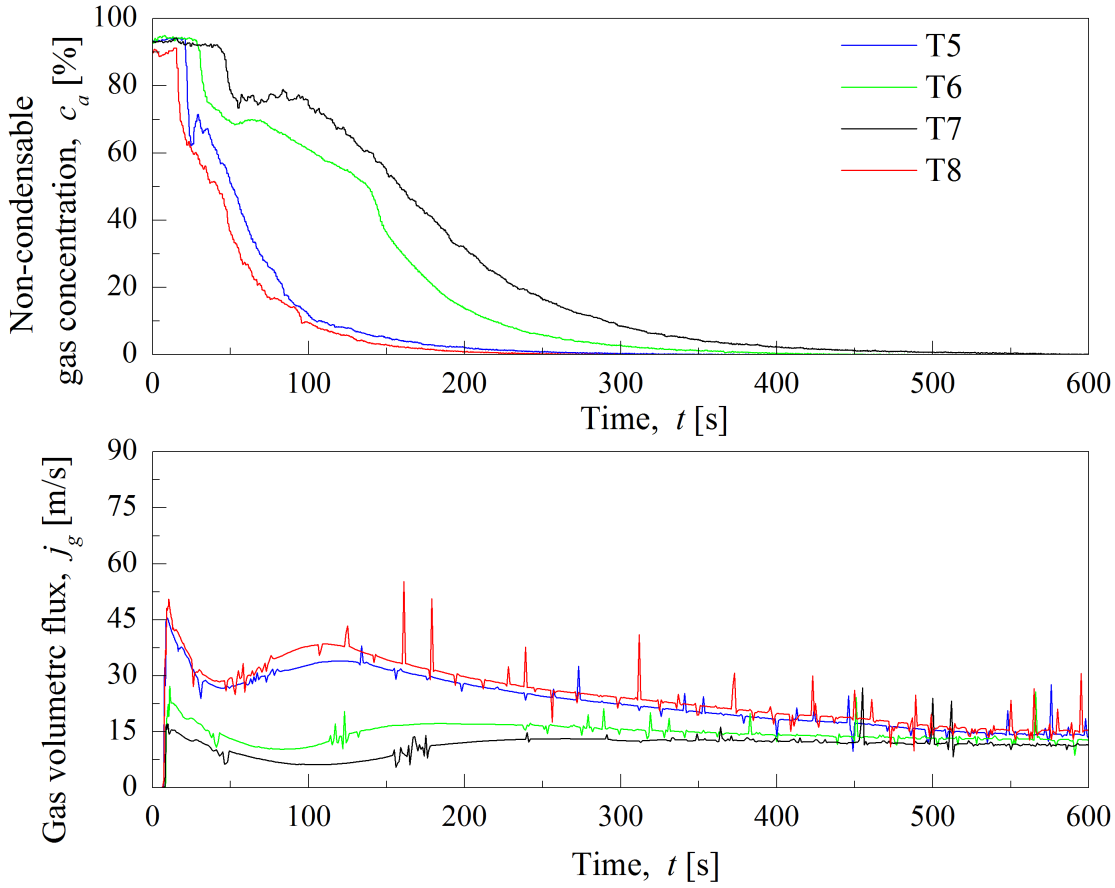

Figure 4-32 Noncondensable Gas Concentration and Gas Volumetric Flux as a Function of Time for Transient Test Nos. T5, T6, T7, and T8

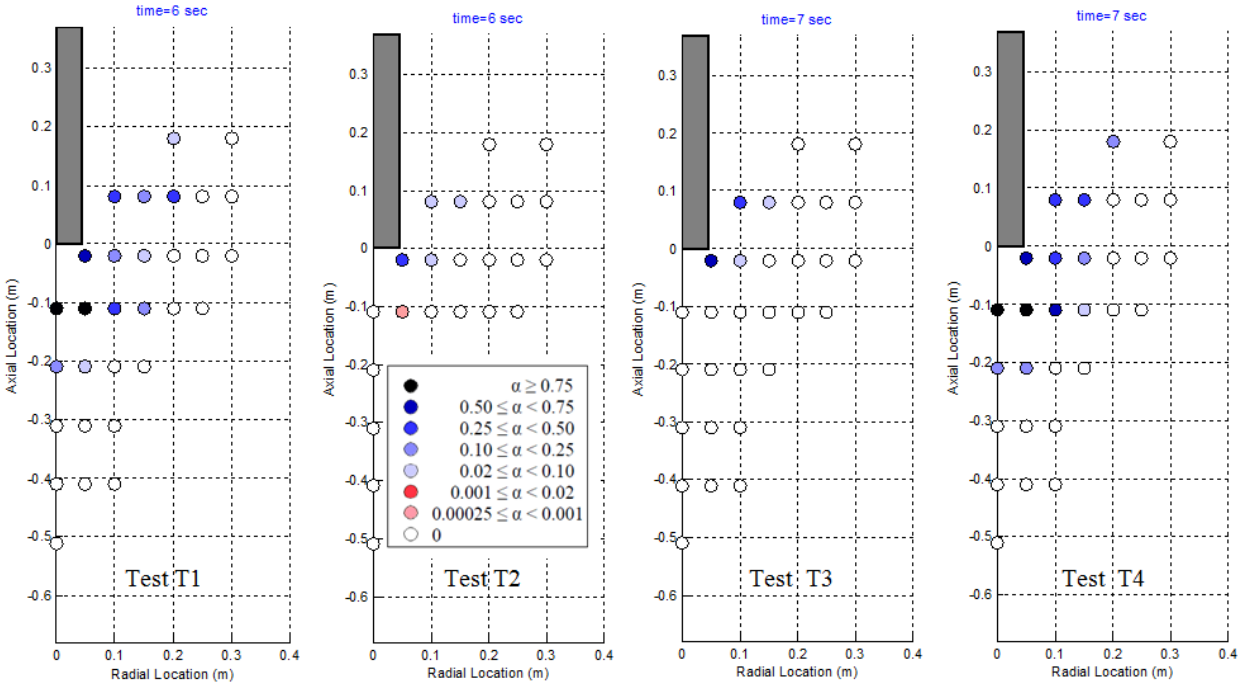

Figure 4-33 Typical Void Fraction Distribution around the Exit of Downcomer During the Initial Period for Test Nos. T1, T2, T3, and T4

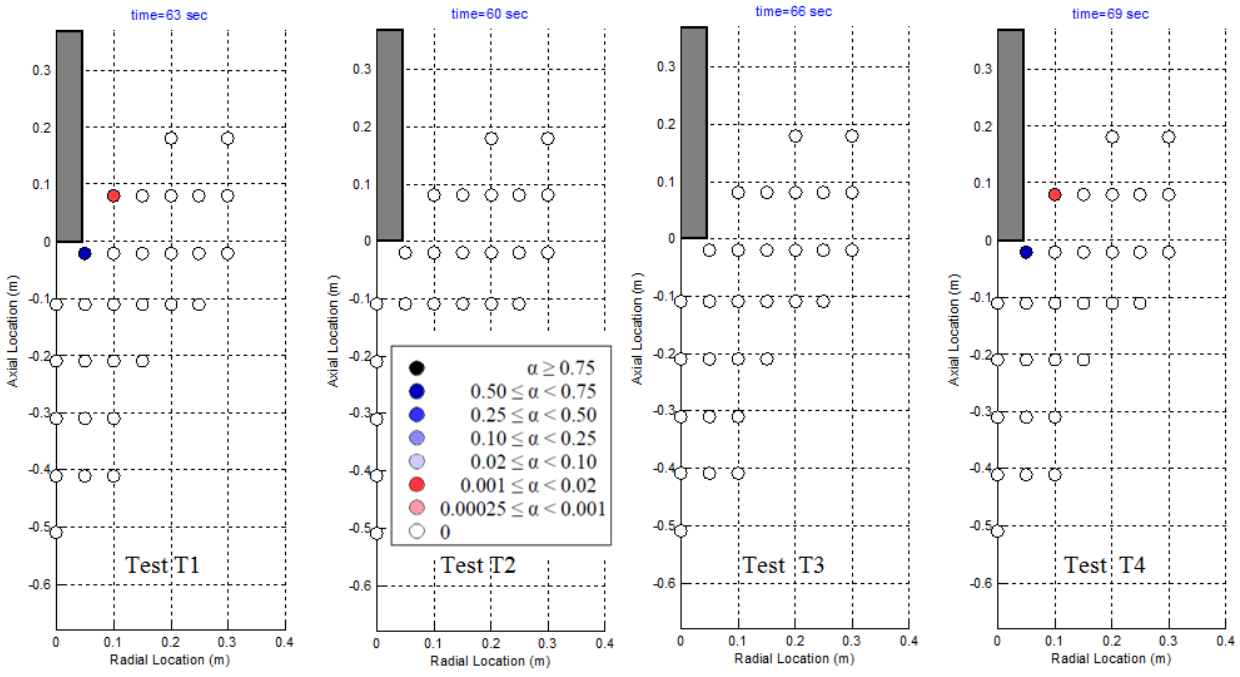

Figure 4-34 Typical Void Fraction Distribution around the Exit of Downcomer During the Quasi-steady Period for Test Nos. T1, T2, T3, and T4

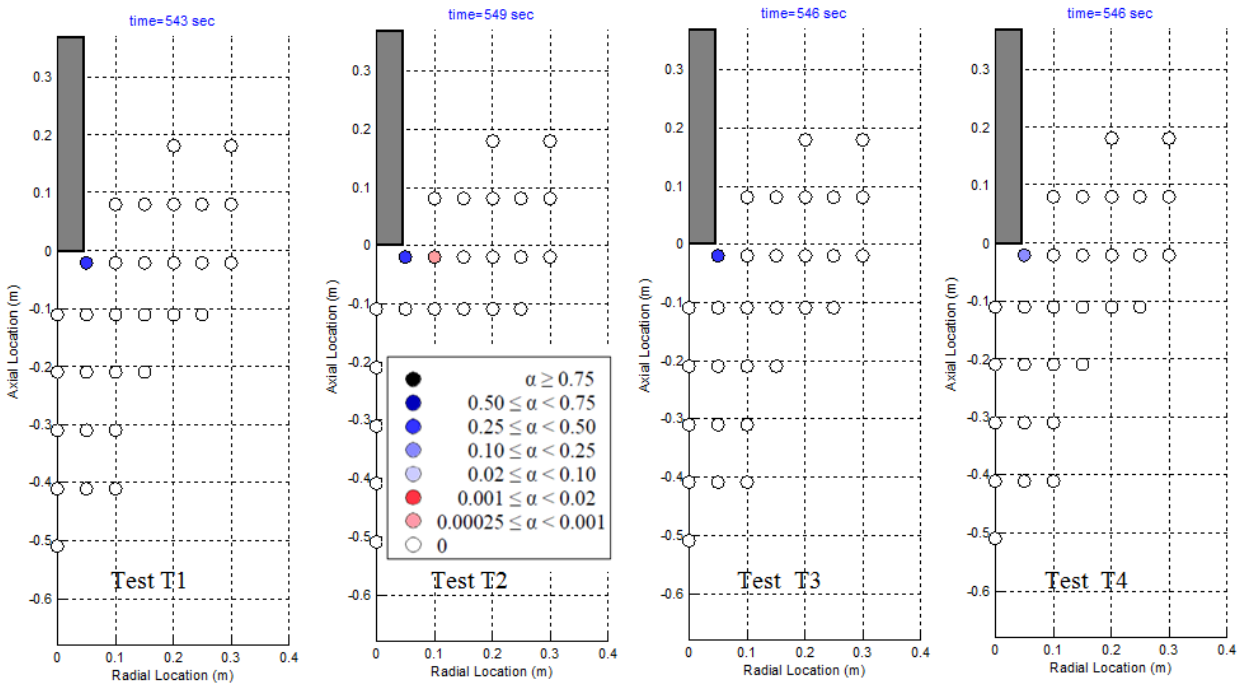

Figure 4-35 Typical Void Fraction Distribution around the Exit of Downcomer During the Chugging Period for Test Nos. T1, T2, T3, and T4

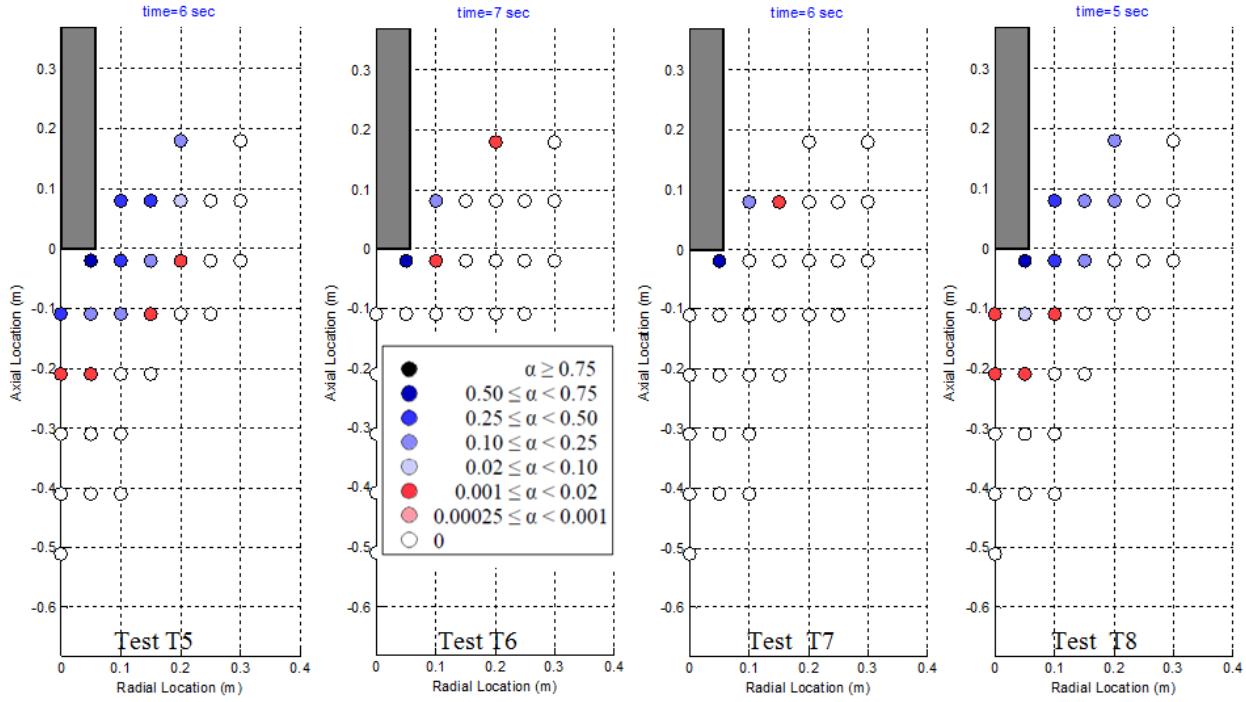

Figure 4-36 Typical Void Fraction Distribution around the Exit of Downcomer During the Initial Period for Test Nos. T5, T6, T7, and T8

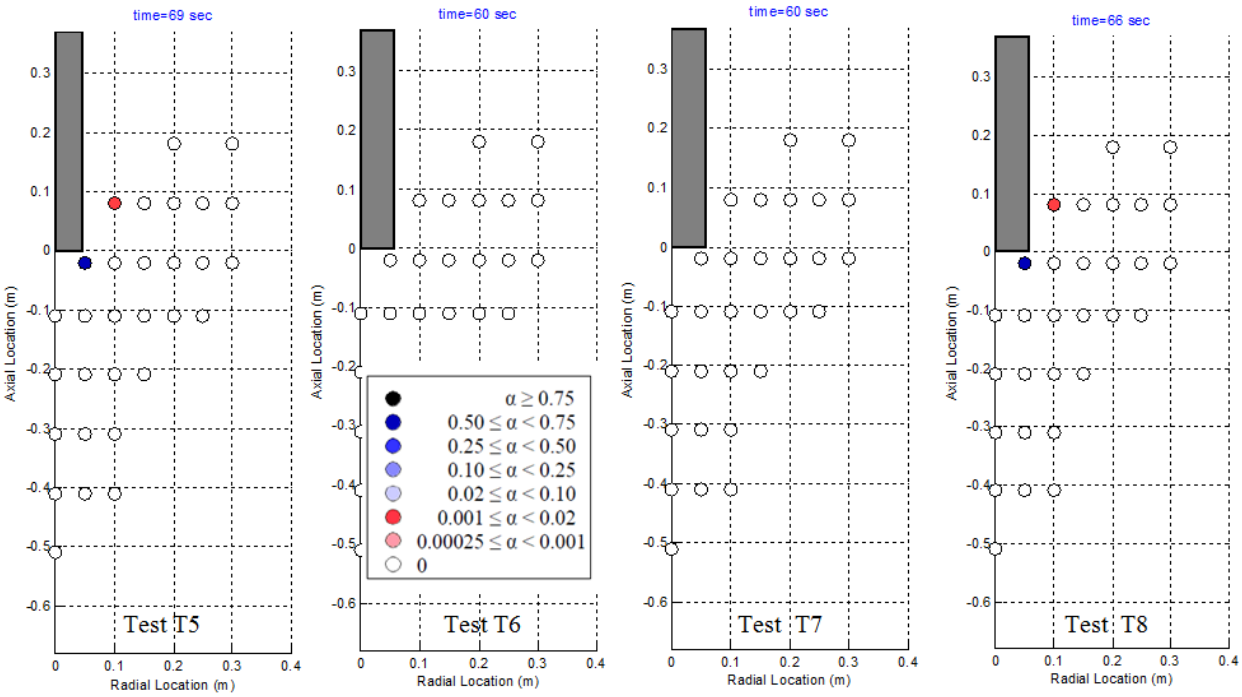

Figure 4-37 Typical Void Fraction Distribution around the Exit of Downcomer During the Quasi-steady Period for Test Nos. T5, T6, T7, and T8

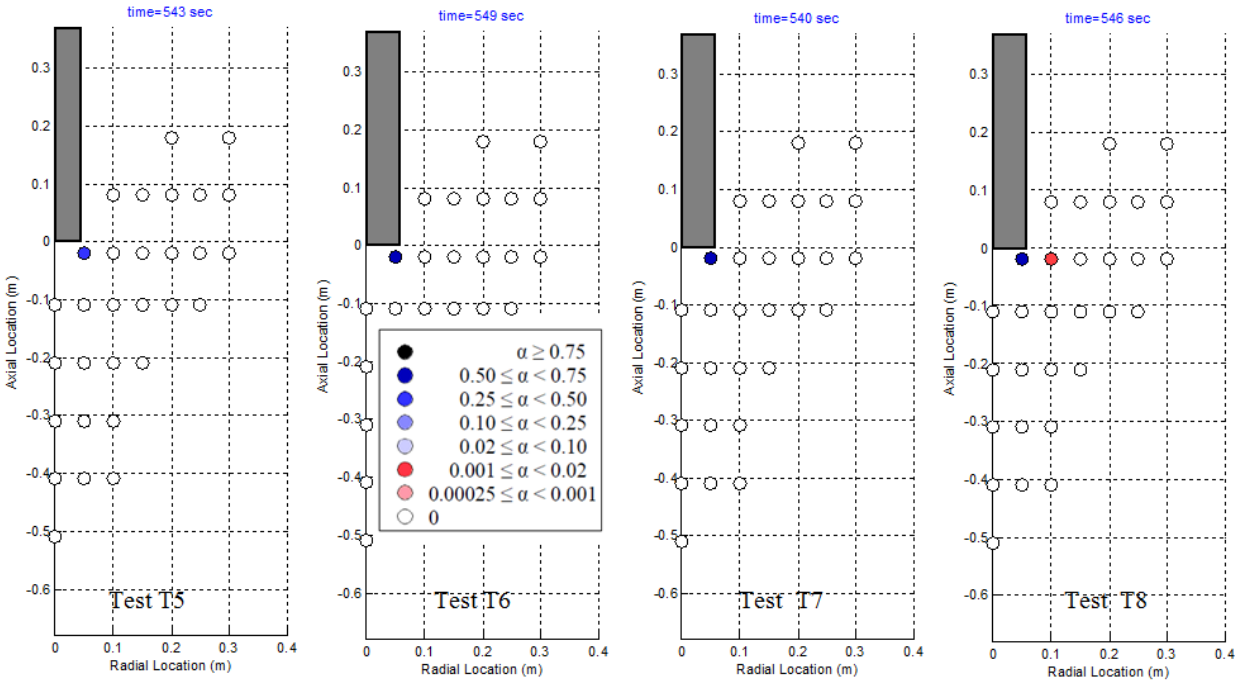

Figure 4-38 Typical Void Fraction Distribution around the Exit of Downcomer During the Chugging Period for Test Nos. T5, T6, T7, and T8

Comparisons of Figures 4-31, 4-33, 4-34, and 4-35 and comparisons of Figures 4-32, 4-36, 4-37, and 4-38 were used to determine that the void distribution and region of void penetration in the SP is governed by the gas volumetric flux at the downcomer and by the noncondensable gas concentration in the downcomer, with the former observed to have the greater effect. The higher the initial gas volumetric flux, the deeper the axial void penetration during the initial period. The bubble plume size during the quasi-steady period also increased a small amount with higher gas volumetric flux. The chugging period void penetration depth appeared to be more sensitive to the noncondensable gas concentration than to initial gas volumetric flux. However, the onset of chugging was much earlier when the break size and hence initial gas volumetric flux was higher due to more rapid decrease in the noncondensable gas concentration.

4.2.5. Comparison of the 0.076 m and 0.102 m (3 in. and 4 in.) Diameter Downcomer Tests

Figures 4-39 and 4-40 provide a comparison of the 100% initial DW air concentration tests for both the 0.076 m and 0.102 m (3 in. and 4 in.) downcomer test sections. The data in these figures, axially (Figure 4-39) and radially (Figure 4-40), is averaged to provide a good overall comparison over the entire initial period of the test. As seen in the figures, both the axial and radial penetration depths of the bubble plumes increased with increased initial gas volumetric flux. The downcomer cross-sectional area did not significantly impact the averaged initial void penetration (both axial and radial) for tests having comparable initial gas volumetric flux.

However, these results may not be extrapolated directly to the prototypic plant without performing a more thorough study.

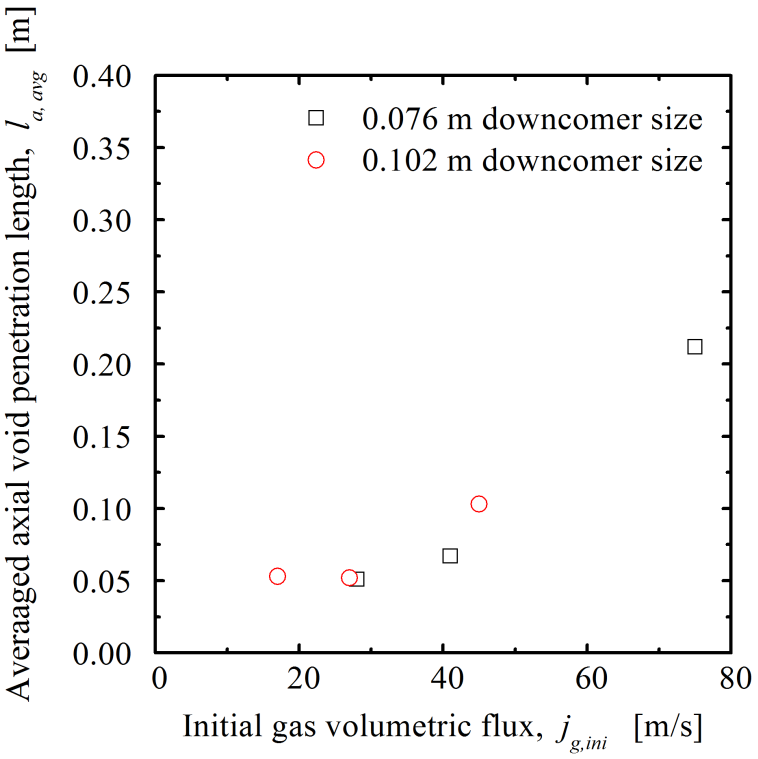

Figure 4-39 Averaged Initial Axial Void Penetration and Initial Gas Velocity

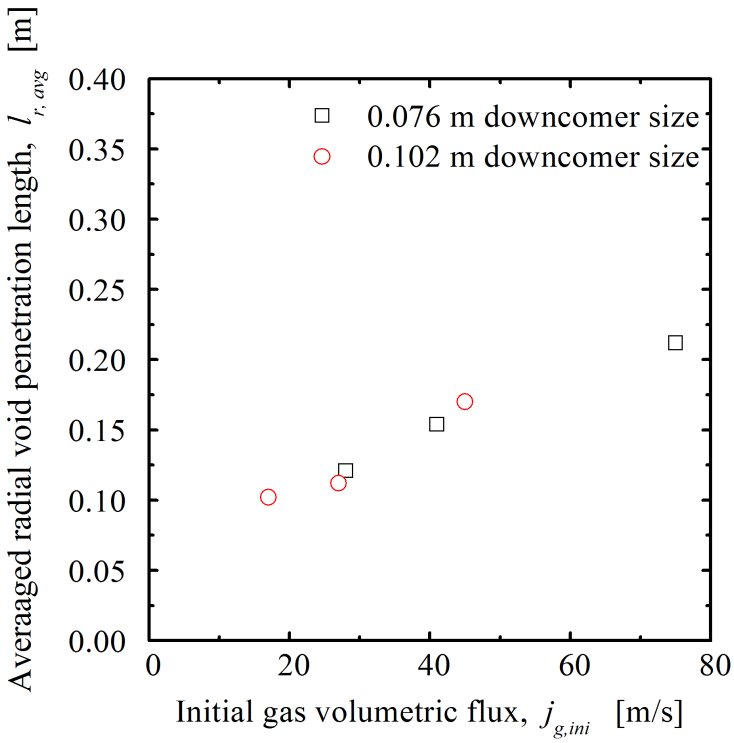

Figure 4-40 Averaged Initial Radial Void Penetration and Initial Gas Velocity

Figures 4-41 and 4-42 provide a comparison of the 100% initial DW air concentration tests for both the 0.076 m and 0.102 m (3 in. and 4 in.) downcomer test sections. The data in these figures was taken from the maximum penetration point, axially (Figure 4-41) and radially (Figure 4-42), for each test to provide a single point comparison. Similar to the averaged penetration figures, both the maximum axial and radial penetration of the bubble plumes tended to increase with increased initial gas volumetric flux. For both downcomer sizes, the downcomer cross-sectional area did not significantly impact the maximum initial void penetration (both axial and radial) for tests having comparable initial gas volumetric flux.

However, as with the averaged results, these results may not be extrapolated directly to the prototypic plant without performing a more thorough study.

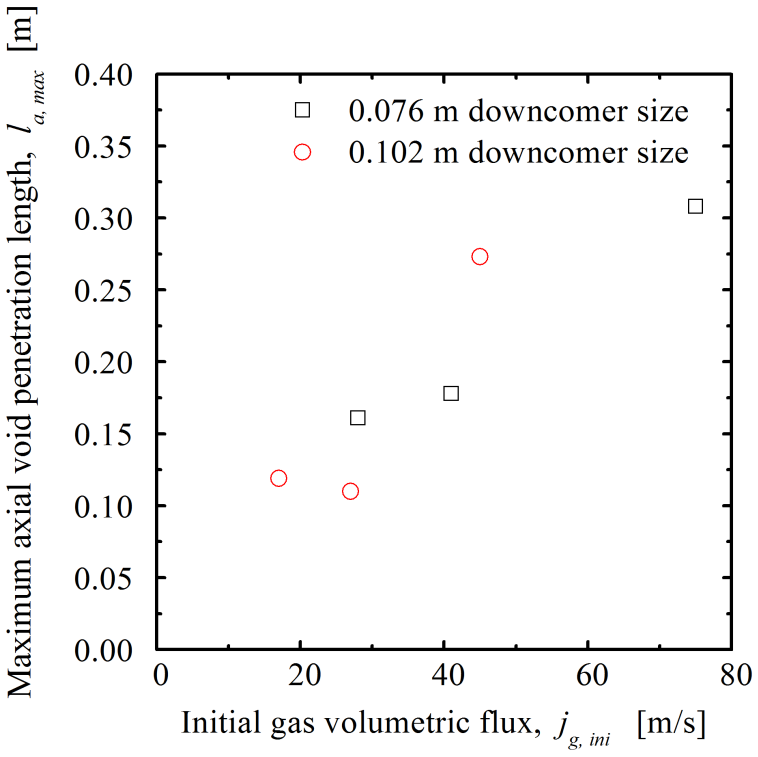

Figure 4-41 Maximum Axial Void Penetration and Initial Gas Velocity

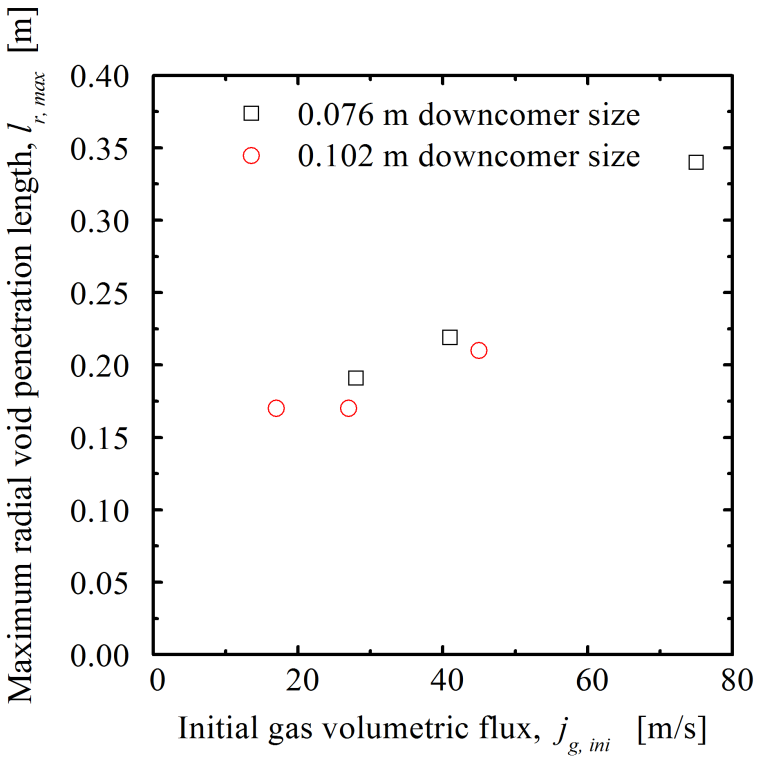

Figure 4-42 Maximum Radial Void Penetration and Initial Gas Velocity

4.2.6. Averaged Axial Bubble Velocity and Chord Length

Table 4-11 shows the averaged axial bubble velocity and chord length measured by the double-sensor conductivity probes for each transient test condition. It is noted that only some gas bubbles were detected and measured by the conductivity probes. For general results, it can be seen that averaged bubble upward velocities ranged between 0.94 to 1.77 m/s (3.1 to 5.81 ft/s). Downward velocity was measured as 1.99 and 3.78 m/s (6.53 and 12.4 ft/s). The averaged gas bubble upward velocity was measured to be greater for the test conditions with the higher break flow. The averaged gas bubble chord length ranged between 0.046 to 0.137 m (1.8 in. to 5.39 in.). The averaged downward bubble velocity could not be estimated in some test conditions (indicated by "-" in Table 4-11) since the bubble plume size was limited. The gas bubbles in those conditions did not contact the probes located below C level used for measuring the downward bubble velocity as explained in Section A.1.2.1.

Table 4-11 Averaged Axial Bubble Velocity and Chord Length Measured By the Double-sensor Conductivity Probes for the Transient Tests.

Test No.	Averaged Upward Bubble Velocity (m/s [ft/s])	Averaged Downward Bubble Velocity (m/s [ft/s])	Averaged Bubble Chord Length (m [in])
T1	1.47 [4.82]	3.78 [12.40]	0.109 [4.29]
T2	1.24 [4.07]	-	0.137 [5.39]
T3	1.35 [4.43]	-	0.137 [5.39]
T4	1.77 [5.81]	1.99 [6.53]	0.121 [4.76]
T5	1.53 [5.02]	-	0.088 [3.46]
T6	0.94 [3.08]	-	0.046 [1.81]
T7	0.89 [2.92]	-	0.082 [3.23]
T8	1.16 [3.81]	-	0.107 [4.21]

SUMMARY

The Emergency Core Cooling System (ECCS) in a BWR is critical for keeping the reactor core covered during blowdown from a LOCA and for removing decay heat during recovery. The SP in the BWR Mark I containment is a primary source of supply water for the ECCS pumps' suction. The possible failure of the low pressure ECCS due to large amounts of entrained gas in the ECCS pump suction piping of a BWR from the SP has been considered. A certain amount of air ingestion into the Residual Heat Removal (RHR) and core spray pumps can degrade the pump performance and thereby compromise coolant delivery to the core. Therefore, it is important to understand the void distribution in the SP during blowdown from a LOCA.

Two sets of experiments, steady state tests and transient tests, were performed at the PUMA-E test facility to study the void fraction distribution in the SP. In the steady state tests, different air volumetric flow rates were injected into the downcomer installed in the PUMA-E SP. For the transient tests, the actual blowdown characteristics of a LOCA period in the DW and subsequent injection of sequential flows of air, steam-air mixture, and pure steam with the various flow rate conditions was simulated using the PUMA-E RPV, DW, and SP. The downcomer geometry and inlet flow conditions were determined from the results of a scaling analysis. (The scaling analysis for these parameters is based on proprietary design information and will not be included here.)

Although the experimental facility is not prototypic in scale, it provides valuable information about the qualitative behavior of the downcomer and suppression pool of a BWR Mark I and Mark II under blowdown conditions. The information gathered in this analysis provides a strong starting point for further research and will help guide future investigations. It may also be possible, with a rigorous and thorough analysis, to extrapolate all of the experimental result to prototypic conditions. In addition, the data collected will serve to guide and benchmark future CFD analyses.

To perform the steady state tests, the PUMA-E facility was modified as follows:

- A 0.102 m (4 in.) downcomer test section was installed in the SP by connecting the test section to the existing SRV line.
- An air supply line was added to provide the required air volumetric flow rate to the downcomer test section.

To perform the transient tests, the PUMA-E facility was modified as follows:

- 0.076 m and 0.102 m (3 in. and 4 in.) downcomer test sections were installed in the SP by connecting the test sections with a window in the existing vertical vent pipe.
- Jet deflectors were installed in the DW at each DPV line discharge location and at the entrance of the vertical vent pipe to prevent the discharge of steam from the RPV directly to the SP.

For both tests, common instrumentation and the high-speed camera were installed as follows:

- Vortex flow meters, flow nozzles, pressure gauges, and thermocouples were installed in the test facility to obtain required information such as air flow rate, steam break flow, pressure, temperature, etc.

- Single-sensor and double-sensor conductivity probes used to measure the void fraction, bubble velocity, and bubble chord length around the downcomer exit were set in a supporting cage inside the SP.
- A high-speed camera was installed at a viewing port in the SP to record flow visualization information during the experiment.

Steady State Tests

Sixteen steady state tests were performed by varying the downcomer void condition, air volumetric flow rate, and air velocity ramp rate. Each steady state test was conducted for 30 seconds.

The time-averaged void fractions, axial bubble velocities, and bubble chord length were estimated from the data obtained using the conductivity probes. Information about the void fraction distribution, bubble velocity, and bubble chord length around the downcomer exit at the various times during the experiment was obtained. The void distribution and penetration was estimated based on the signals obtained by the conductivity probes and recorded images from the high-speed camera. The images obtained by the high-speed camera demonstrated the development of the bubble plume during the experiment.

Two distinct periods (initial period and quasi-steady) were observed during each steady state test. The axial void penetration depth was maximum during the initial period due to the liquid slug inertia and was reduced in the quasi-steady period. The radial void penetration oscillated from the initial period through the quasi-steady period.

To study the impact of volumetric flow rate, air velocity ramp rate, and initial downcomer void condition on SP void distribution and penetration, a parametric study was performed and a comparison of the experimental results of selected test conditions was made.

The following conclusions were reached from the steady state test results:

- Air volumetric flow rate has a minor effect on the void fraction distribution and void penetration during the initial period in the range of high air volumetric flow rate conditions.
- Air volumetric flow rate strongly impacts the void fraction distribution and void penetration during the quasi-steady state for the entire range of air flow rate conditions.
- Initial downcomer void conditions strongly affect the void fraction distribution and void penetration during the initial period but have no impact on void fraction distribution and void penetration during the quasi-steady period.
- Air injection velocity ramp rate has only a minor impact on the void fraction distribution and void penetration in both the initial period and the quasi-steady period.

Transient Tests

Eight transient tests were performed. The transient tests varied the downcomer size (0.076 m or 0.102 m [3 in. or 4 in.]), gas volumetric flux at the downcomer, and the initial air concentration in the DW. Each transient test was conducted for 10 minutes.

In the transient tests, saturated steam with the required break flow rate was discharged from the RPV to the DW. The steam then passed through the installed downcomer section into the SP.

Measured break mass flow rate of steam was used as the inlet boundary condition in preparing a RELAP5 simulation. The gas volumetric flux at the downcomer for each test conditions was then estimated using RELAP5. The gas volumetric flux estimated for each test condition spans the entire range of the scaled down initial gas volumetric flux expected during a LOCA in downcomers of the prototypic plant. The test data for each test condition was obtained using the same method used to obtain the steady state test results.

Three periods of blowdown (initial period, quasi-steady period, and chugging period) were observed during each transient test. The initial period was dominated by the ejection of the liquid slug from the downcomer and provided the maximum axial void penetration depth. The quasi-steady period consisted of oscillations resulting from condensation and pressure oscillations at the exit of the downcomer. The axial and radial void penetration was significantly reduced in the quasi-steady period compared with the initial period. The eventual reduction in noncondensable gas concentration in the DW to some threshold caused the chugging period. During the chugging period, random small bubbles were ejected from the downcomer exit. The penetration of these bubbles was greater than the penetration experienced during the quasi-steady period and more comparable to the initial period penetration.

The transient tests were performed with 0.076 m and 0.102 m (3 in. and 4 in.) downcomer diameters to investigate the impact of downcomer cross-sectional area on the void penetration. For the experiments performed, it was found that the downcomer cross-sectional area did not significantly impact the void penetration for tests having comparable initial gas volumetric flux. However, the downcomer diameter in the prototypic plant is much larger compared with the downcomer diameters used in the transient tests. In order to confirm the insignificance of the downcomer size on the void fraction, further analysis is required. The additional analysis may include full-scale experiments with prototypic geometry and detailed CFD analyses.

The following conclusions were reached from the transient test results:

- Axial depth and radial void penetration are maximum during the initial period and reduced in the quasi-steady period.
- The void distribution and void penetration in the SP is governed by the gas volumetric flux at the downcomer and by the air concentration in the downcomer.
- The chugging period demonstrated renewed deep axial and radial void penetration which is more comparable to the penetration experienced in the initial period. However, the injected bubbles are small compared with the bubble plume experienced in the initial and quasi-steady period and are primarily composed of steam which would be expected to have a smaller effect on pump performance than noncondensable gas.
- The onset of chugging was observed to be earlier when the initial gas volumetric flux was higher and when the initial noncondensable gas concentration in the DW was lower for test conditions with comparable initial gas volumetric flux.
- The averaged axial and radial penetration depths of the bubble plumes during the initial period increase with increased initial gas volumetric flux regardless of downcomer

diameter for the test sections used. However, this result may not be extrapolated directly to the prototypic plant without performing a more thorough study which could include further tests.

It is noted that results of the transient experiments were more benign in terms of initial axial void penetration as compared to the steady state test results. In other words, the maximum penetration depth of air experienced in the steady state tests was larger than that experienced when performing the transient tests. This is because the DW was not used in the steady state tests, resulting in the air fully pressurizing the downcomer immediately. Therefore, the initial liquid slug in the downcomer for the steady state tests was ejected into the SP at a significantly higher velocity compared to the velocity of ejection in the transient tests. The higher ejection velocity of the liquid slug results in deeper axial void penetration.

The focus of the current transient tests was the initial period of a LOCA blowdown. The test conditions were well scaled for the initial period but not necessarily well scaled to simulate the chugging phenomena. Chugging is a complex phenomenon that depends primarily on periodic sudden condensation of steam into colder water, but depends also on gas volumetric flux, noncondensable gas concentration, frequency of the phenomenon, heat transfer, and subcooling, as well as the downcomer and suppression pool geometry. The rudimentary scaling methods used here are not suitable for use with such complex phenomenon. Instead, more specific and advanced scaling techniques would be needed. However, the chugging phase results in considerable void penetration.

The current results may not be extrapolated directly to the prototypic plant condition without performing a more thorough study and possibly gathering more experimental data.

APPENDIX A. INSTRUMENTATION

A.1 Instrumentation Description

A.1.1 Introduction

In the experimental facility, several major instruments are installed inside the DW, ADS, and MSL to obtain the pressure, temperature, and inlet boundary conditions such as steam flow rate.

The single-sensor and double-sensor conductivity probes are installed in the instrument supporting cage to measure the void fraction, bubble velocity, and chord length. The pressure gauges and thermocouples are installed to measure the pressure and temperature of the gas and water space in the SP.

The test instrumentation is identified by tag numbers, which consist of three fields: XX-YYY-NN.

- XX: instrumentation type (LT: differential pressure gauge, PT: absolute pressure gauge, TE: Thermocouple, FT: Nozzle, CE: conductivity probe)
- YYY: instrumentation location (SP: suppression pool, DC: downcomer, DW: Drywell, DP: depressurization line, MS: main steam line)
- NN: instrumentation number

Appendix Section A.4 lists the instrumentation, units, and measurable ranges.

A.1.2 Conductivity Probes

There are two types of conductivity probes used in this experiment. One is the single-sensor conductivity probe and the other is the double-sensor conductivity probe. The single-sensor conductivity probe is used to measure the local void fraction while the double-sensor conductivity probe is used to simultaneously measure the local void fraction and bubble velocity.

A.1.2.1 Conductivity Probes and Supporting Cage Design

As shown in Figure A-1, the single-sensor conductivity probe consists of an electrode, which is made from Teflon coated stainless steel wire with 0.61 mm (0.024 in.) diameter. The Teflon coating on the tip of the wire is removed to expose a sharp edge with the length of 1.27 mm (0.05 in.). To protect against any scratches to the Teflon coating on the wire that can produce a disturbance of the signal, a heat shrink tube is applied to cover that section of stainless steel wire. The probes are installed on a stainless steel tube of 12.7 mm (0.5 in.) diameter through conax fittings.

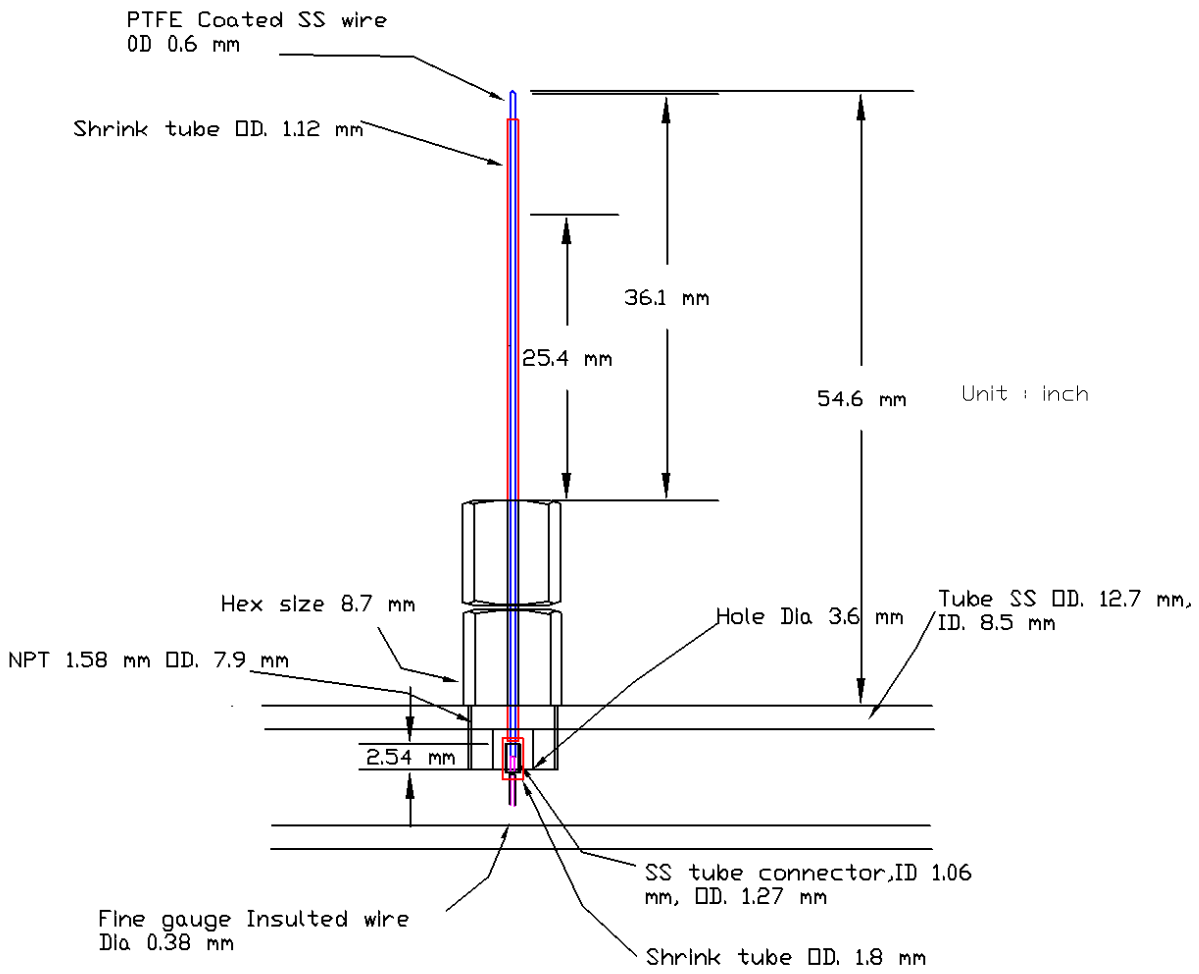

Figure A-1 Design of Single-sensor Conductivity Probe

The design of the double-sensor conductivity probe is similar to the single-sensor conductivity probe. The main difference between the single- and double-sensor conductivity probe design is the number of stainless steel wires in the probe. As shown in Figure A-2, the double-sensor conductivity probe consists of two electrodes, which have the same diameter as those of the single-sensor conductivity probe. To measure the bubble velocity, the two electrodes are arranged with approximately 3.8 mm (0.15 in.) of elevation difference.

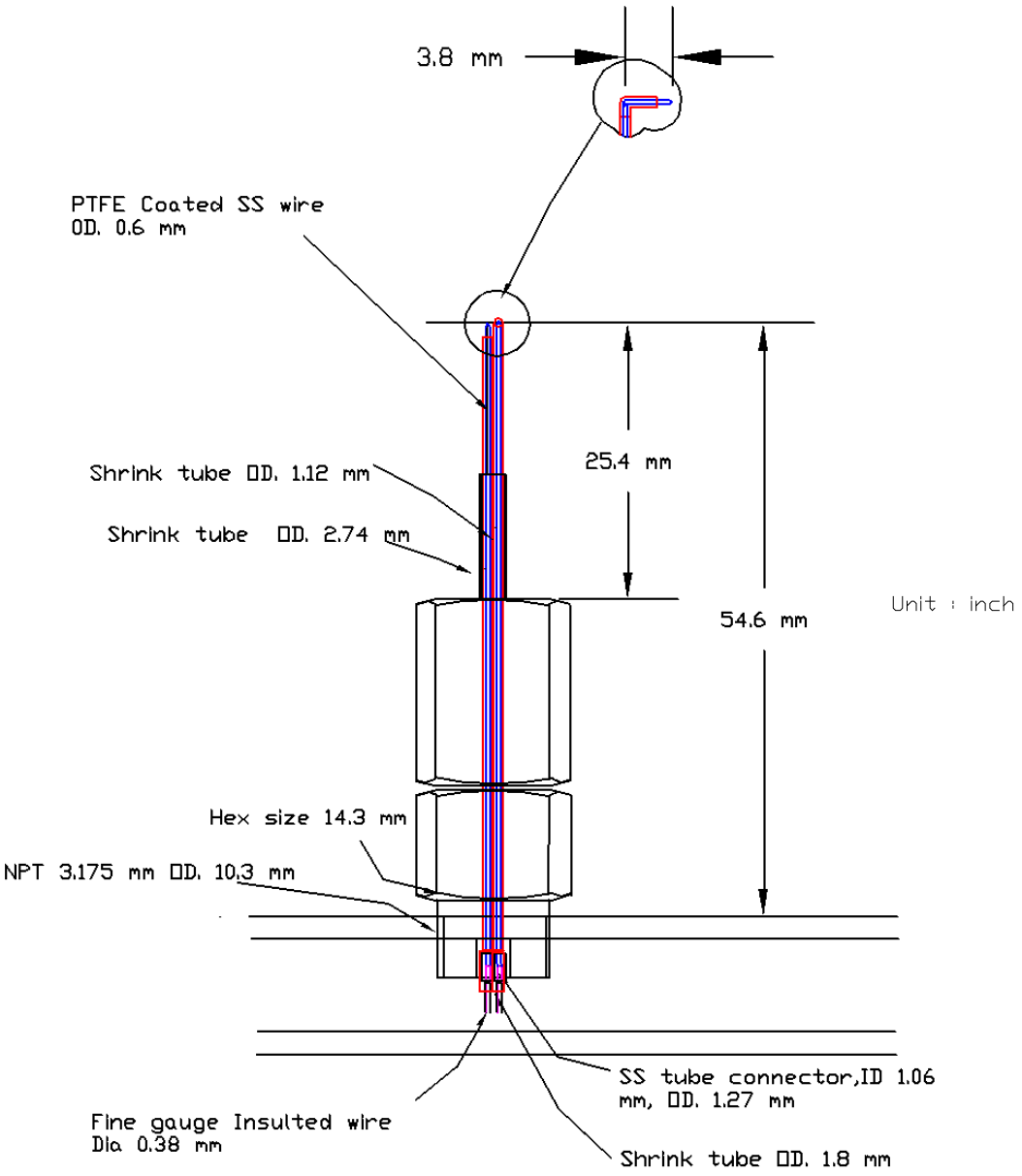

Figure A-2 Design of Double-sensor Conductivity Probe

Each stainless steel wire of the probe is connected with fine gauge insulated wire to carry the electric signals to an electronic circuit and Data Acquisition System (DAS). Finally, the electric signals are converted into the void fraction and bubble velocity information (Ref.6).

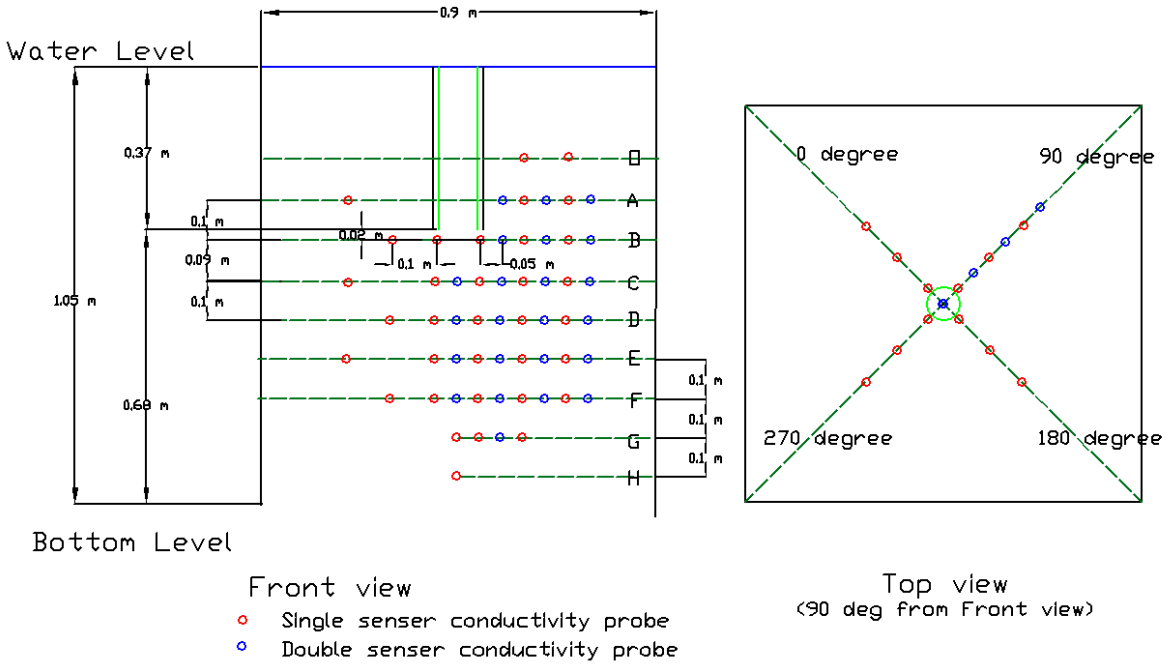

Figure A-3 Configuration and Orientation of Single-sensor and Double-sensor Conductivity Probes on Supporting Cage

The arrangement of the measurement locations for conductivity probes on the supporting cage is displayed in Figure A-3. Forty-nine single-sensor and 22 double-sensor conductivity probes are mounted systematically on the supporting cage, which is a rectangular prism of size 0.9 m × 0.9 m × 1.2 m (3 ft x 3 ft x 4 ft). The configuration of the probe locations has eight axial levels (Level O to H) and seven radial positions from the center of the downcomer pipe in a cross-shaped pattern. The nine axial levels of probes were adjusted according to the bubble plume size which was observed from the shake down tests. Due to the limited performance of the Data Acquisition System (DAS) electronics board, conductivity probes located far from the region of interest are disconnected from the DAS system in order to increase data acquisition frequency. It was confirmed that these disconnected conductivity probes are located outside the maximum void penetration over the whole range of test conditions.

In each level of probes, several single-sensor and double-sensor conductivity probes are mounted on one of the four tubes to measure detailed void fraction and bubble velocity, while at least three single-sensor conductivity probes are mounted on the other tubes to check the symmetry of the void fraction at the same level of the bubble plume. The tip of each single-sensor probe is oriented horizontally to detect upward and downward moving bubbles. The short tip of each double-sensor conductivity probe is oriented horizontally, and the long tip of each double-sensor conductivity probe is directed upward for the probes in level C to level G to measure downward bubble velocity. The long probe tips in level A and B are directed downward to measure upward bubble velocity. These orientations are designed based on the direction of the gas plume movement. The supporting cage is fixed within the existing structures in the SP to prevent shaking or vibration that may affect experimental results. Five single-sensor conductivity probes are installed on the side wall of the downcomer at various axial positions to

estimate the initial water column level before performing the tests. The first probe is located near the exit of the downcomer while the fifth probe is mounted at a distance of 0.37 m (1.2 ft). from the downcomer exit. The details of the probe arrangement are described in Section A.5.

A.1.2.2 Data Processing for Conductivity Probes

The raw output signal obtained by a conductivity probe is the voltage signal from the electronic circuit and ranges from about 1 to 5 volts. The low and high voltage signal represent the water phase and gas phase respectively at the location of the probe tip at a given time. To convert this information to the time-averaged void fraction, a computer program is written to process the data.

For an example, the raw voltage signals of each probe with a frequency of 4667 Hz are categorized to be 0 or 1 by comparison with the threshold value. If the value is more than the threshold value, it will be converted to 1. If the value is less than the threshold value, it will be transformed to 0.

The time-averaged void fraction is estimated over the proper averaging time by

$$Time\ averaged\ void\ \ fraction = \frac{Number\ \ of\ \ data\ \ of\ \ gas\ \ phase}{Number\ \ of\ \ total\ \ data} \tag{A.1}$$

Sensitivity tests for an time over which to obtain the time-averaged void fraction were performed. The time-averaged void fractions were obtained with averaging times of 0.25, 0.5, 1.0, 2.0, and 4.0 seconds. The sensitivity results are shown in Figures A-4 to A-8.

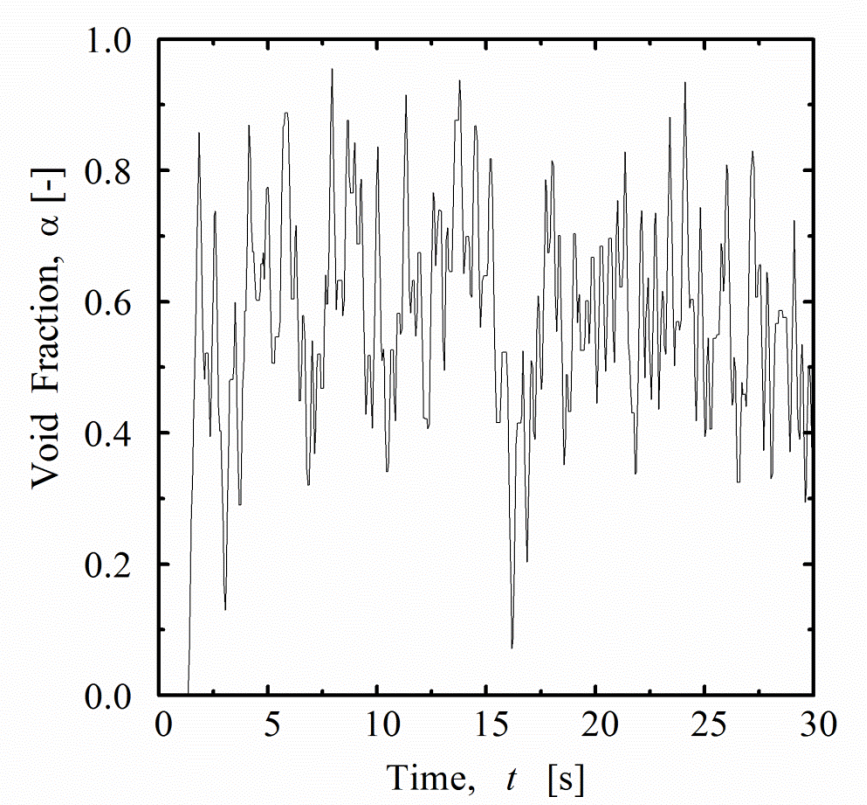

Figure A-4 Void Fraction Calculated Based on the Averaging Time of 0.25 Second

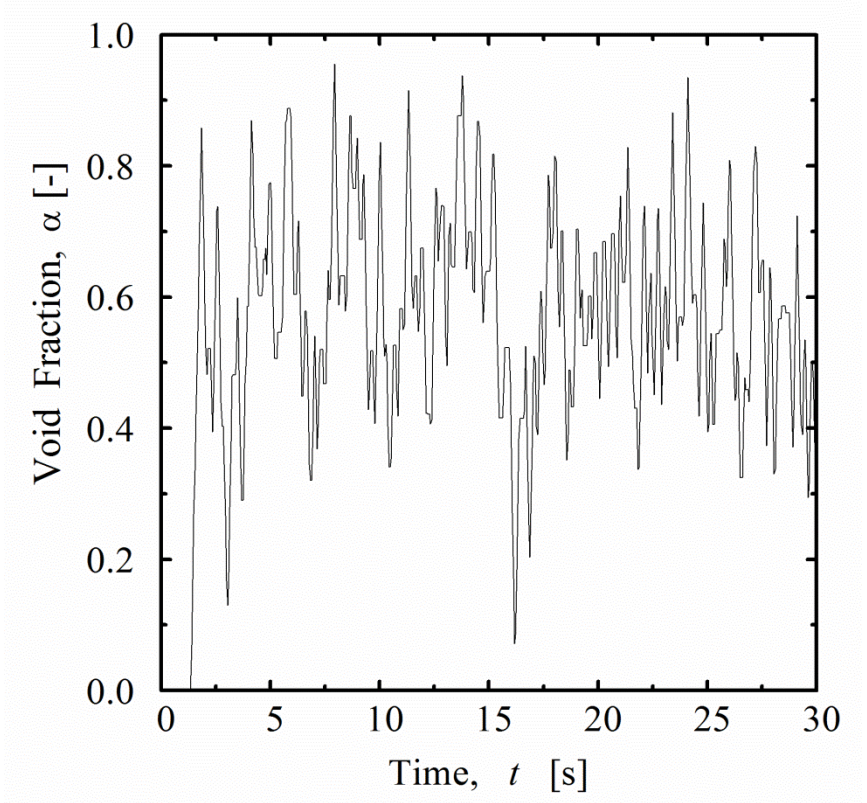

Figure A-5 Void Fraction Calculated Based on the Averaging Time of 0.5 Second

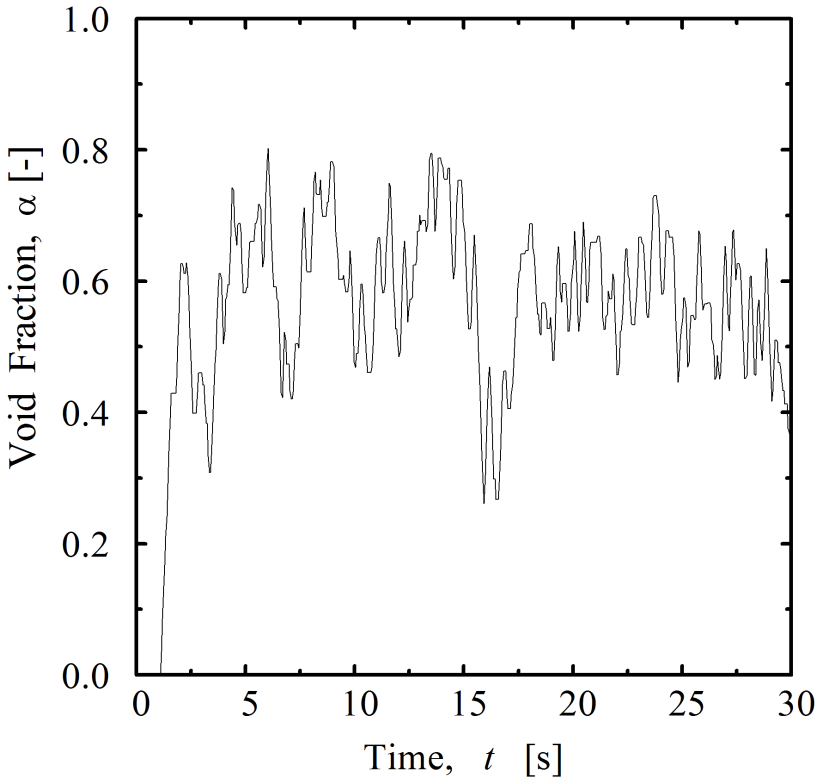

Figure A-6 Void Fraction Calculated Based on the Averaging Time of 1.0 Second

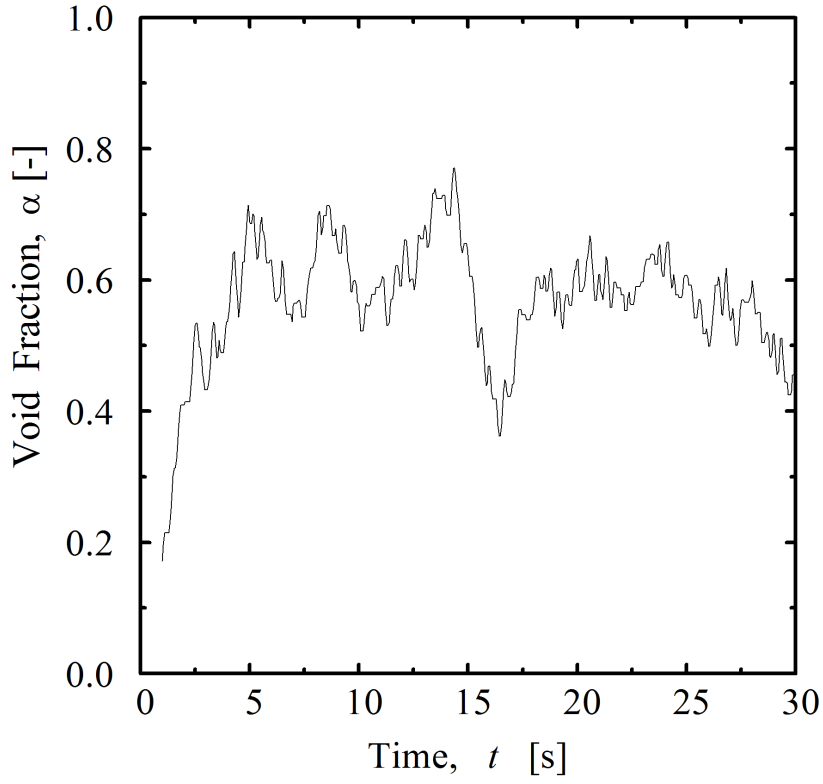

Figure A-7 Void Fraction Calculated Based on the Averaging Time of 2.0 Seconds

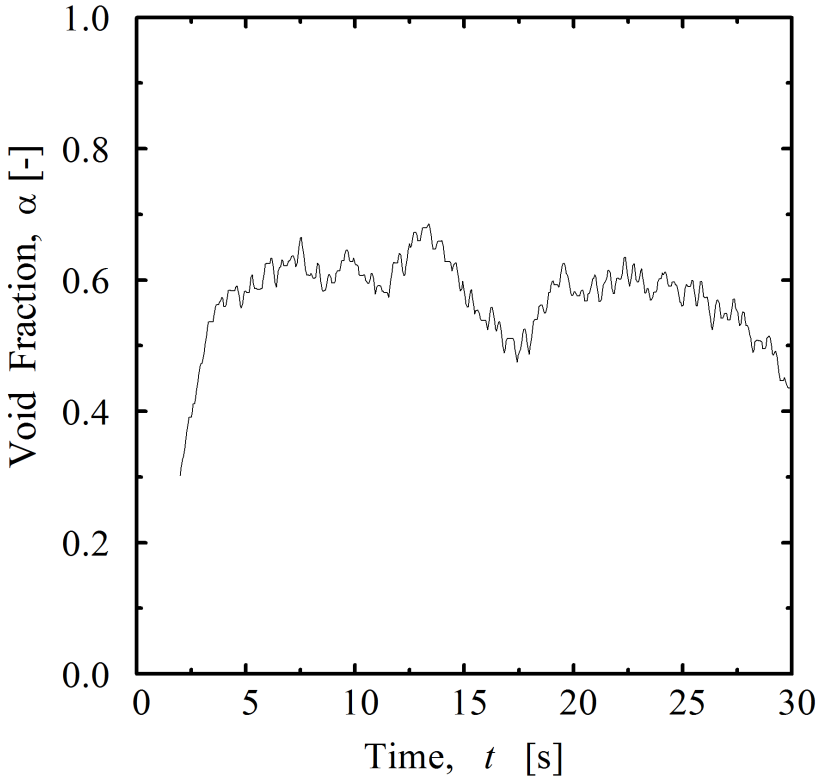

Figure A-8 Void Fraction Calculated Based on the Averaging Time of 4.0 Seconds

From the results of the sensitivity tests shown in Figures A-4 to A-8, the calculated void fractions fluctuate around the averaged value depending on the given averaging time.

For the averaging time of 0.25 second, very high frequency void fraction change is observed, whereas for the averaging time of 4.0 seconds, detailed void fraction variation with time is smoothed out. In order to visualize reasonable void fraction variation with time, an averaging time of 1 second is chosen. In the transient tests, this averaging time is used to maintain consistency with the results from the steady state tests.

The bubble velocity is estimated based on the time lag between the two signals and the distance between the two tips of the double-sensor conductivity probes. The raw signals of the double-sensor probes are converted into 0 or 1 by comparison with the threshold value. An example of two signals from a double-sensor conductivity probe is shown in Figure A-9.

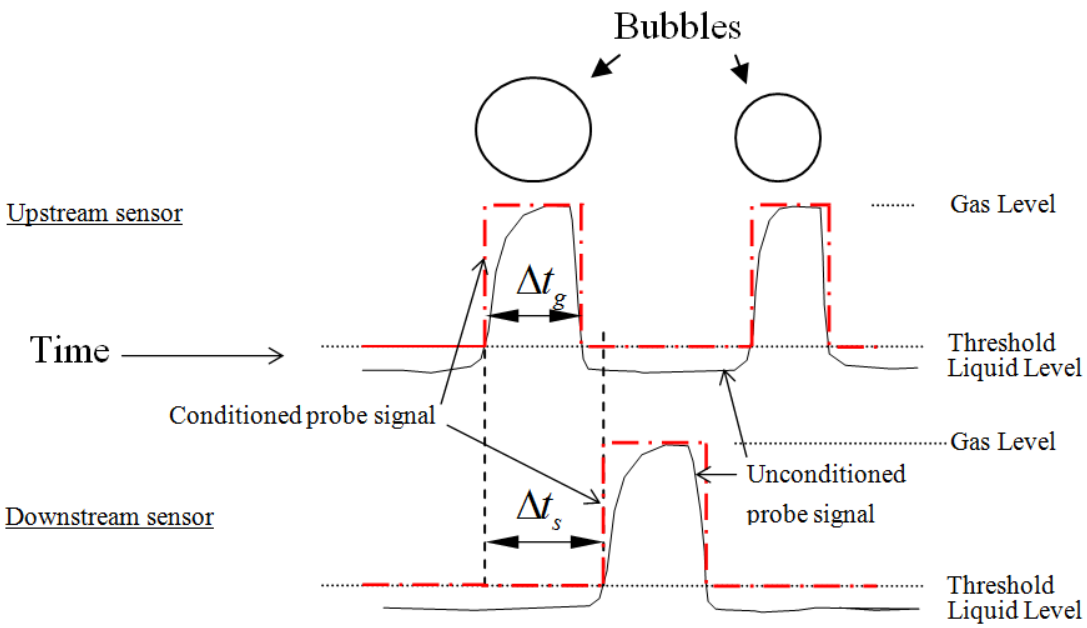

Figure A-9 Example of Two-Signal from the Double-sensor Conductivity Probe

The bubble velocity is calculated based on the following equation.

$$Bubble\ velocity\ (v_b) = \frac{d}{\Delta t} \tag{A.2}$$

where

d = distance between the two tips of a double-sensor conductivity probe

Δt = time lag between the two consecutive signals

Due to the limitation of the double-sensor conductivity probes, this calculated bubble velocity is only the axial component of the interfacial velocity.

The bubble chord length is calculated based on the bubble velocity obtained from Equation A.2 and the time period that the probe is covered by the gas phase. The following equation is used to calculated the bubble chord length.

$$Bubble\ chord\ length\ (L) = v_b \times \Delta t_s \tag{A.3}$$

where

v_b = bubble velocity

Δt_s = time period that the probe is covered by gas phase

A.1.3 Pressure Measurement

The experimental facility uses pressure transducers manufactured by Honeywell (Model STD 924) for differential pressure measurements. The accuracy is ± 25 Pa (0.0036 psi) for upper range values less than 25 kPa (3.6 psi) and ± 0.1% of the maximum pressure for upper range values exceeding 25 kPa (3.6 psi). Model STG 944 pressure transducers manufactured by Honeywell are used for absolute pressure measurements with an accuracy of ± 3.2 kPa (0.46 psi).

The pressure sensors measure the gauge pressures and transmit a 4 to 20 mA signal. The DAS measures the voltages across 250 Ω (± 0.1 Ω) resistors. The data conversion program converts the 1 to 5 volt signals into engineering units as follows:

$$\phi = \phi_{\min} + \frac{\left(\phi_{\max} - \phi_{\min}\right)}{\left(V_{\max} - V_{\min}\right)} \times \left(V - V_{\min}\right) \tag{A.4}$$

where

ϕ	:	output in engineering units
$\phi_{\min}$	:	instrument range minimum
$\phi_{\max}$	:	instrument range maximum
V	:	voltage output (Volts)
$V_{\min}$	:	minimum output voltage (Volts)
$V_{\max}$	:	maximum output voltage (Volts)

For the present case $\phi = P_g$, the gauge pressure. Then, the absolute pressures are calculated as follows:

$$P_a = P_g + P_b \tag{A.5}$$

where P_a is the absolute pressure (kPa) and P_b is the barometric pressure (kPa).

A.1.4 Temperature Measurement

The experimental facility uses sheathed K-type thermocouples manufactured by OMEGA Engineering, Inc. The thermocouple signals, in mV, are converted directly into engineering units through the Labview program. The range of the K-type thermocouples is -200~1250 °C (-328~2280 °F) and the thermocouple limits of error is 2.2 °C (4 °F) or ± 0.7% of reading.

A.1.5 Air Flow Rate Measurement

For the steady state tests, two Foxboro vortex flow meters (Model 84W) are installed on the parallel 0.05 m (2 in.) and 0.02 m (¾ in.) pipelines to measure air flow for high and low flow rate conditions, respectively. The vortex flow meter works on the principle that a disturbance in the flow field generates vortices, which are proportional to the flow rate. The flow can be measured

by counting the number of vortices per unit time. The measurable range of each vortex meter used in this experiment is listed in the Section A.4. There is an accuracy of ± 1% of the maximum and minimum flow rate. The output from the vortex flow meter is a 4 to 20 mA signal. It is converted into engineering units using Equation A.4. The standard calibration for a vortex flow meter is performed by the manufacturer before delivery.

A.1.6 Nozzle Flow Rate Measurement

For the transient tests, both the pressure difference across a nozzle or a venturi and the upstream pressure are measured by pressure transducer cells. This data, along with the nozzle specifications, is sufficient to calculate the mass flow rate. This is accomplished using the following equation (Ref. 7). Z_1 and F_a were compiled from figures and fit with a polynomial curve.

$$\dot{m} = \frac{A_2 Y F_a C_d}{\sqrt{1-\beta^4}} \sqrt{(2\rho)(P_1 - P_2)} \tag{A.6}$$

Here, A_2 is the area at the nozzle throat (m^2), $\dot{m}$ is mass flow rate in kg/s, P_1 and P_2 are upstream pressure and downstream pressure in kPa respectively, and Y is the expansion factor given by

$$Y = \left[\left(\frac{P_2}{P_1}\right)^{2/k} \left(\frac{k}{k-1}\right) \left(\frac{1-\left(\frac{P_2}{P_1}\right)^{(k-1)/k}}{1-\left(\frac{P_2}{P_1}\right)} \right) \left(\frac{1-\beta^4}{1-\beta^4\left(\frac{P_2}{P_1}\right)^{2/k}} \right) \right]^{1/2} \tag{A.7}$$

In Equation A.6, β is defined as the ratio of the nozzle diameters, D_1 and D_2

$$\beta = \frac{D_2}{D_1} \tag{A.8}$$

Pressure in Equation A.6 is in kPa, and F_a is the thermal expansion factor given by

$$F_a = 0.9992 + 3.346 \times 10^{-5} T_1 \tag{A.9}$$

with temperature in °C. C_d is the discharge coefficient given by

$$C_d = 0.99622 + 0.0232 D_1 - (6.36 + 5.11 D_1 - 0.24\beta^2) \frac{1}{\sqrt{\mathrm{Re}_{D_2}}} \tag{A.10}$$

where Re_{D_2} is Reynolds number corresponding to the diameter D_2.

The value of *k* in Equation A.7 is the ratio of specific heat given by

$$k = 1.3111 - 1.11 \times 10^{-5} P_1 \tag{A.11}$$

The density is calculated using the ideal gas law

$$\rho = \frac{P_1}{Z_1 R T_1} \tag{A.12}$$

with the pressure (P_1) in Pa, the gas constant (R) = 0.4615 kJ/kg-K, and temperature (T_1) in Kelvin (K). Finally, Z_1 is given by the following equation, with pressure in kPa

$$Z_1 = 0.9904 - 7.496 \times 10^{-5} P_1 + 1.369 \times 10^{-8} P_1^2 \tag{A.13}$$

Z_1 is the compressibility factor and relates steam to an ideal gas.

For this experiment, the accuracy of nozzle measurements is investigated by comparison between the RPV inventory water loss estimated by nozzle flow meters and the water level change measured by DP gauges in the RPV before and after the 0.102 m (4 in.) downcomer experiments. The results are shown in the Table A-1. It can be seen that the difference between the estimated inventory loss in the RPV is less than 10%.

Table A-1 Percent Difference of Water Inventory Loss in RPV from the Nozzles and DP Gauges.

Type of Steam Flow (No. of DPV opening)	Total Estimate of Inventory Loss in RPV		Percent Difference (%)
	Nozzles	Water Level Change from DP Gauge	
Small (2 DPVs)	97.8 kg (216 lbm)	107 kg (236 lbm)	-9.34
Medium (3 DPVs)	113 kg (249 lbm)	116 kg (256 lbm)	-2.95
High (5 DPVs)	151 kg (333 lbm)	164 kg (362 lbm)	-7.75

A.1.7 Oxygen Concentration Measurement

The experimental facility uses RM CEM O2/IQ analyzers manufactured by AMETEX/Thermox to measure oxygen concentration. The machines mainly consist of three basic systems: the plumbing, the measuring system, and the temperature system. The measuring element is a closed-end tube or disk made from ceramic zirconium oxide stabilized with an oxide of yttrium or

calcium. Gases having different oxygen partial pressures on two sides of the cell will produce a potentiometric voltage. The magnitude of this voltage is a function of the ratio of the two oxygen partial pressures. Since a gas with reference oxygen concentration is contained on one side of the tube or disk, another oxygen concentration can be calculated (Ref. 8).

The operating range of the oxygen analyzer is 0.1-100% oxygen with an accuracy of $\pm$ 0.75% of readings or 0.05% O_2 absolute. The response time is less than 4 seconds to 90% step response change and less than 2 seconds to 63% step response change at 0.94 L/min (2 scfh) from 2% to 20% O_2. The maximum inlet temperature is 204 $^{\circ}$C (400 °F), sample pressure is $\pm$ 0.14 kg/cm^2 max (2 psig) and sample flow is 0.94 to 7.08 L/min (2 to 15 scfh) (Ref. 8).

For the transient tests, two oxygen analyzers are used to measure the oxygen concentrations at key locations in the facility. One is connected to the DC and another is connected to the upper DW. Since the sampling tubing used to transport gas from the DC and the DW to the machines is relatively long (DC machine tubing is 4.6 m [15 ft], DW machine tubing is 1.3 m [4.3 ft]), some heat belts are used to minimize heat loss in these pipes during the test. This is to prevent steam condensation inside the tubes, which could result in inaccurate measurements and damage to the machine. Also, the time necessary for gas to travel through these tubes to the sampling machine has been calculated and it has been considered in the data analysis.

The oxygen analyzers measure the oxygen concentration and transmit a 4 to 20 mA signal. The DAS measures the voltages across 250 Ω ($\pm$ 0.1 Ω) resistors. The data conversion program converts the resulting 1 to 5 volt signals to 0 to 20.9% oxygen concentration, or 0 to 100% noncondensable gas concentration.

A.1.8 High-speed Video Camera

A high-speed camera (Model No. PHOTRON-FASCAM SA-3) with a maximum recording rate of 10,000 frames per second (fps) is available at the PUMA-E facility. For the steady state tests, 250 fps with a maximum recording time of around 9 seconds per recording is used. For the transient tests, 60 fps with a maximum recording time of around 9 seconds per recording is applied. The high-speed camera is applied to visualize the transient venting phenomena of the gas plume around the exit of the downcomer. Captured digital images can be transferred and recorded in the computer.

A.2 Instrumentation Location

This chapter describes the locations of important instruments for the steady state and transients tests. Figure A-10 shows various symbols used to portray components in the instrument location drawings for both tests.

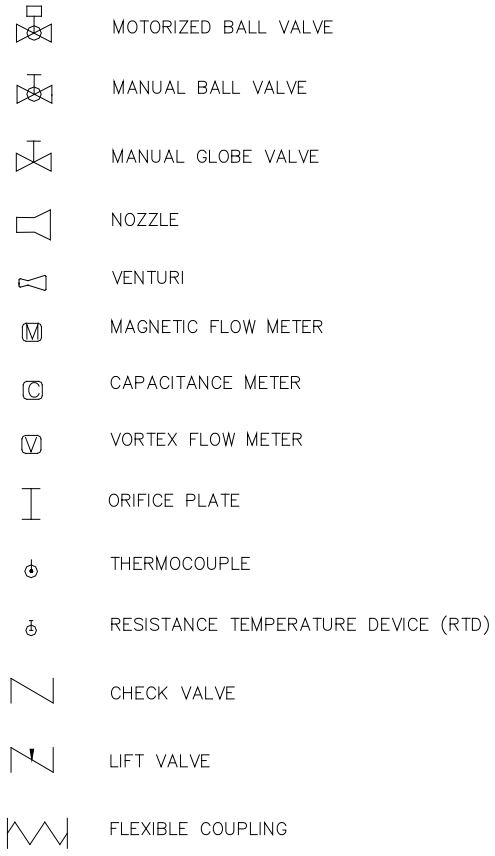

Figure A-10 Symbols Used in Isometric Drawings for Instrument Location

A.2.1 Instrumentation Location for Steady State Tests

The locations of instrumentation for steady state tests in the SP are shown in Figure A-11. These instruments include two thermocouples (TE-SP-04, TE-SP-09), an absolute pressure gauge (PT-SP-01), and a differential pressure gauge (LT-SP-01) for water level measurement. A differential pressure gauge (LT-DC-01) between the air line connected to the SRV line and the gas space in the SP is installed to estimate the water level in the downcomer as shown in the figure.

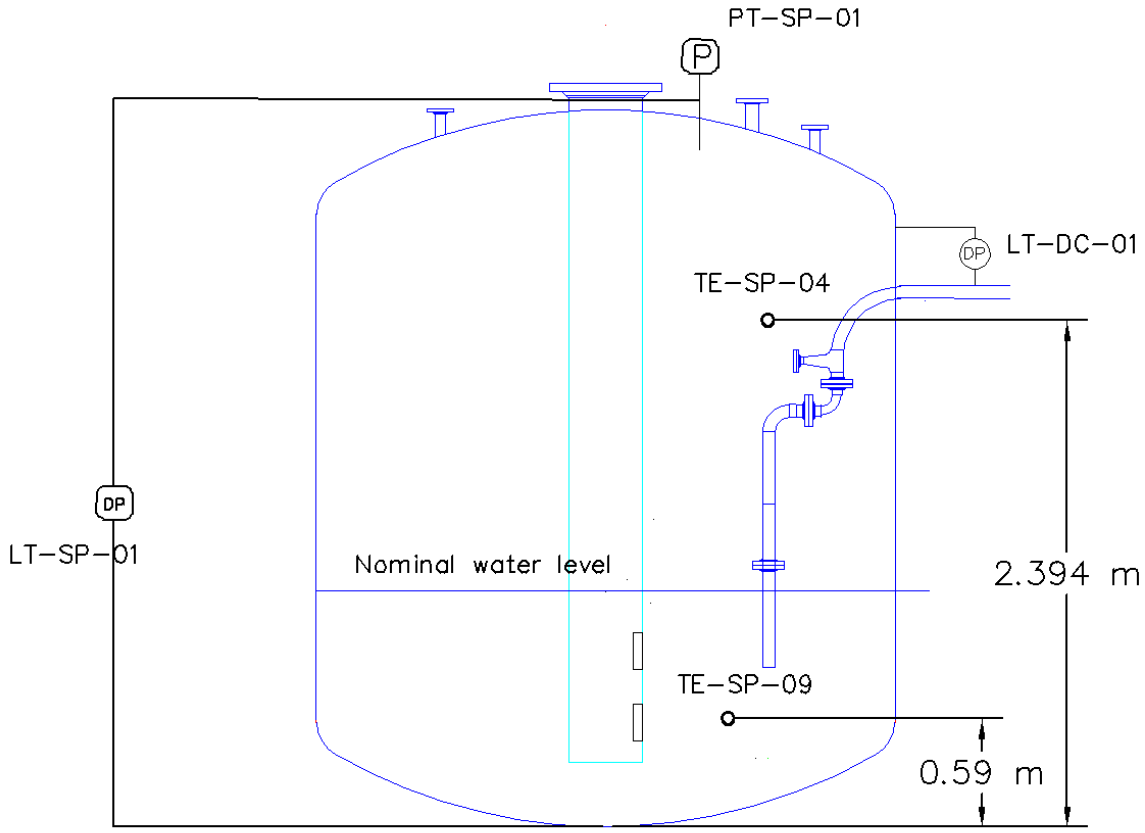

Figure A-11 Locations of Pressure and Water Level Measurement in SP

The conductivity probe locations on the supporting cage, which are based on the distance from the center of the downcomer exit, are shown in Section A.5.

The locations of instruments in the air supply line are shown in Figure A-12. These instruments include two thermocouples (TE-AL-01, TE-AL-02), two absolute pressure gauges (PT-AL-01, PT-AL-02), and two vortex flow meters (FT-AL-01, FT-AL-02).

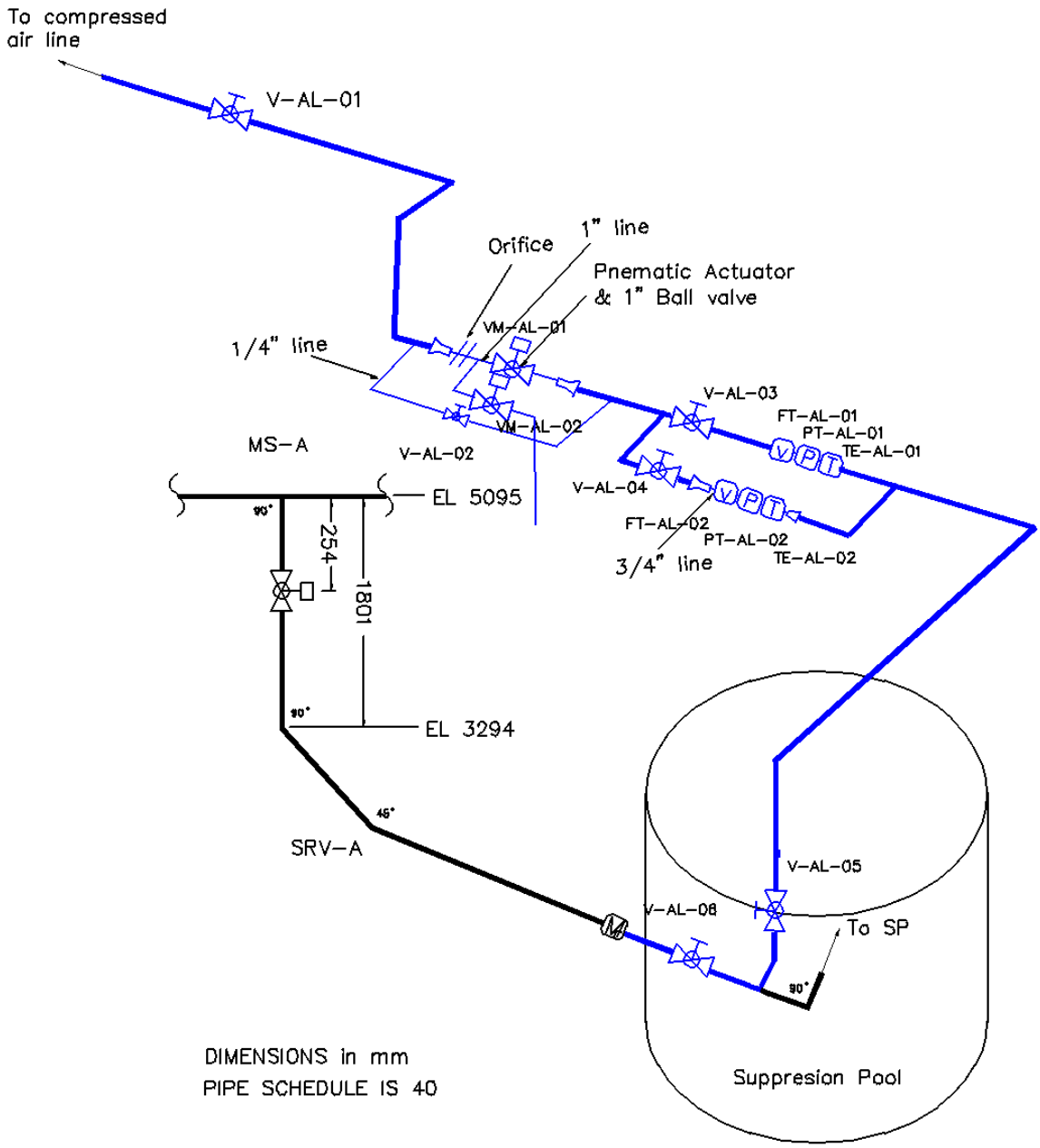

Figure A-12 Locations of Pressure, Temperature, and Air Flow Rate Measurement in the Air Supply Line

A.2.2 Instrumentation Location for Transient Tests

The locations of instrumentation in the DW are shown in Figure A-13. This instrumentation includes a pressure transmitter (PT-DW-01), three thermocouples (TE-DW-01, TE-DW-02 and TE-DW-09), and the oxygen analyzer (AI-DW-01).

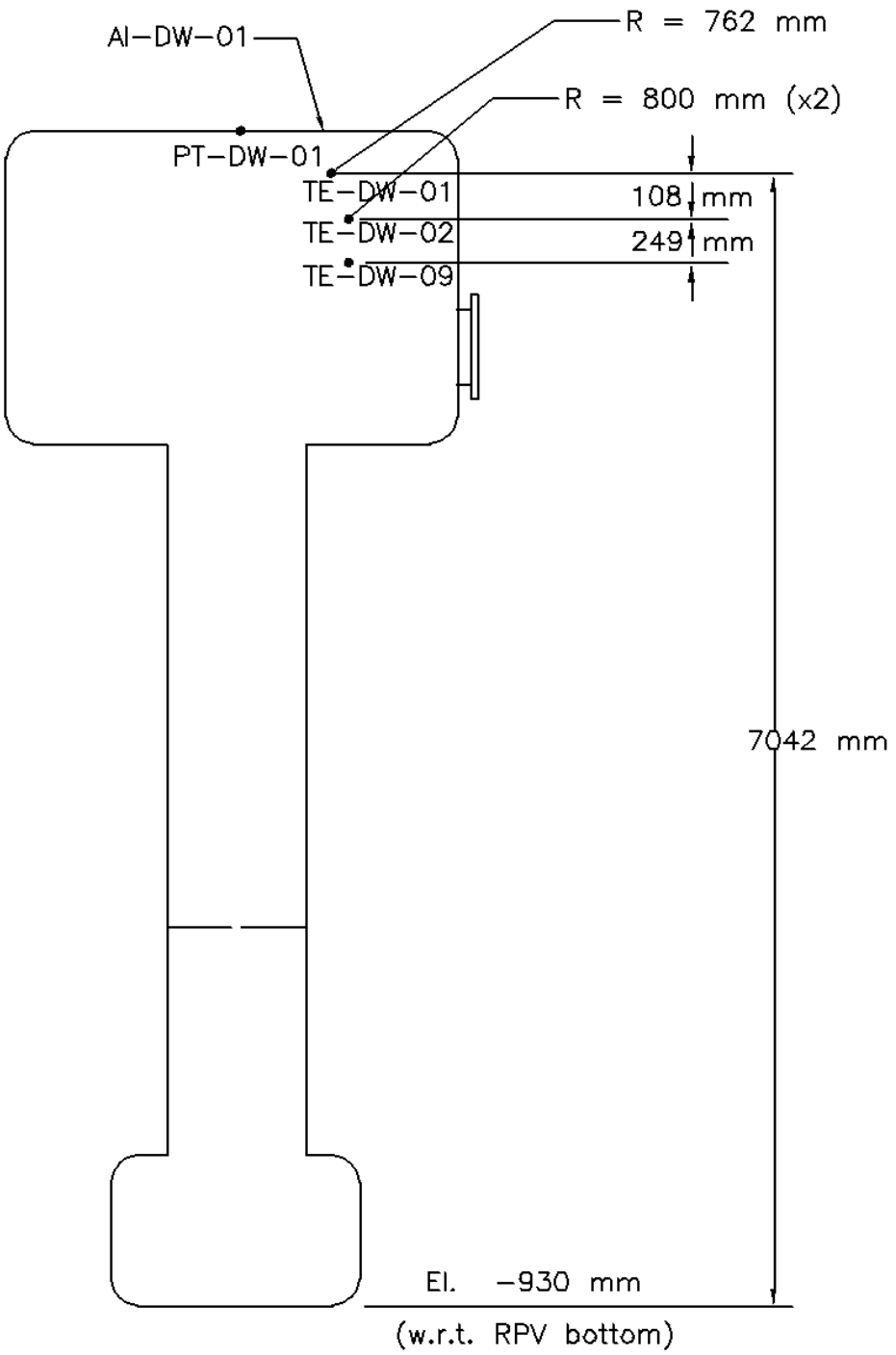

Figure A-13 Locations of Instrumentation in the DW

The locations of instrumentation in the SP are shown in Figure A-14. This instrumentation includes two thermocouples (TE-SP-08 and TE-SP-09), the oxygen analyzer (AI-DC-01), the high-speed camera, and the conductivity probe cage.

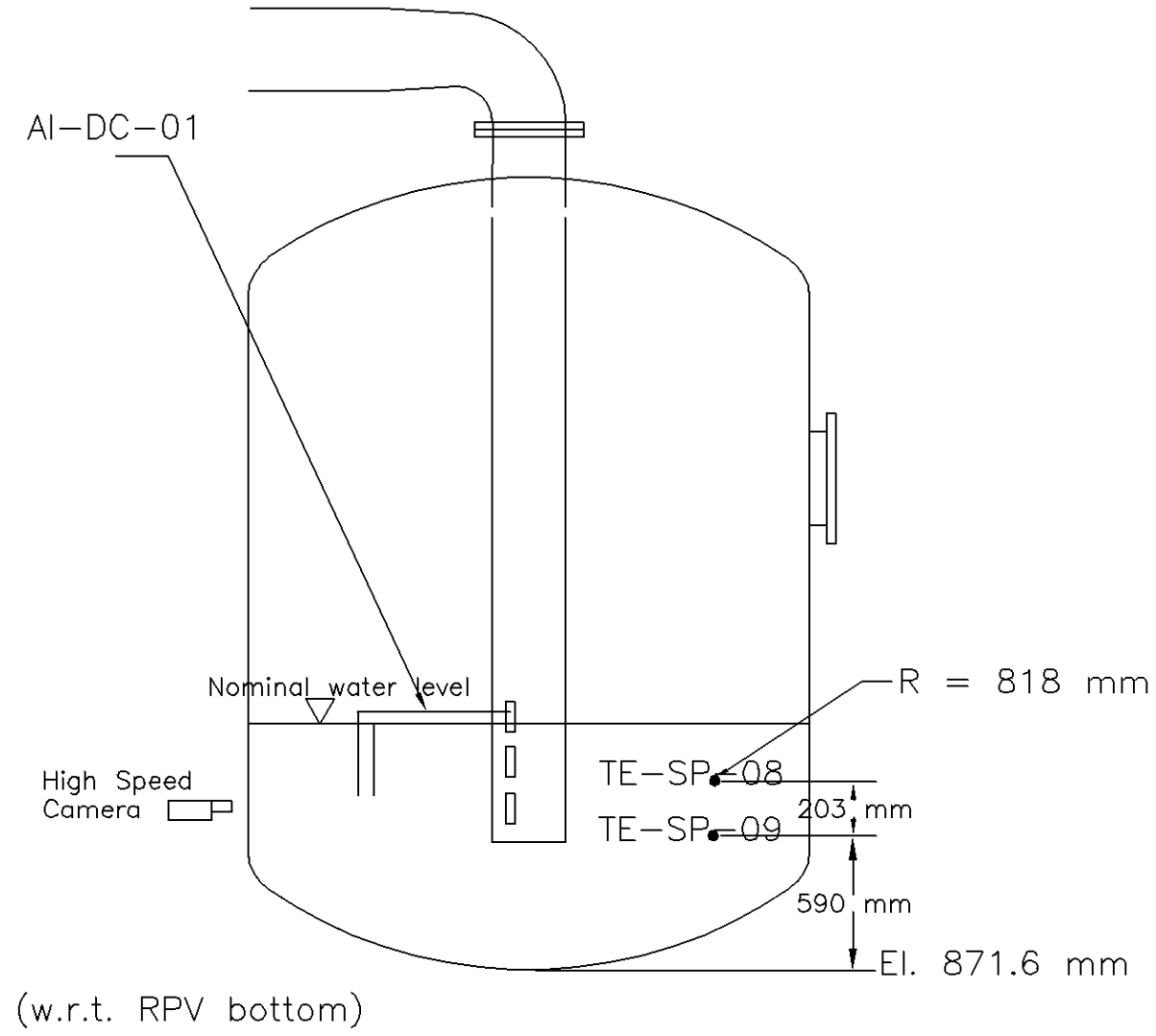

Figure A-14 Locations of Instrumentation in the SP

The exact conductivity probe locations on the supporting cage in the SP are shown in Section A.5. The supporting cage is centered on the exit of the downcomer (for either size, 0.102 m or 0.076 m [4 in. or 3 in.]).

The locations of the instrumentation in each break line are shown in Figures A-15 to A-18.

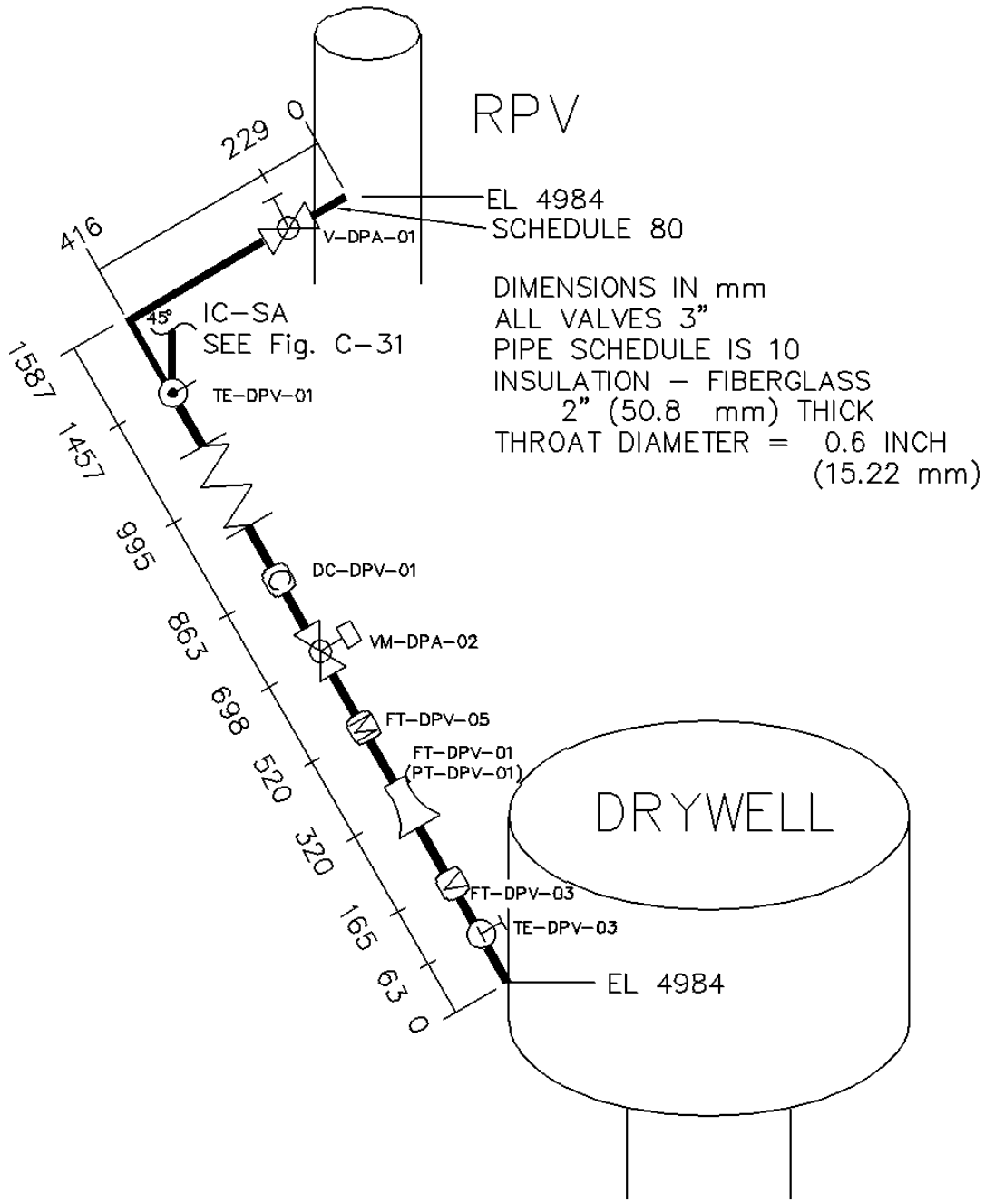

Figure A-15 DP-A Line from RPV to Drywell

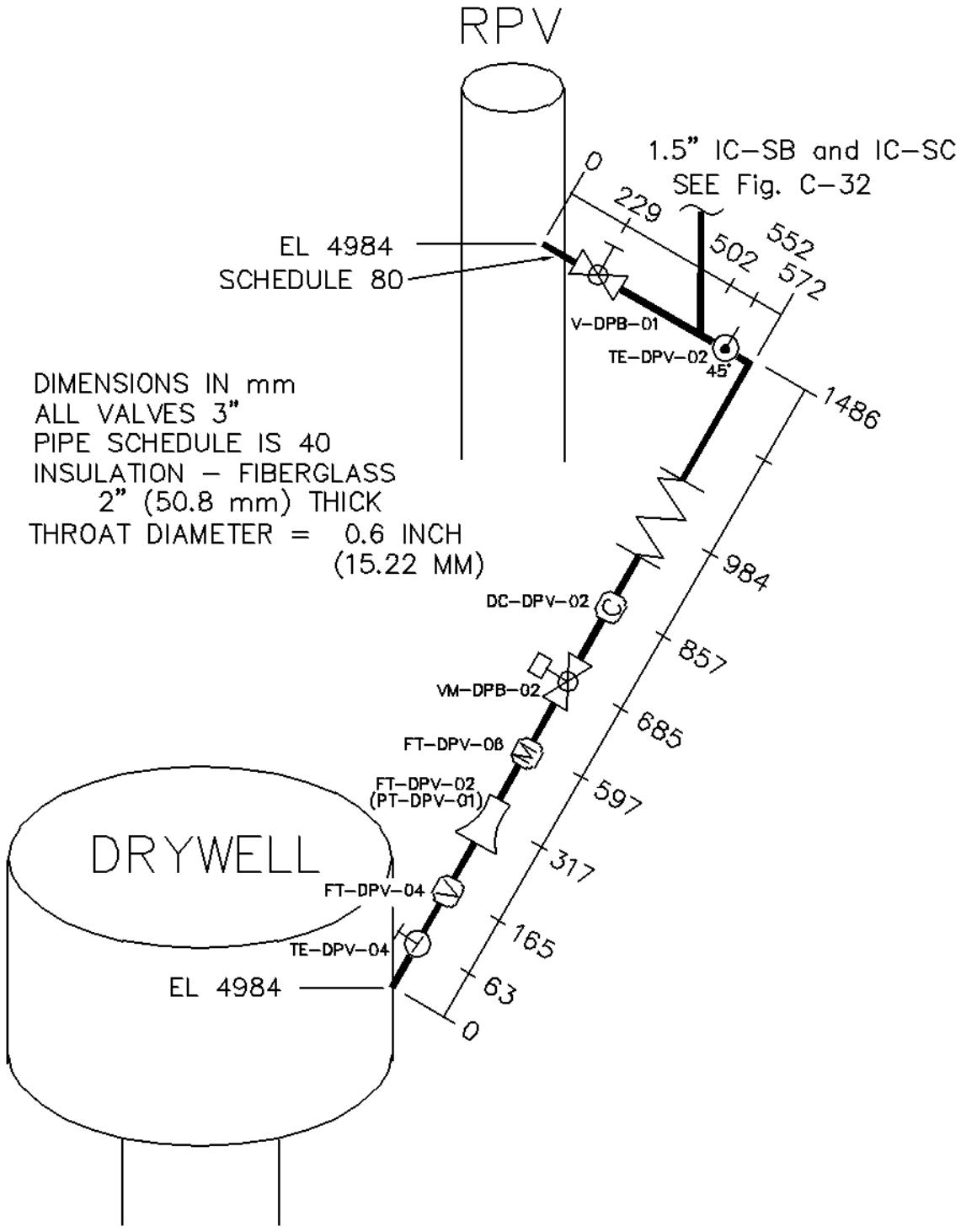

Figure A-16 3" DP-B Line from RPV to Drywell

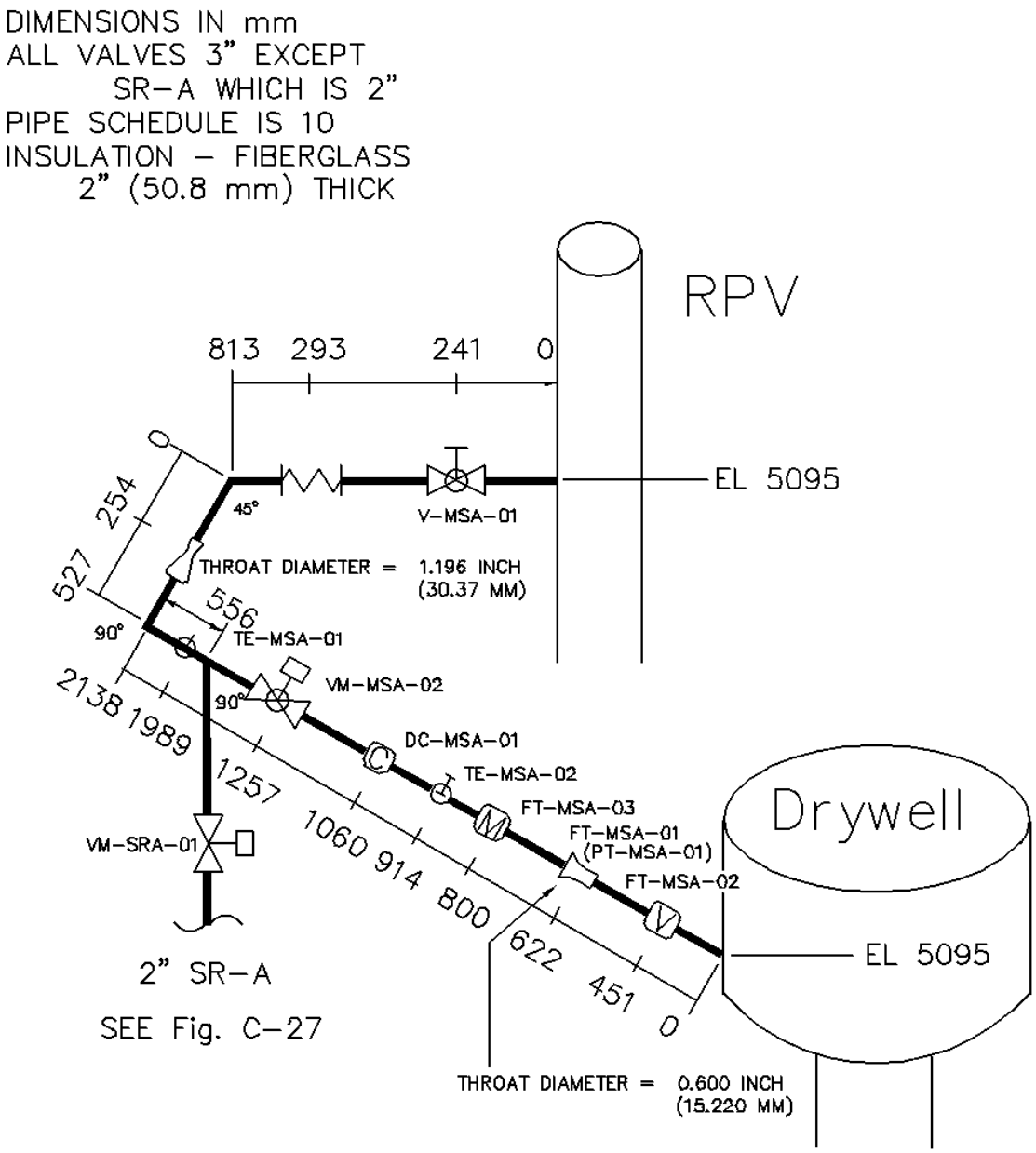

Figure A-17 3" MS-A Line from RPV to Drywell

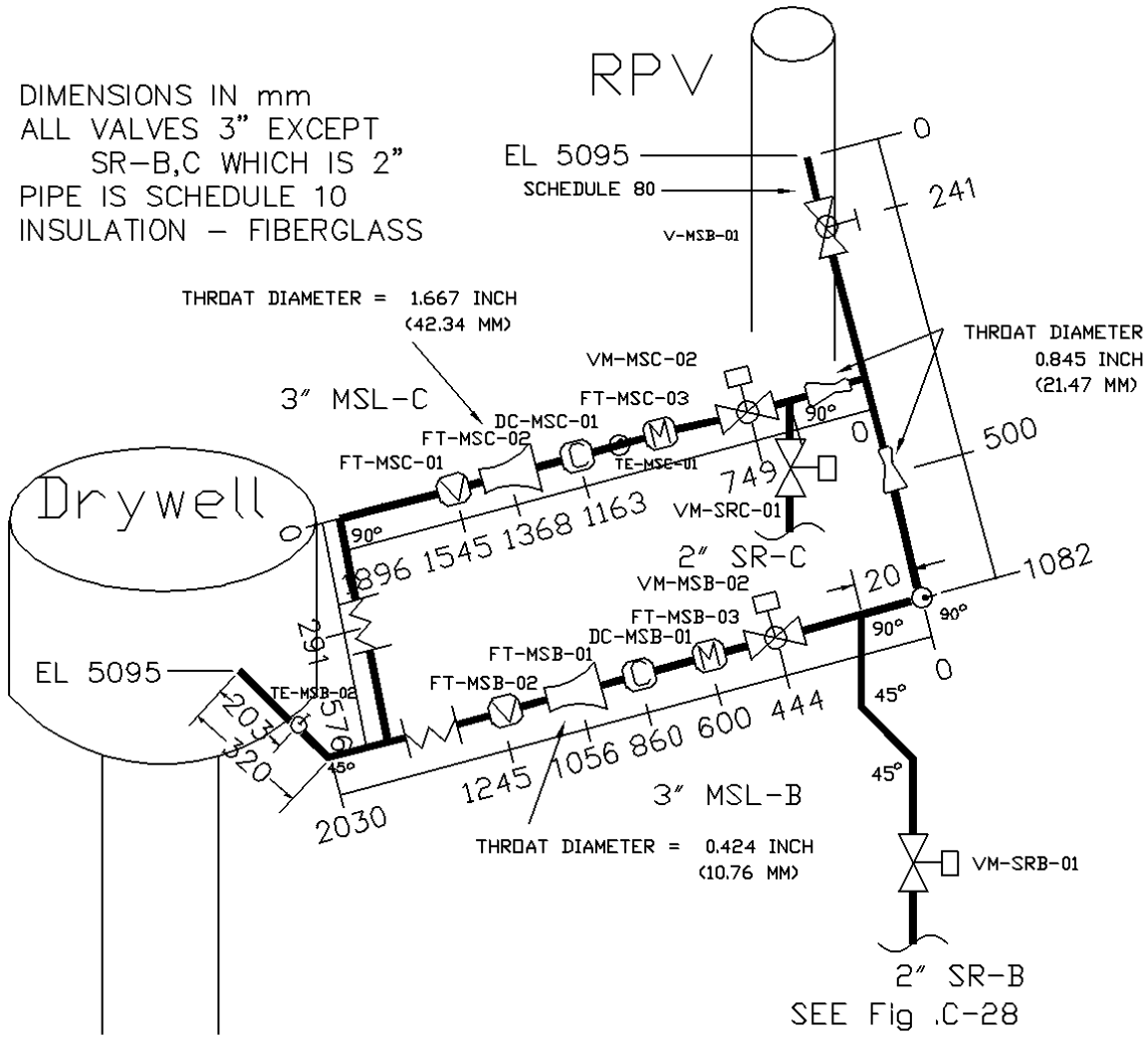

FT-MSC-02 : 0.424'' (10.76 mm) for the transient tests

Figure A-18 3" MSL-B and MSL-C Lines from RPV to Drywell

A.3 Data Acquisition System (DAS) and Valve Control System

The DAS for the steady state tests and transient tests is explained in this chapter. The same DAS for the conductivity probes and high-speed camera is used for the both tests. The DAS for other measurements is different between the steady state and transient tests.

A.3.1 DAS and Valve Control System for Steady State Tests

The data acquisition, valve control, and data processing are archived using three computers. The experimental data are stored in personal computers (PC) directly. The sampling rate is 4666 Hz. Two National Instruments USB-6225 modules are used for the data acquisition. Each of the USB-6225 modules has the capability to handle 80 analog inputs.

PC#1 is mainly used to acquire data on pressure, temperature, air flow rate, some of the conductivity probes, and to control opening and closing of the pneumatic ball valve. PC#2 acquires data from the remaining conductivity probes. PC#3 is mainly utilized to record flow visualization from the high-speed movie camera.

A.3.2 DAS and Valve Control System for Transient Tests

The data acquisition for the transients test has two different system. One is the DAS used for conductivity probes and high-speed camera. Another is the DAS used for other instruments and the control system.

A.3.2.1 DAS for Conductivity Probes and High-speed Camera

The data acquisition for conductivity probes and high-speed camera is archived using three computers. The conductivity probe data are stored in personal computers directly. The sampling rate is 3896 Hz. Two National Instruments USB-6225 modules are used for the data acquisition.

PC#1 and #2 acquire the data from the conductivity probes. PC#3 is mainly utilized to record flow visualization from the high-speed movie camera.

A.3.2.2 DAS for Other Instruments and Control System

The DAS for other instruments and the control system used to perform the transient tests was originally used in performing integral tests in the PUMA-E facility. The DAS for temperature and pressure, heater, and valve controls is based on a network of three personal computers. The sampling rate is 2 Hz or faster for all instruments. Data is stored directly in the hard disk of the sampling computer.

Keithly-Metrabyte A/D and D/A converter boards are used throughout the DAS. The main software for data acquisition is Labtech Notebook. Some software for data acquisition and the control modules were developed at Purdue and written in the C programming language. All of the software runs under the DOS or Windows platforms. Each PC works independently except for the initial trigger which is generated by the control PC (PC #6) or a human operator.

PC #4 is fully dedicated to acquiring the temperature data. Two DAS-801 boards and fourteen EXP-16 terminal boards are used. The software is Labtech. The sampling rate is 2 Hz.

PC #5 acquires the pressure, magnetic flow meter, oxygen concentration, heat flux, and vortex flow meter signals. The hardware and software are the same as those used for PC #4. The sampling rate is 5 Hz.

PC #6 is the control PC. It has a DAS-801 board with an EXP-16 terminal to input the narrow and wide range level signals from the RPV and the heater powers. It is controlled through a PIO-24 board with two SSIO-24 terminals. This computer controls the power to the three banks of heater rods and the timing signals for the test initiation and the ADS valve control.

A.4 List of Pressure, Water Level, Temperature, and Flow Measurements

Table A-2 Pressure and Level Measurements.

TAG NUMBER	COMPONENT	MEASUREMENT	RANGE (Min)	RANGE (Max)	UNITS
PT-SP-01	SP	Pressure	0	500	kPa
LT-SP-01	SP	Diff.Pressure	0	33.718	kPa
PT-DW-01	DW	Pressure	0	500	kPa
LT-DC-01	DOWNCOMER	Diff.Pressure	0	5	kPa
PT-AL-01	AIR LINE	Pressure	0	1500	kPa
PT-AL-02	AIR LINE	Pressure	0	1500	kPa

Table A-3 Temperature Measurements.

TAG NUMBER	COMPONENT	MEASUREMENT	RANGE (Min)	RANGE (Max)	UNITS
TE-SP-04	SP	Temperature	-200	1250	°C
TE-SP-08	SP	Temperature	-200	1250	°C
TE-SP-09	SP	Temperature	-200	1250	°C
TE-AL-01	2”AIR LINE	Temperature	-200	1250	°C
TE-AL-02	¾”AIR LINE	Temperature	-200	1250	°C
TE-DW-01	DW	Temperature	-200	1250	°C
TE-DW-02	DW	Temperature	-200	1250	°C

Table A-4 Flow Measurement.

TAG NUMBER	COMPONENT	MEASUREMENT	RANGE (Min)	RANGE (Max)	UNITS
FT-AL-01	2”AIR LINE	FLOW RATE	7.95	692.8	m^3/h
FT-AL-02	¾”AIR LINE	FLOW RATE	1.12	58.41	m^3/h
FT-DPV-A	3” DP-A LINE	FLOW RATE	0	500	kPa
FT-DPV-B	3” DP-B LINE	FLOW RATE	0	500	kPa
FT-MS-A	3” MS-A LINE	FLOW RATE	0	500	kPa
FT-MS-C	3” MS-C LINE	FLOW RATE	0	500	kPa

A.5 List of Conductivity Probe Locations

The configuration of probe locations in each level is shown in Figure A-3 and Figures A-19 to A-27. Table A-5 shows the type and location of each conductivity probe. The axial and radial locations of probes are measured from the level of the downcomer exit. The red circles represent the single-sensor conductivity probes and the blue circles represent the double sensor probes.

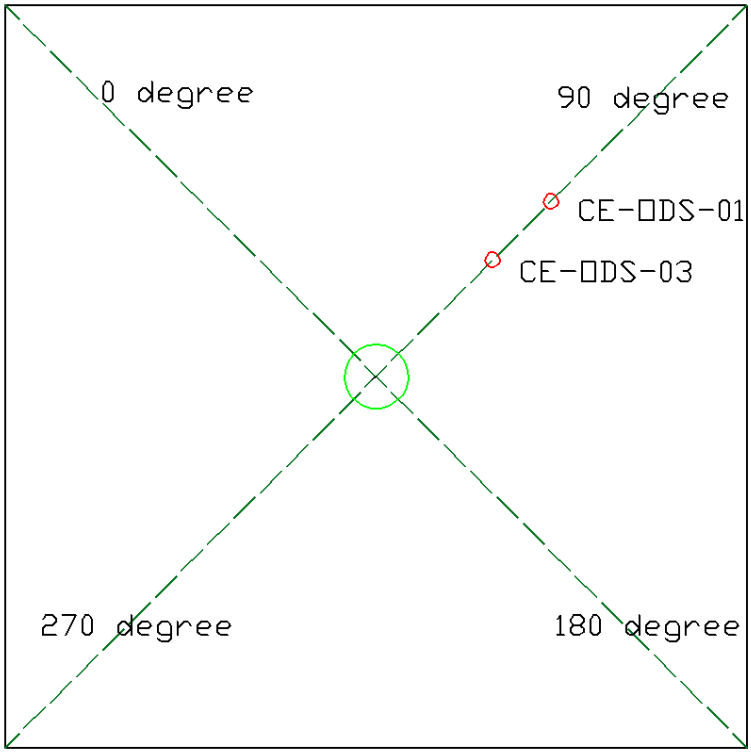

Figure A-19 Configuration of Conductivity Probes on Level O (0.18 m [0.59 ft] above downcomer exit)

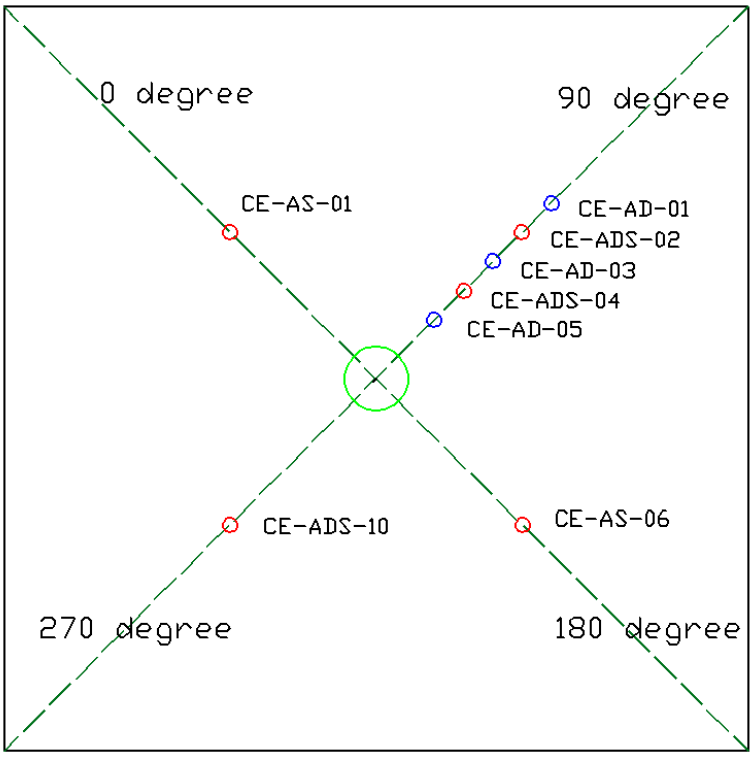

Figure A-20 Configuration of Conductivity Probes on Level A (0.08 m [0.26 ft] above downcomer exit)

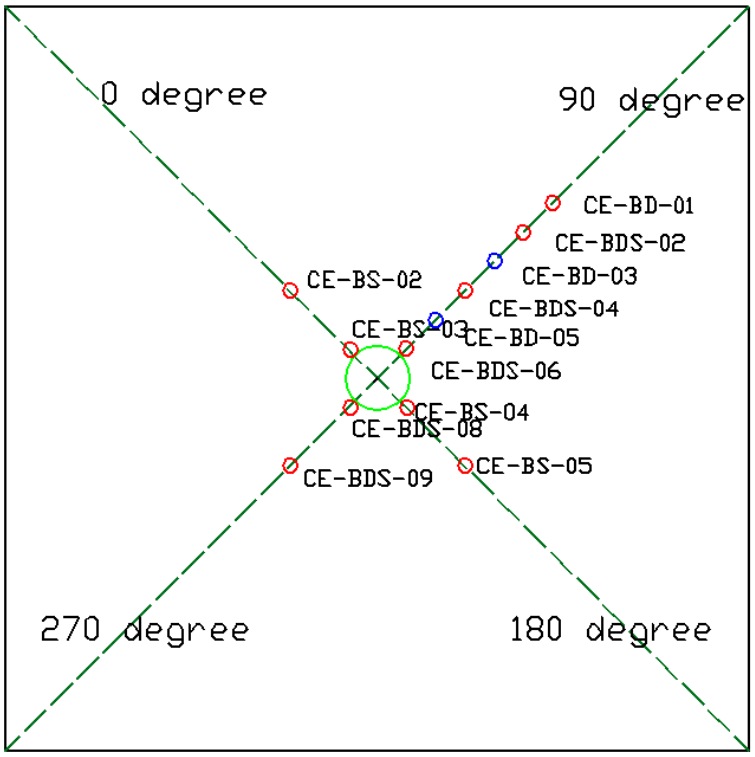

Figure A-21 Configuration of Conductivity Probes on Level B (0.02 m [0.07 ft] above the level of downcomer exit)

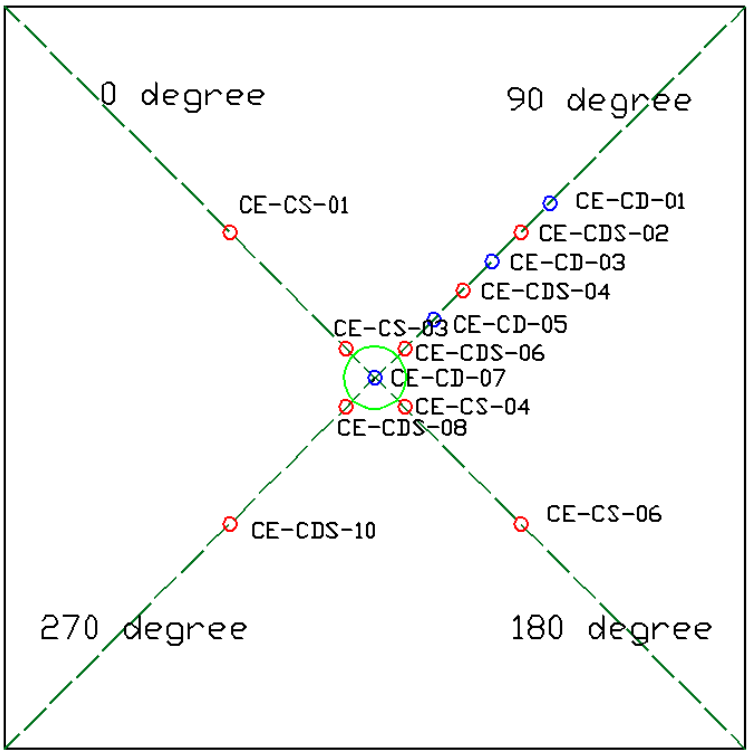

Figure A-22 Configuration of Conductivity Probes on Level C (0.11 m [0.36 ft] below the level of downcomer exit)

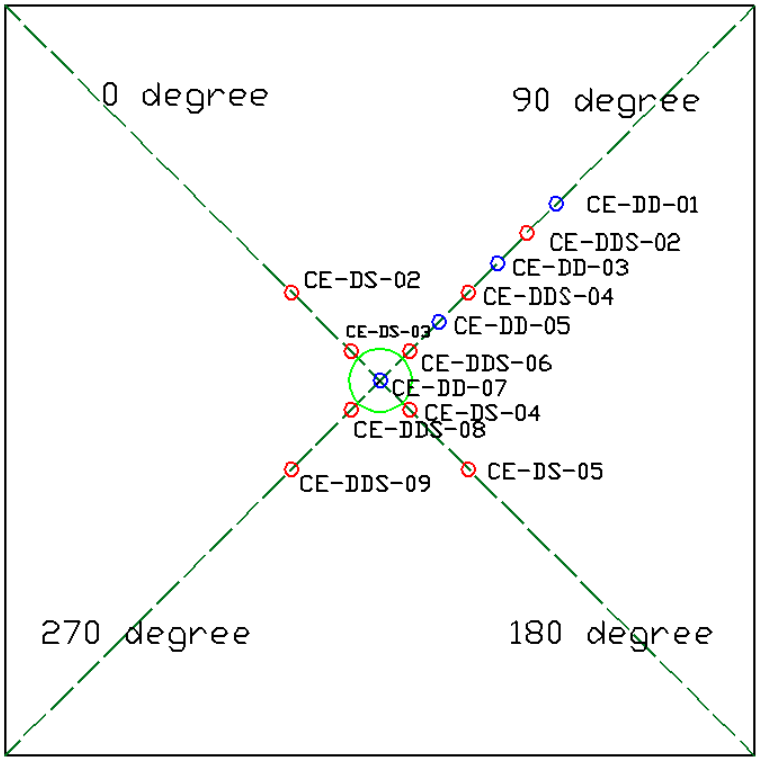

Figure A-23 Configuration of Conductivity Probes on Level D (0.21 m [0.69 ft] below the level of downcomer exit)

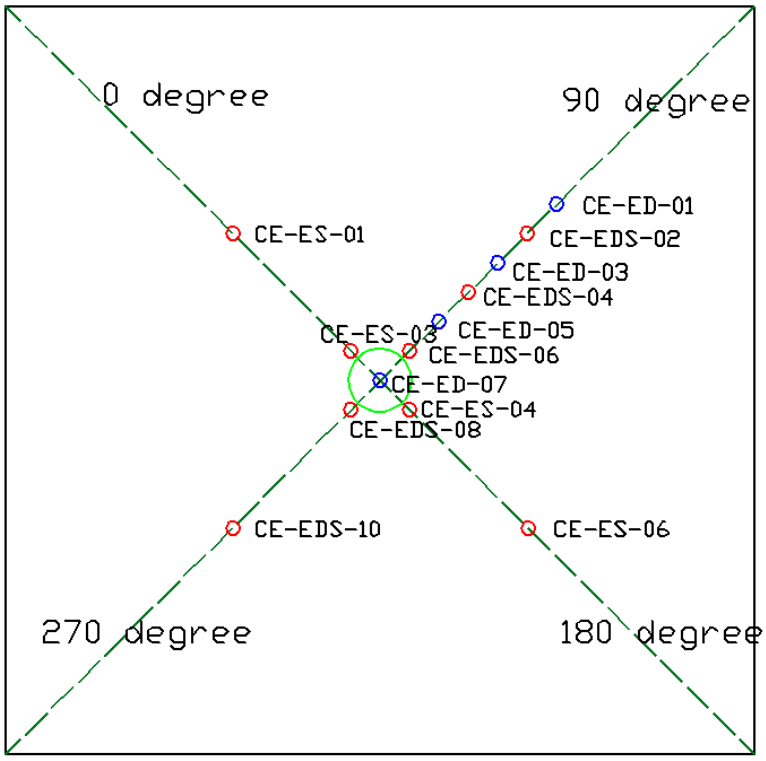

Figure A-24 Configuration of Conductivity Probes on Level E (0.31 m [1.02 ft] below the level of downcomer exit)

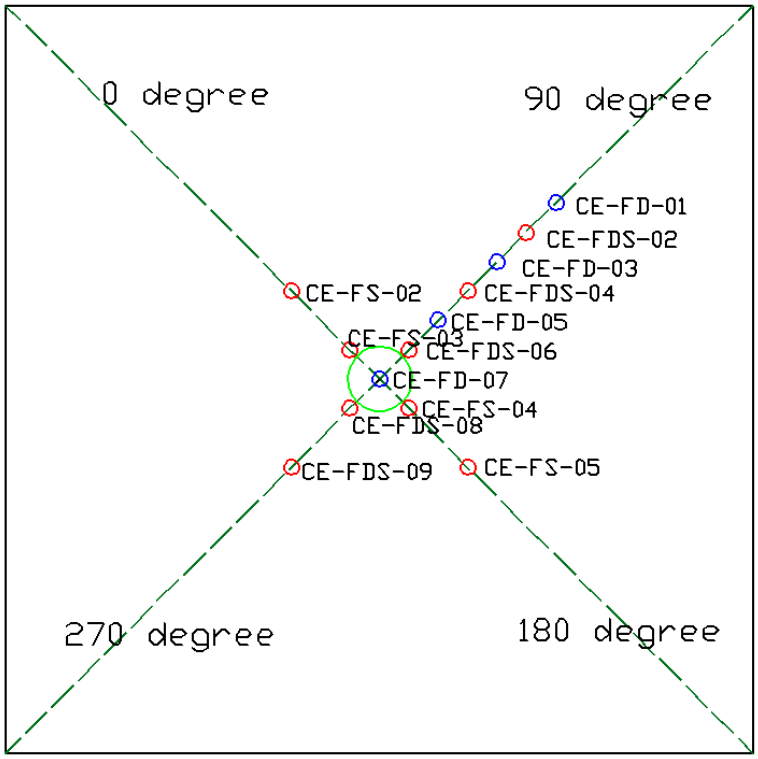

Figure A-25 Configuration of Conductivity Probes on Level F (0.41 m [1.35 ft] below the level of downcomer exit)

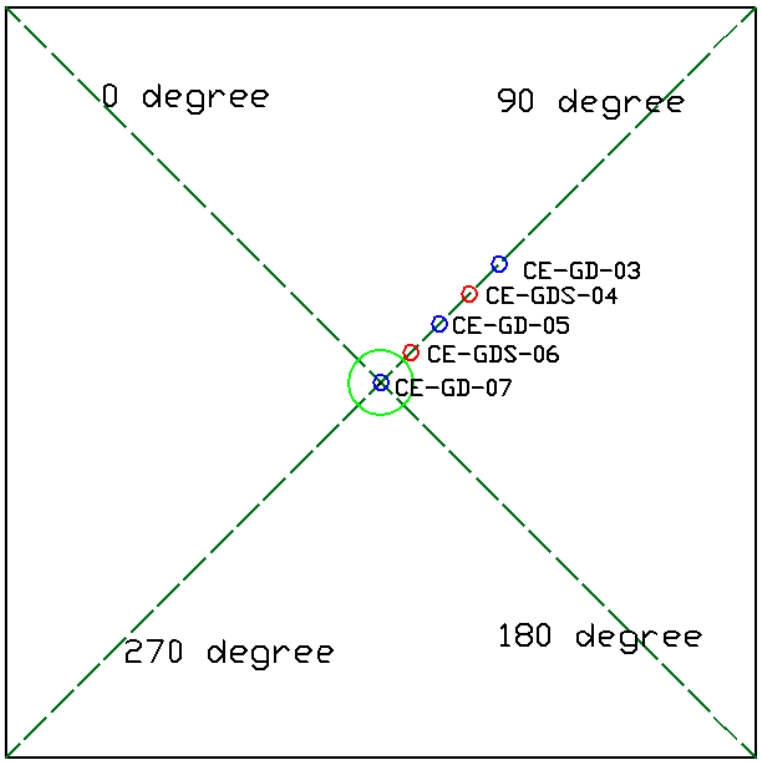

Figure A-26 Configuration of Conductivity Probes on Level G (0.51 m [1.67 ft] below the Level of Downcomer Exit)

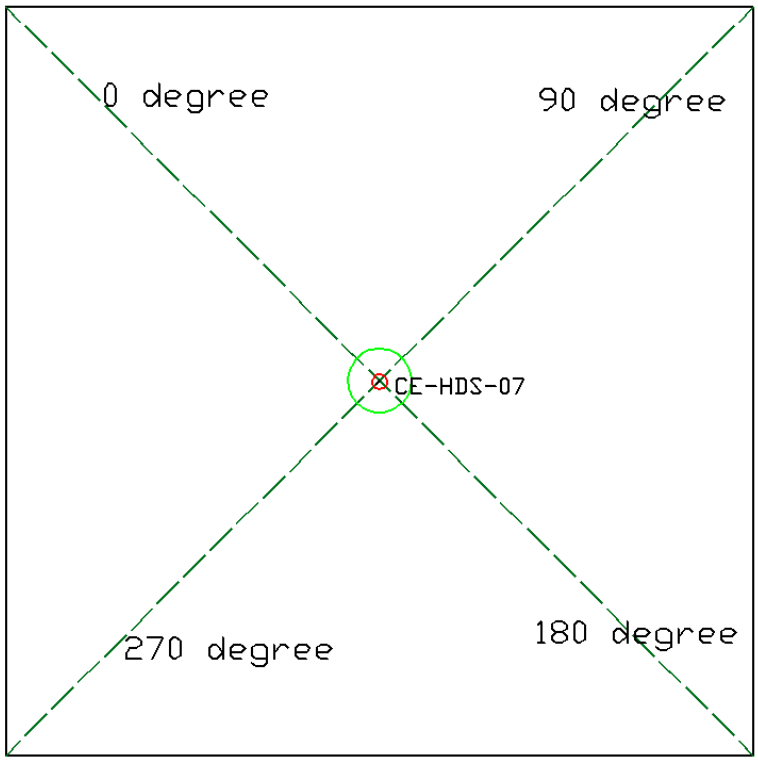

Figure A-27 Configuration of Conductivity Probes on Level H (0.61 m [2.0 ft] below the Level of Downcomer Exit)

The axial location (h) “+” and “-” means the position of the probe is above or below the level of the downcomer exit, respectively. The radial location (r) is the distance from the vertical axis passing through the center of downcomer exit. The double-L and double-S mean the long and short tip of double-sensor conductivity probe, respectively. The azimuthal angle can be seen in Figure A-3.

Table A-5 Type and Location of Conductivity Probes

TAG NUMBER	COMPONENT	TYPE OF SENSOR	AXIAL LOCATION (m [in])	RADIAL LOCATION (m [in])	AZIMUTHAL ANGLE (°)
CE-ODS-01	CAGE	Single	+0.18 [+7.09]	0.3 [11.81]	90
CE-ODS-06	CAGE	Single	+0.18 [+7.09]	0.2 [7.87]	90
CE-AS-01	CAGE	Single	+0.08 [+3.15]	0.25 [9.84]	0
CE-AS-06	CAGE	Single	+0.08 [+3.15]	0.25 [9.84]	180
CE-AD-01	CAGE	Double-L	+0.08 [+3.15]	0.3 [11.81]	90
CE-AD-01s	CAGE	Double-S	+0.08 [+3.15]	0.3 [11.81]	90
CE-ADS-02	CAGE	Single	+0.08 [+3.15]	0.25 [9.84]	90
CE-AD-03	CAGE	Double-L	+0.08 [+3.15]	0.2 [7.87]	90
CE-AD-03s	CAGE	Double-S	+0.08 [+3.15]	0.2 [7.87]	90
CE-ADS-04	CAGE	Single	+0.08 [+3.15]	0.15 [5.91]	90
CE-AD-05	CAGE	Double-L	+0.08 [+3.15]	0.1 [3.94]	90
CE-AD-05s	CAGE	Double-S	+0.08 [+3.15]	0.1 [3.94]	90
CE-ADS-10	CAGE	Single	+0.08 [+3.15]	0.25 [9.84]	270
CE-BS-02	CAGE	Single	-0.02 [-0.79]	0.15 [5.91]	0
CE-BS-03	CAGE	Single	-0.02 [-0.79]	0.05 [1.97]	0
CE-BS-04	CAGE	Single	-0.02 [-0.79]	0.05 [1.97]	180
CE-BS-05	CAGE	Single	-0.02 [-0.79]	0.15 [5.91]	180
CE-BD-01	CAGE	Double-L	-0.02 [-0.79]	0.3 [11.81]	90
CE-BD-01s	CAGE	Double-S	-0.02 [-0.79]	0.3 [11.81]	90
CE-BDS-02	CAGE	Single	-0.02 [-0.79]	0.25 [9.84]	90
CE-BD-03	CAGE	Double-L	-0.02 [-0.79]	0.2 [7.87]	90
CE-BD-03s	CAGE	Double-S	-0.02 [-0.79]	0.2 [7.87]	90
CE-BDS-04	CAGE	Single	-0.02 [-0.79]	0.15 [5.91]	90
CE-BD-05	CAGE	Double-L	-0.02 [-0.79]	0.1 [3.94]	90

Table A-5 (continued) Type and Location of Conductivity Probes

TAG NUMBER	COMPONENT	TYPE OF SENSOR	AXIAL LOCATION (m [in])	RADIAL LOCATION (m [in])	AZIMUTHAL ANGLE (°)
CE-BD-05s	CAGE	Double-S	-0.02 [-0.79]	0.1 [3.94]	90
CE-BDS-06	CAGE	Single	-0.02 [-0.79]	0.05 [1.97]	90
CE-BDS-08	CAGE	Single	-0.02 [-0.79]	0.05 [1.97]	270
CE-BDS-09	CAGE	Single	-0.02 [-0.79]	0.15 [5.91]	270
CE-CS-01	CAGE	Single	-0.11 [-4.33]	0.25 [9.84]	0
CE-CS-03	CAGE	Single	-0.11 [-4.33]	0.05 [1.97]	0
CE-CS-04	CAGE	Single	-0.11 [-4.33]	0.05 [1.97]	180
CE-CS-06	CAGE	Single	-0.11 [-4.33]	0.25 [9.84]	180
CE-CD-01	CAGE	Double-L	-0.11 [-4.33]	0.3 [11.81]	90
CE-CD-01s	CAGE	Double-S	-0.11 [-4.33]	0.3 [11.81]	90
CE-CDS-02	CAGE	Single	-0.11 [-4.33]	0.25 [9.84]	90
CE-CD-03	CAGE	Double-L	-0.11 [-4.33]	0.2 [7.87]	90
CE-CD-03s	CAGE	Double-S	-0.11 [-4.33]	0.2 [7.87]	90
CE-CDS-04	CAGE	Single	-0.11 [-4.33]	0.15 [5.91]	90
CE-CD-05	CAGE	Double-L	-0.11 [-4.33]	0.1 [3.94]	90
CE-CD-05s	CAGE	Double-S	-0.11 [-4.33]	0.1 [3.94]	90
CE-CDS-06	CAGE	Single	-0.11 [-4.33]	0.05 [1.97]	90
CE-CD-07	CAGE	Double-L	-0.11 [-4.33]	0 [0.00]	90
CE-CD-07s	CAGE	Double-S	-0.11 [-4.33]	0 [0.00]	90
CE-CDS-08	CAGE	Single	-0.11 [-4.33]	0.05 [1.97]	270
CE-CDS-10	CAGE	Single	-0.11 [-4.33]	0.25 [9.84]	270
CE-DS-02	CAGE	Single	-0.21 [-8.27]	0.15 [5.91]	0
CE-DS-03	CAGE	Single	-0.21 [-8.27]	0.05 [1.97]	0
CE-DS-04	CAGE	Single	-0.21 [-8.27]	0.05 [1.97]	180
CE-DS-05	CAGE	Single	-0.21 [-8.27]	0.15 [5.91]	180
CE-DD-01	CAGE	Double-L	-0.21 [-8.27]	0.3 [11.81]	90
CE-DD-01s	CAGE	Double-S	-0.21 [-8.27]	0.3 [11.81]	90
CE-DDS-02	CAGE	Single	-0.21 [-8.27]	0.25 [9.84]	90
CE-DD-03	CAGE	Double-L	-0.21 [-8.27]	0.2 [7.87]	90
CE-DD-03s	CAGE	Double-S	-0.21 [-8.27]	0.2 [7.87]	90
CE-DDS-04	CAGE	Single	-0.21 [-8.27]	0.15 [5.91]	90
CE-DD-05	CAGE	Double-L	-0.21 [-8.27]	0.1 [3.94]	90
CE-DD-05s	CAGE	Double-S	-0.21 [-8.27]	0.1 [3.94]	90
CE-DDS-06	CAGE	Single	-0.21 [-8.27]	0.05 [1.97]	90
CE-DD-07	CAGE	Double-L	-0.21 [-8.27]	0 [0.00]	90
CE-DD-07s	CAGE	Double-S	-0.21 [-8.27]	0 [0.00]	90

Table A-5 (continued) Type and Location of Conductivity Probes

TAG NUMBER	COMPONENT	TYPE OF SENSOR	AXIAL LOCATION (m [in])	RADIAL LOCATION (m [in])	AZIMUTHAL ANGLE (°)
CE-DDS-08	CAGE	Single	-0.21 [-8.27]	0.05 [1.97]	270
CE-DDS-09	CAGE	Single	-0.21 [-8.27]	0.15 [5.91]	270
CE-ES-01	CAGE	Single	-0.31 [-12.20]	0.25 [9.84]	0
CE-ES-03	CAGE	Single	-0.31 [-12.20]	0.05 [1.97]	0
CE-ES-04	CAGE	Single	-0.31 [-12.20]	0.05 [1.97]	180
CE-ES-06	CAGE	Single	-0.31 [-12.20]	0.25 [9.84]	180
CE-ED-01	CAGE	Double-L	-0.31 [-12.20]	0.3 [11.81]	90
CE-ED-01s	CAGE	Double-S	-0.31 [-12.20]	0.3 [11.81]	90
CE-EDS-02	CAGE	Single	-0.31 [-12.20]	0.25 [9.84]	90
CE-ED-03	CAGE	Double-L	-0.31 [-12.20]	0.2 [7.87]	90
CE-ED-03s	CAGE	Double-S	-0.31 [-12.20]	0.2 [7.87]	90
CE-EDS-04	CAGE	Single	-0.31 [-12.20]	0.15 [5.91]	90
CE-ED-05	CAGE	Double-L	-0.31 [-12.20]	0.1 [3.94]	90
CE-ED-05s	CAGE	Double-S	-0.31 [-12.20]	0.1 [3.94]	90
CE-EDS-06	CAGE	Single	-0.31 [-12.20]	0.05 [1.97]	90
CE-ED-07	CAGE	Double-L	-0.31 [-12.20]	0 [0.00]	90
CE-ED-07s	CAGE	Double-S	-0.31 [-12.20]	0 [0.00]	90
CE-EDS-08	CAGE	Single	-0.31 [-12.20]	0.05 [1.97]	270
CE-EDS-10	CAGE	Single	-0.31 [-12.20]	0.25 [9.84]	270
CE-FS-02	CAGE	Single	-0.41 [-16.14]	0.15 [5.91]	0
CE-FS-03	CAGE	Single	-0.41 [-16.14]	0.05 [1.97]	0
CE-FS-04	CAGE	Single	-0.41 [-16.14]	0.05 [1.97]	180
CE-FS-05	CAGE	Single	-0.41 [-16.14]	0.15 [5.91]	180
CE-FD-01	CAGE	Double-L	-0.41 [-16.14]	0.3 [11.81]	90
CE-FD-01s	CAGE	Double-S	-0.41 [-16.14]	0.3 [11.81]	90
CE-FDS-02	CAGE	Single	-0.41 [-16.14]	0.25 [9.84]	90
CE-FD-03	CAGE	Double-L	-0.41 [-16.14]	0.2 [7.87]	90
CE-FD-03s	CAGE	Double-S	-0.41 [-16.14]	0.2 [7.87]	90
CE-FDS-04	CAGE	Single	-0.41 [-16.14]	0.15 [5.91]	90
CE-FD-05	CAGE	Double-L	-0.41 [-16.14]	0.1 [3.94]	90
CE-FD-05s	CAGE	Double-S	-0.41 [-16.14]	0.1 [3.94]	90
CE-FDS-06	CAGE	Single	-0.41 [-16.14]	0.05 [1.97]	90
CE-FD-07	CAGE	Double-L	-0.41 [-16.14]	0 [0.00]	90
CE-FD-07s	CAGE	Double-S	-0.41 [-16.14]	0 [0.00]	90
CE-FDS-08	CAGE	Single	-0.41 [-16.14]	0.05 [1.97]	270
CE-FDS-09	CAGE	Single	-0.41 [-16.14]	0.15 [5.91]	270

Table A-5 (continued) Type and Location of Conductivity Probes

TAG NUMBER	COMPONENT	TYPE OF SENSOR	AXIAL LOCATION (m [in])	RADIAL LOCATION (m [in])	AZIMUTHAL ANGLE (°)
CE-GD-03	CAGE	Double-L	-0.51 [-20.08]	0.2 [7.87]	90
CE-GD-03s	CAGE	Double-S	-0.51 [-20.08]	0.2 [7.87]	90
CE-GDS-04	CAGE	Single	-0.51 [-20.08]	0.15 [5.91]	90
CE-GD-05	CAGE	Double-L	-0.51 [-20.08]	0.1 [3.94]	90
CE-GD-05s	CAGE	Double-S	-0.51 [-20.08]	0.1 [3.94]	90
CE-GDS-06	CAGE	Single	-0.51 [-20.08]	0.15 [5.91]	90
CE-GD-07	CAGE	Double-L	-0.51 [-20.08]	0 [0.00]	90
CE-GD-07s	CAGE	Double-S	-0.51 [-20.08]	0 [0.00]	90
CE-HDS-07	CAGE	Single	-0.61 [-24.02]	0 [0.00]	90

APPENDIX B. TEST PROCEDURES

B.1 Steady State Tests

To ensure the quality of the experimental data, the following steps are performed before running the experiments for each test condition:

A. Test facility checking and valve adjustment
    1. Check water level (nominal water level 1.05 m [3.44 ft]).
    2. Check the manual valve positions for the air injection line (V-AL-01 closed, V-AL-02 closed, V-AL-05 opened, V-AL-06 closed).
    3. Check the air supply pressure at air compressor (>130 psig [997.7 kPa]).
    4. Adjust the needle valve positions (opening and closing) of pneumatic actuator (VM-AL-01) to the required position.
B. Instrument and DAS program preparation
    1. Open the DAS program.
    2. Check the input parameters in the DAS program such as the data sampling rate, bypass valve (VM-AL-02) opening time, and data acquisition time.
    3. Adjust the pneumatic actuator valves to the default position (VM-AL-01 and VM-AL-02 closed) using the DAS program.
    4. Check all instrument readings from DAS control program.
C. Confirmation of high-speed video camera and movie-recording program
    1. Open the movie recording program and check program working status.
    2. Adjust the focus of the lens and the aperture size of the camera.
    3. Check the input parameters in the movie-recording program such as frame size, fps, shutter speed, etc.

After completing the above procedures from A to C, the following steps are performed to start the experiment.

1. Adjust void condition in the downcomer section by opening the manual valve V-AL-02 until it reaches the required water level based on visual observation (only for partial void test conditions).
2. Initialize the test by executing the DAS program to open VM-AL-02 initially and open VM-AL-01 later while closing VM-AL-02.
3. The DAS program starts to record the experimental data after the signal to open VM-AL-01 is activated (time at 0 second). Simultaneously, the movie-recording program initiates to capture the high-speed video for around 10 seconds with 250 fps recording.

After about 30 seconds, VM-AL-01 is closed by the DAS program and recording of experimental data is terminated accordingly.

B.1.1 Test Initiation Time

The test is initiated by the DAS program which sends the electrical signal to open the main supply valve (VM-AL-02) and initialize the high-speed camera simultaneously. However, due to electronic system limitations, the starting times of DAS and high-speed camera have some

difference. Table B-1 represents the test initiation point for the high-speed camera and the DAS. For the high-speed camera, test initiation happens when the air-water interface arrives at the downcomer exit. For the DAS, test initiation occurs when the single-sensor conductivity probe located at the downcomer exit responds to the phase change. This should be considered when interpreting the test results.

Table B-1 Test Initiation Time at DAS and High-speed Camera Time Frames.

Test No.	Test Initiation Time (second)	
	DAS Time	Camera Time
A1	1.50	1.08
A2	1.50	1.07
A3	1.50	1.10
A4	4.49	4.02
A5	1.50	1.04
A6	1.50	1.02
A7	1.50	1.04
A8	1.86	1.09
A9	1.50	1.11
A10	1.50	1.01
A11	1.53	1.17
A12	6.00	5.74
A13	1.50	1.15
A14	1.50	1.14
A15	1.50	1.16
A16	1.50	1.19

B.2 Transient Tests

To ensure the quality of the experimental data, the following steps are performed before running the experiments for each test condition:

A. Test facility conditions and valve adjustment
   1. Purge instrumentation racks.
   2. Ensure air compressor is on and air supply pressure is ≥130 psig (997.7 kPa).
   3. Set up location of high-speed camera and turn on SP lighting.
   4. Isolate PCCS, ICS, and GD from DW and SP.
   5. Set up oxygen analyzers for both the DW and downcomer.
   6. Adjust SP water and gas space temperature to 37 °C ± 1 °C (98.6 °F ± 1.8 °F) .
   7. Adjust SP water level to ~1.05 m (~3.44 ft) and confirm visually through SP view port (water should touch horizontal marker on downcomer).
   8. Vent SP / confirm SP pressure ~0 psig (~101 kPa).
   9. Drain DW / confirm DW is empty.
   10. Vent DW / confirm DW ~0 psig (~101 kPa).

11. Fill RPV with water to ~2.8 meters (~9.2 ft).
12. Turn on RPV camera fans, RPV cameras, and camera monitors.
13. Close RPV heater breakers and heat up RPV to 10 psig (170 kPa).
14. Vent noncondensable gases from the RPV and ensure even RPV heating.
15. Heat RPV to ~130 psig (~998 kPa).
16. Heat DW using heated compressed air to 65 °C (+ 2 °C - 1 °C)[1] (149 °F [+ 3.6 °F - 1.8 °F]).
17. Adjust SP Pressure to approximately 1.8 psig (±1 psi) (113.8 kPa [± 6.9 kPa]).
18. Open manual valves on the appropriate Main Steam / DPV lines:

Test Case	Manual Valves
2 DPV	MS-A
3 DPV	MS-A MS-C
5 DPV	DPV MS- C

B. Instrument and DAS program preparation
   1. Open the DAS programs.
   2. Check all instruments readings from DAS control program.

C. Confirmation of high-speed video camera and movie-recording program
   1. Open the movie recording program and check program working status.
   2. Adjust the focus of the lens and the aperture size of camera.
   3. Check the input parameters in the movie-recording program such as frame size, frames per second, shutter speed, etc.

After completing the above procedures from A to C, the following steps are performed to start the experiment:

1. Adjust water level in the downcomer section by cycling the motor-operated DW vents.
2. Position the appropriate DPV valves in AUTO:

Test Case	DPV
2 DPV	MS-A
3 DPV	MS-A MS-C
5 DPV	DPV MS- C

3. Initialize the test by executing the RPV heater computer program.

[1] For the 5 DPV - 80% noncondensable gas tests, use steam from the RPV for final heating rather than air. Blowdown for approximately 10 seconds to achieve 80% initial noncondensable concentration.

4. Trigger the DAS programs to record data once the RPV is pressurized to 134 psig (1024 kPa) by the RPV heater computer program.
5. Initiate the movie-recording program and divide the recording into 5 partitions. Each partition is approximately 9 seconds of recording length. High-speed movie recordings are to be made at

Movie Partition	Elapsed Test Time (seconds)	Test Period
1	0	Initial
2	30	Stabilizing
3	60	Steady State
4	300	Steady State (2DPV / 3DPV) / Onset of Chugging (5DPV / 5DPV - 80%)
5	540	Chugging

6. Record data for 10 minutes.

B.2.1 Test Initiation Time

The test is initiated by the DAS program which sends an electrical signal to open the appropriate steam lines. The high-speed camera is initiated by a human operator when the RPV pressure reaches 1024 kPa (134.0 psig). This causes the starting times of DAS and high-speed camera to have some differences. Table B-2 represents this time difference between the high-speed camera and the DAS for the initial period. The data provided in this table can be useful to compare trends between the DAS and high-speed camera.

Table B-2 Approximate Difference between DAS and High-speed Camera Time Frames for the Initial Period.

Test No.	Time Comparison (seconds)	
	DAS Time	Camera Time
T1	6.22	1.80
T2	5.82	3.53
T3	5.25	3.30
T4	5.87	3.57
T5	5.52	3.18
T6	6.17	5.53
T7	5.42	1.65
T8	4.58	3.83

APPENDIX C. UNCERTAINTY ANALYSIS

C.1 Introduction

The uncertainty analysis presented here is based on the methods outlined in NUREG/CR 6309 (Ref. 3). The error propagation analysis is derived using a combination of errors obtained from the instrument specifications and in-house calibration data. The analysis is performed at the 95% confidence level, which is equivalent to two standard deviations.

The uncertainty determinations are discussed in detail in the following sections, with one section devoted to each of the specific instrument types. Note that for the transient and steady state tests, a different board was used in the data acquisition systems. Thus, for the steady state tests (using a NI-USB-6225 board) and the transient tests (using a NI-USB-6225 board for conductivity probes and a EXP-16 board for other parameters), there is a small difference in overall uncertainty.

The methodology used in this uncertainty analysis is that recommended by the ASME Performance Test Codes Supervisory Committee 19.1 (Ref. 9). Nomenclature used in this analysis include: precision index, S, which is a measure of the calibration scatter about the mean; bias limit, B, which is a measure of the difference between the mean of the calibration data and the standard; the 95th percentile point for the two-tailed Student t distribution, t; and the precision error, P, which is the product of t and S. The root sum square (RSS) of the components of the bias limit results in the overall bias limit for the measurement. The RSS of the precision errors results in the overall precision error for the measurement. The overall uncertainty, U, for a specific measurement is the RSS of the bias limit and the precision error. That is

$$B_{total} = \left(\Sigma B_t^2\right)^{1/2} \tag{C.1}$$

$$P_{total} = \left(\Sigma\left(tS^t\right)^2\right)^{1/2} \tag{C.2}$$

$$U_{RSS} = \left(B_{total}^2 + P_{total}^2\right)^{1/2} \tag{C.3}$$

C.2 K-Type Thermocouples

Based on the information obtained from The Temperature Handbook, OMEGA Engineering, Inc., Vol 27, p. H-4, the thermocouple “Limit of Error” is ± 2.2 °C (± 4.0 °F) or ± 0.75% of reading, whichever is greater. Since 0.75% of 180 °C (356 °F) (maximum expected temperature) is 1.4 °C, ± 2.2 °C (2.5 °F, ± 4 °F) was used as limit of error. This limit is defined by ANSI - MC96.1 which states that no thermocouples may exceed it. Therefore it may be assumed that the uncertainty is at the 95% confidence level (i.e.: two standard deviations). The output from each thermocouple is fed into a data acquisition board. For the transient tests, EXP-16, a 16-channel multiplexer and signal conditioning board, was used with the gain setting for this board at 200. For the steady state tests, a NI-USB-6225 board was adopted.

One of the principal uncertainties associated with the use of the data acquisition board is the "Peak-to-peak noise level," or the electronic noise imposed on the signal. The noise level is a function of the specific transducer (for example Type K thermocouple) and amplifier gain setting. The specifications for this board do not list the noise level for a Type K thermocouple with the corresponding gain setting. The peak-to-peak noise level was obtained experimentally. The average standard deviation for 26 thermocouple channels is 0.41 °C (0.74 °F)for the transient tests and 0.75 °C (1.35 °F) for the steady state tests.

The bias for the DAS boards, including the effect of cold junction compensation, is set by calibration. The criterion is that the standard deviation will be kept below 1 °C (1.8 °F). This calibration is performed for two thermocouples per board and includes the uncertainties of the wiring.

For the transient tests, performing a RSS of the two precision components (from the thermocouples and the peak-to-peak noise in the EXP-16 boards) and using a student *t* value of 2.0 (i.e.: two standard deviations) the precision error is P_{total} = 2.35 °C (4.23 °F). The overall bias is B_{total} = 2.0 °C (3.6 °F), and the uncertainty is U = 3.1 °C (5.6 °F).

For the steady state tests, performing a RSS of the two precision components (from the thermocouples and the peak-to-peak noise in the NI_USB_6225 boards) and using a student *t* value of 2.0 (i.e.: two standard deviations) the precision error is P_{total} = 2.66 °C (4.79 °F). The overall bias is B_{total} = 2.0 °C (3.6 °F), and the uncertainty is U = 3.3 °C (5.9 °F).

C.3 Pressure and Differential Pressure Measurements

The facility uses pressure transducers manufactured by Honeywell for all pressure and differential pressure measurements. These transducers are designed to measure pressure over a specific range:

- STD924 - 0-1 bar (0-14.7 psi) ["ST 3000 Series 900 Smart Transmitter Differential Pressure Model STD924" Honeywell Specification 34-ST-03-35, 4/92]
- STD930 - 0-7 bar (0-103 psi) ["ST 3000 Series 900 Smart Transmitter Differential Pressure Model STD930" Honeywell Specification 34-ST-03-36, 7/92]
- STG944 - 0-35 bar (0-515 psig) ["ST 3000 Series 900 Smart Transmitter Differential Pressure Model STG974" Honeywell Specification 34-ST-03-37, 7/92].

Each transducer is discussed, in turn, in the following sections. For all of the applications using the STD differential pressure transducers, it is assumed that the electronics are far enough away from any high temperatures that they are at ambient temperature. The transducers are designed so that this is relatively easy to accomplish and by doing so the "Combined Zero and Span Temperature Effect" is neglected. If the installation results in the transducer temperature exceeding 21°C (70°F), then an additional error is introduced and would have to be quantified. This would add ~ 0.4% of the upper range value to the bias error associated with each transducer for each 28°C (50°F) increase.

C.3.1 STD924

The PUMA instrumentation uses the STD924 transducer to measure either gage pressure or differential pressure over eight ranges, depending on the specific application. Honeywell Specification 34-ST-03-35, 7/92 lists the accuracy for this transducer to be ± 0.1% of either the calibrated span or the upper range value, whichever is greater. Here the calibrated span is defined as 25% of the Upper Range Limit. The Upper Range Limit for this transducer is 100 kPa (400 inch H_2O) and the calibrated span is 25 kPa (100 inch H_2O). Therefore, for any PUMA application with an upper range value (maximum pressure to be measured) less than 25 kPa, the accuracy is ± 25 Pa (± 0.1 in H_2O). Where the maximum pressure exceeds 25 kPa, the accuracy is ± 0.1% of this maximum pressure. This accuracy is treated as a bias error, in accordance with ANSI/ASME PTC 19.1.

The output from an STD924 transducer is fed into a multiplexer and signal shaper. The STD924 output is a 4-20 mA signal that is measured across a 250 Ω ± 0.1% output resistor, resulting in a 1 - 5 V input signal for the multiplexer. For the transient tests, the multiplexer gain is set at 1. At this setting, the linearity uncertainty (bias) is ± 0.015% of the maximum pressure and the peak-to-peak noise (precision) is ± 0.14% of the maximum pressure. (Ref. 10) while for the steady state tests, both the linearity uncertainty (± 0.016% of the maximum pressure) and peak-to-peak noise (± 0.125% of the maximum pressure) were obtained experimentally.

The output from the multiplexer is input into the DAS-801 analog-to-digital converter. There are four sources of measurement error associated with this board: gain accuracy, linearity, gain stability, and zero stability. The gain accuracy, for an input signal of 5 V, is ± 1.25% of the upper range value. The linearity is ± 1.2% of the upper range value. Both of these are bias errors. The two sources of precision error are the gain stability, 50 ppm of the upper range value, and zero stability, 20 ppm of the upper range value.

Finally, these errors are summed, in accordance with Equations C.1 – C.3. In general, the uncertainty is ~ 1.7% of the upper range value for the transient tests and ~ 1.8% of the upper range value for the steady state tests, independent of the span being measured. These uncertainties only include the transducer and associated electronics errors. Specifically excluded are uncertainties associated with the use of the pressure measurement to infer global conditions - for example, the use of the differential pressure measurement to infer liquid level, which should also include uncertainties associated with the potential for voiding in the sensor line.

C.3.2 STG944

These are used to measure pressure over the pressure range of 0 – 1.5 MPa (0 - 218 psi). Based on the maximum pressure to be measured, the (bias) accuracy for this transducer is ± 3.2 kPa (0.46 psi). For the transient tests, the linearity and peak-to-peak noise uncertainties for the EXP-16 multiplexer are ± 150 Pa (0.022 psi) and ± 1.4 kPa (0.20 psi), respectively. For the steady state tests, the linearity and peak-to-peak noise uncertainties for the NI-USB-6225 multiplexer are ± 37.5 Pa (5.44×10^{-3} psi) and ± 1.25 kPa (0.181 psi), respectively. The two bias contributions for the DAS801 ADC (gain accuracy and linearity) are ± 12.5 kPa (± 1.81 psi) and

± 12.0 kPa (± 1.74 psi), respectively. The two precision components for this board (gain stability and zero stability) are ± 50 Pa (± 7.25×10^{-3} psi) and ± 20 Pa (± 2.9×10^{-3} psi), respectively. The overall uncertainty associated with this transducer is ± 18 kPa (± 2.6 psi) or ~ 1.8% of the upper range value for the transient tests and ± 18 kPa (± 2.6 psi) or ~ 1.8% of the upper range value for the steady state tests. To reduce the uncertainties of key measurements, like reactor vessel levels and absolute pressures of the main vessels, many pressure transducers were calibrated in-house.

C.4 Flow Measurements

Vortex flow meter model 84W, manufactured by Foxboro, is used in the PUMA facility. This transducer works on the principle that a disturbance in the flow field will generate vortices, the number of which is proportional to the flow rate. Therefore, the flow can be measured by counting the number of vortices per unit time.

These flow meters measure gas velocities in the range of 1.5 m/s to 120.5 m/s (4.9 ft/s to 395 ft/s). They have an accuracy of ± 1.0 m/s (± 3.3 ft/s). The NI_USB_6225 multiplexer has linearity (bias) of ± 0.064 m/s (± 0.21 ft/s) and a peak-to-peak noise level (precision) of ± 0.32 m/s (± 1.1 ft/s). The DAS801 ADC has a gain accuracy and linearity (both bias) components of ± 0.51 m/s and ± 0.49 m/s (± 1.7 ft/s and ± 1.6 ft/s), respectively. This board has a gain stability and zero stability (both precision) components of ± 0.002 m/s and 0.008 m/s (± 0.01 ft/s and ± 0.03 ft/s), respectively. This results in an overall uncertainty of ± 2.2 m/s (± 7.2 ft/s) or 1.2% of the upper range value.

C.5 Oxygen Analyzer (only used in the transient tests)

Three oxygen analyzers are installed in the PUMA facility and are used to measure oxygen concentrations in the DW, pressure suppression chamber, and passive containment cooling system/isolation condenser system. The oxygen sensor is the Thermox RM CEM O2/IQ; Extractive Zirconium Oxide Oxygen Analyzer manufactured by AMETEK (Ref. 8). This transducer measures oxygen concentrations over a range of 0 ~ 21%. The transducer accuracy is ± 0.05% O_2 concentration or ± 0.75% of reading, whichever is greater. Since the upper range limit is 21%, the accuracy was chosen to be ± 0.16% O_2, and this was assumed to be a bias uncertainty. For this range of oxygen concentrations, the EXP-16 multiplexer linearity is ± 0.003% O_2 (bias) and the peak-to-peak noise is ± 0.029% O_2. The DAS-801 ADC uncertainties are ± 0.26 and ± 0.025% O_2 for the gain accuracy and linearity (both bias) and ± 0.001 and ± 0.004% O_2 for the gain stability and zero stability (both precision) components, respectively. The overall uncertainty for this measurement, including both bias and precision components for the transducer and electronics, is ± 0.2% O_2.

REFERENCES

1. **NUREG-0408**, “Mark I containment Short Term Program – Safety Evaluation Report,” U.S. Nuclear Regulatory Commission, Washington, DC, December, 1977.
2 Lahey, R. T. Jr., and F. J. Moody, “The Thermal-Hydraulics of a Boiling Water Nuclear Reactor,” 2nd ed. La Grange Park, IL: American Nuclear Society, 1993.
3. **NUREG/CR-6309**, “Scientific Design of Purdue University Multi-Dimensional Integral Test Assembly (PUMA) for GE SBWR,” U.S. Nuclear Regulatory Commission, Washington, DC, 1996.
4. **U.S. Nuclear Regulatory Commission**, A. Velazquez, “Technical Assessment GSI-193, BWR ECCS Suction Concerns, Geometrical and Operation Characteristics Effecting the Ingress of Noncondensable gases in the BWR ECCS System During HELB Accident”, 2010 (available in ADAMS under Accession #ML102460492).
5. **U.S. Nuclear Regulatory Commission**, “Rev. 11 of TI 2515177 Inspection Guidance”, 2011 (available in ADAMS under Accession #ML111660749).
6 T. Hibiki, S. Hogsett, and M. Ishii, “Local Measurement of Interfacial Area, Interfacial Velocity and Liquid Turbulence in Two-Phase Flow,” Nucl. Eng. Des. 184 (1998) 287-304.
7. **ASME**, “Fluid Meters: Their Theory and Application,” 1971.
8. **AMETEK Corp.**, “Thermox RM CEM 02/IQ Extractive Zirconium Oxide Oxygen Analyzer” Technical Specification Manual, October 2005.
9. **ANSI/ASME PTC 19.1**, “Part 1: Measurement Uncertainty - Instruments and Apparatus,” American National Standards Institute / American Society of Mechanical Engineers, 1985.
10. **Keithley MetraByte**, Data Acquisition Catalog & Reference Guide, Taunton, MA, 1994 - 1995.

NRC FORM 335
(12-2010)
NRCMD 3.7

U.S. NUCLEAR REGULATORY COMMISSION

BIBLIOGRAPHIC DATA SHEET

(See instructions on the reverse)

1. REPORT NUMBER
(Assigned by NRC, Add Vol., Supp., Rev., and Addendum Numbers, if any.)

NUREG/CR-7186

2. TITLE AND SUBTITLE

Experimental Measurement of Suppression Pool Void Distribution during Blowdown in Support of Generic Issue 193

3. DATE REPORT PUBLISHED

MONTH	YEAR
September	2014

4. FIN OR GRANT NUMBER

N6831

5. AUTHOR(S)

M. Ishii, T. Hibiki, S. Rassame, M. Griffiths, D.Y. Lee, P. Ju,
J. Yang, S. L. Sharma, and S.W. Choi

6. TYPE OF REPORT

Technical

7. PERIOD COVERED (Inclusive Dates)

8. PERFORMING ORGANIZATION - NAME AND ADDRESS (If NRC, provide Division, Office or Region, U. S. Nuclear Regulatory Commission, and mailing address; if contractor, provide name and mailing address.)

Purdue University
School of Nuclear Engineering
West Lafayette, IN 47907

9. SPONSORING ORGANIZATION - NAME AND ADDRESS (If NRC, type "Same as above", if contractor, provide NRC Division, Office or Region, U. S. Nuclear Regulatory Commission, and mailing address.)

Division of Systems Analysis
Office of Nuclear Regulatory Research
U. S. Nuclear Regulatory Commission
Washington, DC 20555

10. SUPPLEMENTARY NOTES

11. ABSTRACT (200 words or less)

The possible failure of an Emergency Core Cooling System (ECCS) train due to a large amount of entrained gas in the ECCS pump suction piping during a loss of coolant accident (LOCA) is one of the potential engineering problems faced in a Boiling Water Reactor (BWR) power plant. The void fraction distribution and void penetration in the Suppression Pool (SP) during blowdown from a LOCA are key parameters necessary to analyze potential gas intrusion into the ECCS pump suction piping. To study void fraction distribution and void penetration in the Suppression Pool (SP) during blowdown, two sets of experiments, namely steady state tests and transient tests, were conducted using the Purdue University Multi-Dimensional Integral Test Assembly for ESBWR applications (PUMA-E) facility. The design of the test apparatus used is based on a scaling analysis from a prototypical BWR containment (Mark I) with consideration of downcomer size, SP water level and downcomer water submergence depth. Several instruments were installed to obtain the required experimental data such as the gas volumetric flow, void fraction, pressure, and temperature.

12. KEY WORDS/DESCRIPTORS (List words or phrases that will assist researchers in locating the report.)

advanced light water reactor, simplified boiling water reactor (SBWR), ESBWR, loss of coolant accident (LOCA), emergency core cooling system (ECCS), ECCS pump, suppression pool, PUMA, void penetration, blowdown

13. AVAILABILITY STATEMENT

unlimited

14. SECURITY CLASSIFICATION

(This Page)
unclassified

(This Report)
unclassified

15. NUMBER OF PAGES

16. PRICE

Federal Recycling Program

UNITED STATES
NUCLEAR REGULATORY COMMISSION
WASHINGTON, DC 20555-0001

OFFICIAL BUSINESS

NUREG/CR-7186

Experimental Measurement of Suppression Pool Void Distribution During Blowdown in Support of Generic Issue 193

September 2014